



**HAL**  
open science

# Effects of high pressure on empty and water-filled single-wall carbon nanotubes studied by Raman spectroscopy

Abraao Cefas Torres Dias

► **To cite this version:**

Abraao Cefas Torres Dias. Effects of high pressure on empty and water-filled single-wall carbon nanotubes studied by Raman spectroscopy. Physics [physics]. Université Claude Bernard - Lyon I, 2014. English. NNT: 2014LYO10283 . tel-01128278

**HAL Id: tel-01128278**

**<https://theses.hal.science/tel-01128278>**

Submitted on 9 Mar 2015

**HAL** is a multi-disciplinary open access archive for the deposit and dissemination of scientific research documents, whether they are published or not. The documents may come from teaching and research institutions in France or abroad, or from public or private research centers.

L'archive ouverte pluridisciplinaire **HAL**, est destinée au dépôt et à la diffusion de documents scientifiques de niveau recherche, publiés ou non, émanant des établissements d'enseignement et de recherche français ou étrangers, des laboratoires publics ou privés.

N° d'ordre 283-2014

Année 2014

**THESE DE L'UNIVERSITE DE LYON**

Délivrée par

L'UNIVERSITE CLAUDE BERNARD LYON 1

ECOLE DOCTORALE DE PHYSIQUE ET ASTROPHYSIQUE

DIPLOME DE DOCTORAT  
(arrêté du 7 aout 2006)

soutenue publiquement le 11 decembre 2014

par

Abraao Cefas TORRES DIAS

**EFFECTS OF HIGH PRESSURE ON EMPTY AND WATER-FILLED  
SINGLE-WALL CARBON NANOTUBES STUDIED BY RAMAN  
SPECTROSCOPY**

Directeur de Thèse: A. San Miguel

Co-directeur de Thèse: D. Machon

JURY

M. Jean-Louis Bantignies

Rapporteur

M. David Dunstan

Rapporteur

Mme. Catherine Journet-Gautier

Examineur

Mme. Pascale Launois

Examineur

Mme. Sofie Cambré

Examineur

M. Denis Machon

Co-directeur de Thèse

M. Alfonso San Miguel

Directeur de Thèse



## ABSTRACT

# EFFECTS OF HIGH PRESSURE ON EMPTY AND WATER-FILLED SINGLE-WALL CARBON NANOTUBES STUDIED BY RAMAN SPECTROSCOPY

Abraao Cefas TORRES DIAS

Université de Lyon 1, 2015

Carbon nanotubes have extraordinary mechanical, thermal and electrical properties. Among many possible applications, their properties offer great potential to develop new electronic devices or to fabricate innovative composite materials allying lightness and resilience. Their unidimensional physical features are interesting for fundamental studies at nanometric scale. The simplest type of carbon nanotube is the single-wall. It is constituted by a graphene sheet (a bi-dimensional layer of carbon atoms) rolled up to form a cylinder. In view of their potential applications for electronics - where strain engineering is important - or in structured materials, the study of the response to pressure is a major issue. In the scientific literature, theoretical studies estimate that the structural stability of carbon nanotubes, including the radial collapse, depend on the diameter. Experimentally, the quantitative confirmation of the predictions is compromised by the lack of suitable samples or by environmental effects, coupled to resonance effects. Lately, optimal solubilisation of carbon nanotubes in water-surfactant solutions allowed individual assignment by Raman spectroscopy. The present thesis constitutes a set of experimental studies on the effect of high pressures on single wall carbon nanotubes, individualized, closed or open, therefore empty or filled with water. High-pressure techniques and Raman spectroscopy were combined to study the radial collapse, as well to probe the pressure-induced modifications. Chirality-resolved pressure derivatives were obtained for the radial breathing modes (RBM). The RBM of water-filled could be observed at pressures higher than those of empty. After a high-pressure cycle, empty nanotubes of larger diameters were not detectable anymore, while sub-nanometric diameter ones became filled with water. Such observations suggest that thinner nanotubes have better pressure-stability, which is increased upon water-filling. An unusual response of the (7,2) nanotube suggests that the chirality may have also an important role on the structural stability for small diameters. The evolution of the tangential modes suggest the onset of radial collapse of empty nanotubes averaging 1.32 nm diameter at about 4 GPa, in agreement with the latest theoretical predictions. These same nanotubes, though water-filled, they collapse at pressures higher than 16 GPa.



## RÉSUMÉ

Les nanotubes de carbone ont des propriétés mécaniques, thermiques et électriques extraordinaires. Parmi bien d'autres applications, ces propriétés offrent un grand potentiel pour développer des nouveaux dispositifs électroniques ou pour fabriquer des matériaux composites novateurs alliant légèreté et résistance mécanique. Leurs caractéristiques physiques unidimensionnelles sont également d'intérêt pour des études fondamentales à l'échelle nanométrique. Le plus simple des nanotubes de carbone est à feuillet unique ou mono-parois. Il est constitué par une feuille de graphène (une couche bidimensionnelle d'atomes de carbone) enroulée pour former un cylindre. Au vu de ses applications potentielles en électronique où l'ingénierie de contraintes est très importante - ou dans des matériaux de structure, l'étude de la réponse en pression des nanotubes de carbone est un enjeu majeur. Dans la littérature scientifique, les études théoriques estiment que la stabilité structurelle des nanotubes de carbone, qui incluent son effondrement radial, dépendent du diamètre. Expérimentalement, la confirmation quantitative des prédictions est compromise par le manque d'échantillons bien définis ou par les effets de l'environnement, le tout couplé à des effets de résonance. Récemment, la solubilisation optimisée de nanotubes de carbone dans des solutions eau-surfactant a permis l'identification individuelle précise des nanotubes bien définis par spectroscopie Raman. La présente thèse est constituée par un ensemble d'études expérimentales sur l'effet des hautes pressions sur les nanotubes de carbone mono-parois, individualisées, fermés ou ouverts, donc vides ou remplis d'eau. Les techniques des hautes pressions et de la spectroscopie Raman ont été combinées afin d'étudier l'effondrement des nanotubes et de sonder les modifications induites par l'effet de la pression. Les coefficients de pression des modes radiaux de respiration (RBM) ont été obtenus avec identification individuelle par chiralité. Les RBM des nanotubes remplis d'eau ont pu être observés à des pressions bien plus élevées que pour des nanotubes vides. Après un cycle à haute pression, les nanotubes vides de diamètre plus important n'étaient pas détectables tandis que les tubes de diamètre sous-nanométrique se sont remplis d'eau. Ces observations suggèrent que les nanotubes de diamètre le plus faible ont une meilleure stabilité sous pression qui est accrue par le remplissage par de l'eau. Une réponse inusuelle du nanotube (7,2) suggère que la chiralité peut avoir aussi un rôle aussi important dans la stabilité structurelle, en tout cas pour les nanotubes de plus faibles diamètres. De son côté, l'évolution des modes de vibration tangentiels suggère l'effondrement radial des nanotubes vides d'un diamètre d'environ de 1.32 nm à une pression proche de 4 GPa, en accord avec les prévisions théoriques les plus récentes. Ces mêmes tubes remplis d'eau, présentent un effondrement à une pression qui se situe au-delà de 16 GPa.



---

## TABLE OF CONTENTS

|  | Page |
|--|------|
| CHAPTERS   |      |
| I High-pressure studies on carbon nanotubes . . . . .            | 3    |
| I.1 Carbon nanotubes . . . . .                                   | 3    |
| I.2 Raman spectroscopy . . . . .                                 | 9    |
| I.3 High-pressure physics . . . . .                              | 13   |
| I.4 Raman spectroscopy of carbon nanotubes . . . . .             | 16   |
| I.5 High-pressure physics applied to carbon nanotubes . . . . .  | 20   |
| II Samples and experimental setup . . . . .                      | 29   |
| II.1 Samples . . . . .   | 29   |
| II.2 More on the samples . . . . .                               | 33   |
| II.3 High-pressure spectroscopy setup . . . . .                  | 35   |
| III Pressure effects on the Radial Breathing Modes . . . . .     | 39   |
| III.1 Mixed empty and water-filled sample . . . . .              | 39   |
| III.2 Empty and water-filled HiPco samples . . . . .             | 40   |
| III.3 Empty and water-filled Arc samples . . . . .               | 43   |
| III.4 Pressure derivatives . . . . .                             | 44   |
| III.5 Discussion on the Radial Breathing Modes . . . . .         | 44   |
| IV Pressure effects on the Tangential Modes . . . . .            | 55   |
| IV.1 Data Analysis . . . . .                                     | 55   |
| IV.2 On the analysis of the G-band . . . . .                     | 58   |
| IV.3 Spectral line shape . . . . .                               | 61   |
| IV.4 Irreversible changes induced by pressure . . . . .          | 62   |
| IV.5 Pressure derivatives under hydrostatic conditions . . . . . | 63   |
| IV.6 Collapse . . . . .  | 65   |

---

---

## INTRODUCTION

Carbon nanotubes were experimentally observed at first time in 1991<sup>1</sup>. They show elastic modulus<sup>2,3</sup>, tensile strength<sup>4,5</sup>, flexibility<sup>6</sup> and electronic properties<sup>7</sup> comparable or better than those found in different nowadays optimal materials, however, simultaneously combined in a single piece. Such a set of excellent properties put them as promising candidates for applications in diverse domains. In addition, their unique featured one-dimensional physics is of great interest for materials science<sup>8</sup>.

Nanoconfinement can boost the understanding of materials at the molecular level and on nanostructuration in general. Upon confinement inside carbon nanotubes, polyiodides<sup>9</sup>, water<sup>10-13</sup>, fullerenes<sup>14-20</sup> and other molecules were suggested or even demonstrated to assume different geometrical arrangements and show distinct properties. Since pressure can squeeze carbon nanotubes<sup>21</sup>, they can act as pressure-mediators to filler contents, which can open possibilities to the engineering of materials at nanometric scale. The high mechanical resilience of carbon nanotubes allows for the study of their coupling with fluids under different mechanical constraints<sup>22</sup>. While in nanocavities, fluids can exhibit new properties and structures unobserved in their bulk counterparts<sup>23-26</sup>. Carbon nanotubes are also promising for nanofluidic applications<sup>27</sup>. They can provide fast fluid transport inside their nanochannels<sup>28,29</sup>, filtration in molecular level<sup>30</sup> and even the development of nanovalves<sup>31</sup>. For the particular case of water molecules, proton transport<sup>32</sup> and hydroelectric power conversion<sup>33</sup> can be feasible. For energy source related applications, hydrogen storage in carbon nanotubes has been proposed<sup>34</sup>.

Applications requiring lightness and toughness may profit directly on carbon nanotubes, such as reinforced composites<sup>35,36</sup> and high-end fibers<sup>37-39</sup>. Moreover, carbon nanotubes may be also present in future electronics. The first complex devices such as a computer microprocessor based on carbon nanotubes have been proved feasible<sup>40</sup>. However, advanced microchips have dense circuitry, for which encapsulation put them to operate in high-pressure conditions. Since the properties of carbon are geometry dependent, the electronic response is expected to change upon pressure application<sup>41</sup>. Specifically, pressure is expected to change the band gap of semiconducting nanotubes<sup>42</sup>. Theoretical studies suggest that carbon nanotubes can assume an elliptic or even a collapsed geometry under metallic contacts<sup>43</sup> or depending on diameter, these geometries may be reached by interactions with the media, such as was found for carbon nanotubes lying on substrates<sup>44</sup>. Therefore, high pressure conditions could pose constraints for the utilization of CNTs in electronic devices, but by another viewpoint, it could provide pressure-tunable properties, which was demonstrated in carbon nanotube based transistors<sup>45</sup>.

Combined to the diamond anvil cell<sup>46</sup>, optical absorption<sup>47</sup>, X-ray diffraction<sup>21</sup>, photoluminescence<sup>48</sup>, and resonant Raman spectroscopy<sup>49</sup> were proven successful for probing in-situ the pressure response of carbon nanotubes. Further studies carried with these mentioned techniques revealed that not only the pressure, but the environment and the filling have influence on the response to pressure<sup>50-54</sup>. Considering the intrinsic parameters of carbon nanotubes, theoretical studies and computer simulations support that the mechanical stability depends on the inverse of the diameter<sup>55</sup> and possibly on chirality<sup>56</sup>.

This thesis work present a study on the response to pressure of empty and water-filled single walled carbon nanotubes. Specifically, a set of experiments were carried out allying diamond anvil cell as the pressure generator and Raman spectroscopy as the probing technique. As main advances to previous studies, investigations were carried out on optimal carbon nanotubes samples which allowed resolution on chirality and separation between empty and filled configurations. As a main contribution, this study helps to clarify the role of filling and environment on the pressure stability of carbon nanotubes.

## CHAPTER I

## HIGH-PRESSURE STUDIES ON CARBON NANOTUBES

This chapter introduces the main concepts on carbon nanotubes and the experimental techniques used in this thesis work. It also presents a bibliographic review over high pressure physics applied to carbon nanotubes.

## I.1 CARBON NANOTUBES

Carbon nanotubes (CNT) are cylindrical shaped allotropes of carbon. Their simplest form is illustrated in fig. 1.1a, in which an atomic thick layer of carbon atoms is rolled up into a cylindrical shell, called Single Wall Carbon Nanotube (SWNT). Two concentrically aligned SWNTs form a Double Wall Carbon Nanotube (DWNT), as shown in fig. 1.1b. In the same fashion as DWNTs, several SWNTs can form a Multi Wall Carbon Nanotube (MWNT). The thinner SWNTs have diameters of less than one nanometer, whilst the thicker MWNTs can have dozens of nanometers. CNTs can be short as one micrometer in length, or long as one hundred micrometer.

The simplest geometrical model to describe a SWNT considers its wall opened and flattened to a 2-dimensional (2D), honeycomb-like structure. This 2D carbon sheet is known as graphene, which if piled up in several layers constitutes graphite. Both materials are also illustrated in fig. 1.1. The graphene 2D lattice is sketched in fig. 1.2a. Assuming the carbon bond length  $a_{c-c}$  equal to  $1.421\text{\AA}$ , the lattice constant  $a_0$  and the unit vectors  $\vec{a}_1$  and  $\vec{a}_2$  are written as:

$$a_0 = \sqrt{3}a_{c-c} = |\vec{a}_1| = |\vec{a}_2| \quad (\text{I.1.1})$$

$$\vec{a}_1 = \left(\frac{\sqrt{3}a_0}{2}, \frac{a_0}{2}\right), \vec{a}_2 = \left(\frac{\sqrt{3}a_0}{2}, -\frac{a_0}{2}\right) \quad (\text{I.1.2})$$

The vectors  $\vec{b}_1$  and  $\vec{b}_2$  which generates the reciprocal space (shown in fig. 1.2b) are obtained through the orthogonality condition:

$$\vec{a}_i \cdot \vec{b}_j = 2\pi\delta_{ij} \quad (\text{I.1.3})$$

then:

$$\vec{b}_1 = \left(\frac{2\pi}{\sqrt{3}a_0}, \frac{2\pi}{a_0}\right), \vec{b}_2 = \left(\frac{2\pi}{\sqrt{3}a_0}, -\frac{2\pi}{a_0}\right) \quad (\text{I.1.4})$$

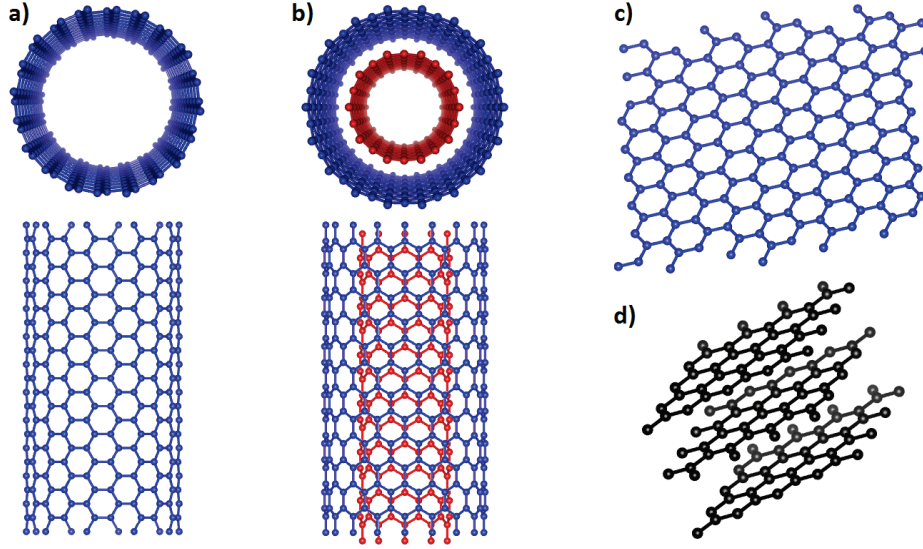


**FIG. 1.1:** Examples of carbon materials<sup>57,58</sup>. (a) Single Wall Carbon Nanotube (SWNT). (b) Double Wall Carbon Nanotube (DWNT). (c) Graphene. (d) Graphite.

In the simplest tight binding approach, electronic dispersion (energy dispersion relations) of graphene is given by<sup>60</sup>:

$$E_{2D}(k_x, k_y) = \pm t \left[ 1 \pm 4 \cos\left(\frac{\sqrt{3}k_x a}{2}\right) \cos\left(\frac{k_y a}{2}\right) + 4 \cos^2\left(\frac{k_y a}{2}\right) \right] \quad (\text{I.1.5})$$

in which  $k_x$  and  $k_y$  are unit wave vectors in the reciprocal space. The equation I.1.5 is plotted in fig. 1.2c, highlighting the K point vicinity. These concepts and equations from I.1.1 to I.1.5 will be useful for the modelization that follows.

The SWNT rolling up from graphene is governed by the Chiral Vector  $\vec{C}_h$ , which has modulus equal to the SWNT circumference length while projected on the honeycomb lattice. Accordingly to the fig.1.3a,  $\vec{C}_h$  is written in terms of the unit vectors  $\vec{a}_1$  and  $\vec{a}_2$ :

$$\vec{C}_h = n\vec{a}_1 + m\vec{a}_2, \quad (\text{I.1.6})$$

The integer indexes  $n$  and  $m$  quantify the roll up and define the chirality  $(n, m)$  of a SWNT. Knowing  $\vec{C}_h$ ,  $\vec{a}_1$  and  $\vec{a}_2$ , diameter  $d_t$  and chiral angle  $\theta_{C_h}$  are respectively given by:

$$d_t = \frac{|\vec{C}_h|}{\pi} = \frac{(\vec{C}_h \cdot \vec{C}_h)^{\frac{1}{2}}}{\pi} = \frac{a_0 \sqrt{n^2 + m^2 + mn}}{\pi} \quad (\text{I.1.7})$$

$$\theta_{C_h} = \cos^{-1} \frac{\vec{C}_h \cdot \vec{a}_1}{|\vec{C}_h| |\vec{a}_1|} \quad (\text{I.1.8})$$

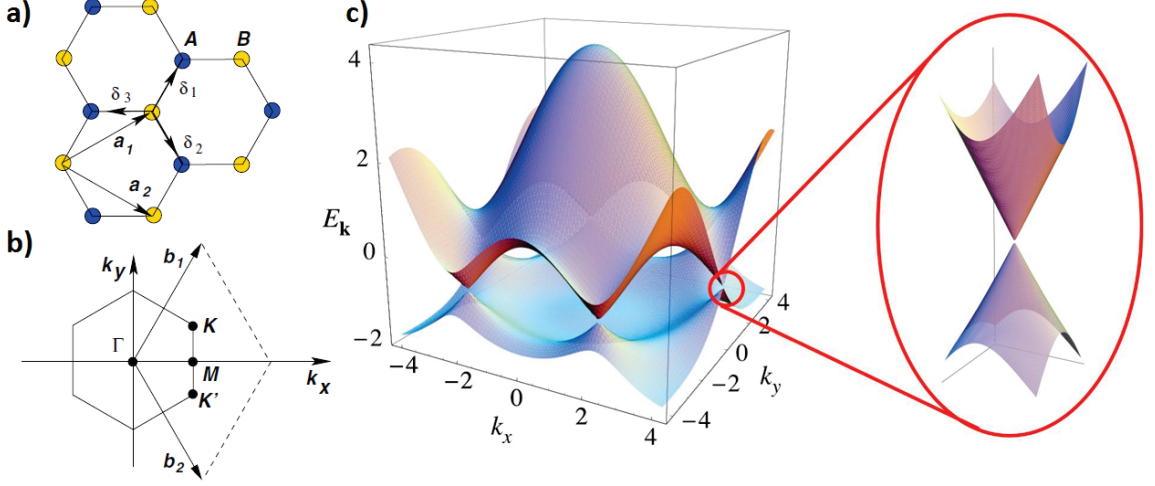


**FIG. 1.2:** Graphene<sup>59</sup>. (a) Real space: 2D honeycomb lattice. (b) Reciprocal space: the first Brillouin Zone. (c) Electronic dispersion and the  $K$  point vicinity highlighted.

For simplicity, CNTs are often classified by their chiral indexes  $(n, m)$  as zigzag ( $m = 0, \theta_{Ch} = 0$ ), armchair ( $m = n, \theta_{Ch} = 30$ ) and chiral ( $m \neq n, 0 < \theta_{Ch} < 30$ ). All three types are illustrated in fig.1.4.

The nanotube is then build up by repeating  $\vec{C}_h$  periodically, which is done by the Translational Vector  $\vec{T}$ :

$$\vec{T} = t_1 \vec{a}_1 + t_2 \vec{a}_2, \quad (\text{I.1.9})$$

The rectangle made by  $\vec{C}_h$  and  $\vec{T}$  delimits the SWNT unit cell. By  $\vec{T}$  own definition,  $\vec{C}_h$  and  $\vec{T}$  must be mutually perpendicular. Thus, the coefficients  $t_1$  and  $t_2$  are:

$$\vec{C}_h \cdot \vec{T} = 0 \Rightarrow t_1 = \frac{2m + n}{D_c}, t_2 = -\frac{2n + m}{D_c} \quad (\text{I.1.10})$$

in which  $D_c$  is the greatest common divisor of  $(2m + n)$  and  $(2n + m)$ . The unit cell then fits  $N$  hexagons, totaling  $2N$  atoms, with  $N$  given by the unit cell area divided by one hexagon area:

$$N = \frac{|\vec{C}_h \times \vec{T}|}{|\vec{a}_1 \times \vec{a}_2|} = 2 \frac{(n^2 + m^2 + mn)}{D_c} \quad (\text{I.1.11})$$

Knowing the real lattice vectors  $\vec{C}_h$  ( $\vec{R}_1$ ) and  $\vec{T}$  ( $\vec{R}_2$ ), the reciprocal lattice vectors  $\vec{K}_1$  and  $\vec{K}_2$  are obtained by applying the orthogonality condition:

$$\vec{K}_i \cdot \vec{R}_j = 2\pi \delta_{ij} \quad (\text{I.1.12})$$

Thus, the equations I.1.6, I.1.9 and I.1.12 altogether give:

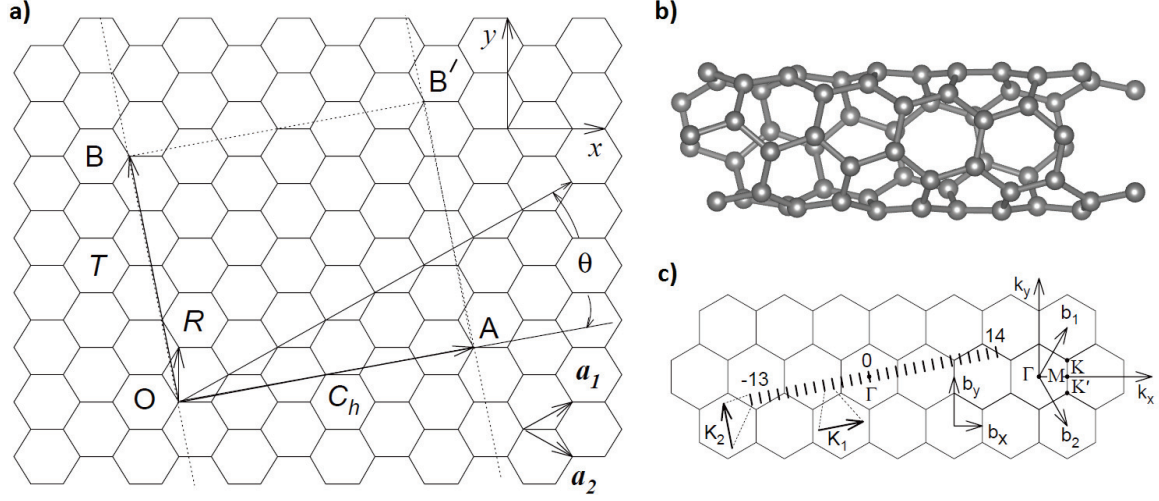


**FIG. 1.3:** The rolling up of the graphene sheet to build the  $(4,2)$  SWNT. (a) Vectors which describe the SWNT geometry. The unit cell is delimited by  $\vec{C}_h$  and  $\vec{T}$ <sup>60</sup>. (b) The nanotube drawn in its unit cell size<sup>57,58</sup>. (c) Its reciprocal space.<sup>61</sup>.

$$\vec{K}_1 = \frac{-t_2\vec{b}_1 + t_1\vec{b}_2}{N}, \vec{K}_2 = \frac{m\vec{b}_1 - n\vec{b}_2}{N} \quad (\text{I.1.13})$$

Then,  $\vec{K}_1$  and  $\vec{K}_2$  generate the reciprocal space of a SWNT, as shown in fig. 1.3c. The first Brillouin Zone is the segment centered at  $\Gamma$ , having length equal to the modulus of  $\vec{K}_2$ . In this figure, each  $\mu$  ( $\mu = 0, \dots, N - 1$ )  $\vec{K}_1$  vector translates one  $\kappa \vec{K}_2/|\vec{K}_2|$  wave vector, giving the  $N$  lines periodically separated by  $|\vec{K}_1|$ . Whenever two wave vectors differs by  $N\vec{K}_1$ , they are equivalent and thus the periodicity is achieved in the reciprocal lattice. It is worth to note that  $\vec{K}_2$  is a reciprocal lattice vector, but  $\vec{K}_1$  is not. As consequence of this featured 1D periodicity, CNTs are often called 1D materials.

The electronic dispersion of SWNTs can be obtained by applying the 1D periodic conditions to the 2D electronic dispersion, i.e., limiting the graphene eigenstates to those simultaneously allowed for SWNTs. For that, one writes 1D wave vectors:

$$K_{\mu,\kappa} = \left( \kappa \frac{\vec{K}_2}{|\vec{K}_2|} + \mu\vec{K}_1 \right), (\mu = 0, 1, \dots, N - 1) \quad (\text{I.1.14})$$

and uses the  $N$  resulting  $K_{\mu,\kappa}$  equations to cut cross-sections on the 2D electronic dispersion  $E_{2D}$  given by equation I.1.5. Remark that  $\vec{K}_1$  and  $\vec{K}_2$  must be properly written in terms of  $\vec{k}_x$  and  $\vec{k}_y$  to be applied in the equation I.1.14. The resulting 1D electronic dispersions are then:

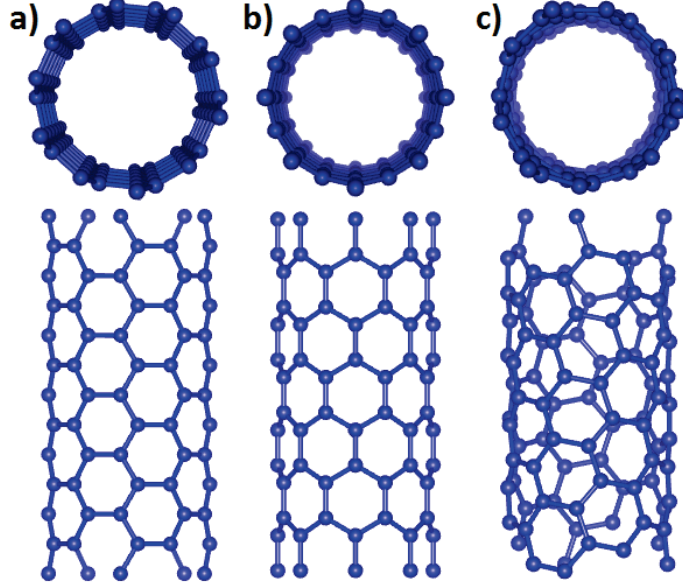


**FIG. 1.4:** Chiral aspect of SWNTs<sup>57,58</sup>. (a) (5,5) armchair. (b) (8,0) zigzag. (c) (6,3) chiral.

$$E_{1D}(\mu, \kappa) = E_{2D}\left(\kappa \frac{(\vec{K}_2)}{|\vec{K}_2|} + \mu \vec{K}_1\right), (\mu = 0, 1, \dots, N-1), \left(-\frac{\pi}{T} < \kappa < \frac{\pi}{T}\right) \quad (\text{I.1.15})$$

This procedure is called zone-folding. As an example, the cross-sections (cutting lines) of the (4, 2) SWNT are shown in fig. 1.5a. As an example for a generic zigzag nanotube, the electronic band structure and the resulting density of states (DOS) are sketched in left panel of fig. 1.6a. Instead of continuous curves, the DOS of carbon nanotubes shows a  $1/\sqrt{E}$  behavior, having peaked discontinuities characteristic of 1D structures known as van Hove singularities (vHS). The transition energies between two symmetric peaks (vHS) on valence and conduction bands are labeled  $E_{11}, E_{22}, \dots, E_{ii}$ , as shown in right panel of fig. 1.6a. The equation I.1.15 states that the vHS are chirality dependent, thus they are unique for a given nanotube. This fact makes possible the chiral indexes  $(n, m)$  assignment by probing  $E_{ii}$  through optical spectroscopy, namely photoluminescence (PL), absorption (ABS) and Resonant Raman Scattering (RRS). This led to the construction of a graph having  $E_{ii}$  plotted as a function of  $d_t$  or  $\omega_{RBM}$ , known as Kataura plot. One example is shown in fig. 1.6b, for which the  $E_{ii}$  values (Y axis) were calculated through third-order tight-binding approximation. Advanced versions of the Kataura plot include excitonic corrections. The dependence of  $\omega_{RBM}$  on  $d_t$  will be discussed in next section.

On graphene, the conducting and valence bands cross themselves in the  $K$  point. Thus, if a wave vector  $\vec{K}_2$  crosses the  $K$  point, then the CNT is metallic. If  $\vec{K}_2$  does not touch the  $K$  point, there is a band gap and the CNT is semiconducting. Geometrically,  $\vec{K}_2$  touches the

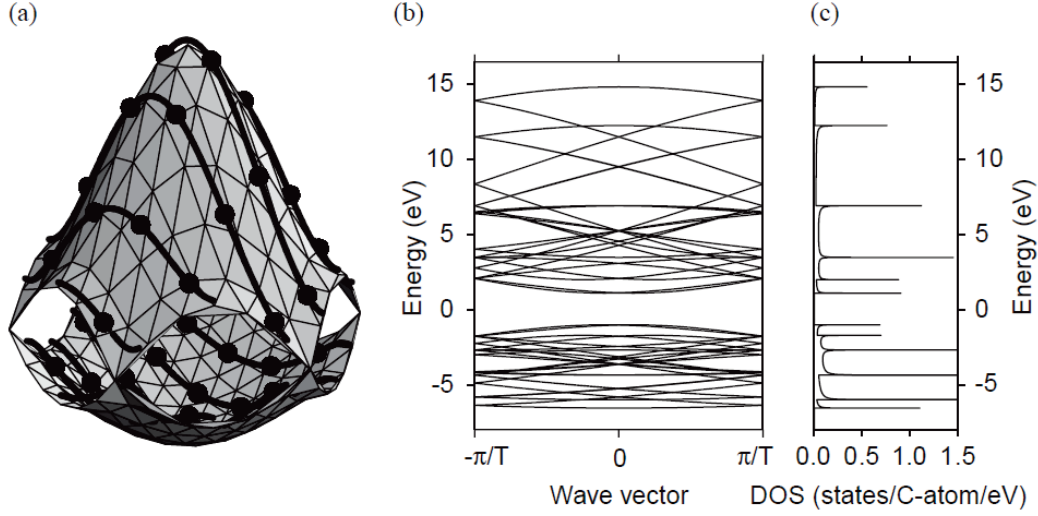


**FIG. 1.5:** Zone folding of the  $(4,2)$  SWNT<sup>62</sup>. (a) Cutting lines over the graphene energy dispersion. (b) Electronic bands for the  $(4,2)$  after zone folding the 2D-lattice. (c) The resulting density of electronic states (DOS).

$K$  point whenever an integer number of the  $\vec{K}_1$  vector fits in the smallest segment between the  $K$  point and the Brillouin zone. This segment  $B\vec{K}$  and  $\vec{K}_1$  are related as follows:

$$B\vec{K} = \frac{(2n + m)}{3} \vec{K}_1 \quad (\text{I.1.16})$$

Therefore, a CNT is metallic if  $(2n + m)/3$  is integer, otherwise it is semiconducting. An equivalent condition often used is:

$$q = (n - m) \bmod(3) \quad (\text{I.1.17})$$

The equation above separates metallic ( $q = 0$ ) and two families of semiconducting ( $q = 1$  or  $q = 2$ ) CNTs. It must be remarked that the zone-folding method does not consider curvature effects, which are important for SWNTs having diameter smaller than 1 nm. Strictly, only armchair SWNTs are purely metallic.

Non-armchair SWNTs which  $(n,m)$  give  $q = 0$  in eq. I.1.17 actually show a very small band gap. However, for such SWNTs at room temperature, the thermal energy is enough to excite electrons from the valence to the conduction band and consequently they show metallic response. Considering a more precise rule, SWNTs having small band gap follow a  $n - m = 3j$  relation, in which  $j$  is a nonzero integer. Analogously, those having larger band gap respect a  $n - m = 3j \pm 1$  relation.

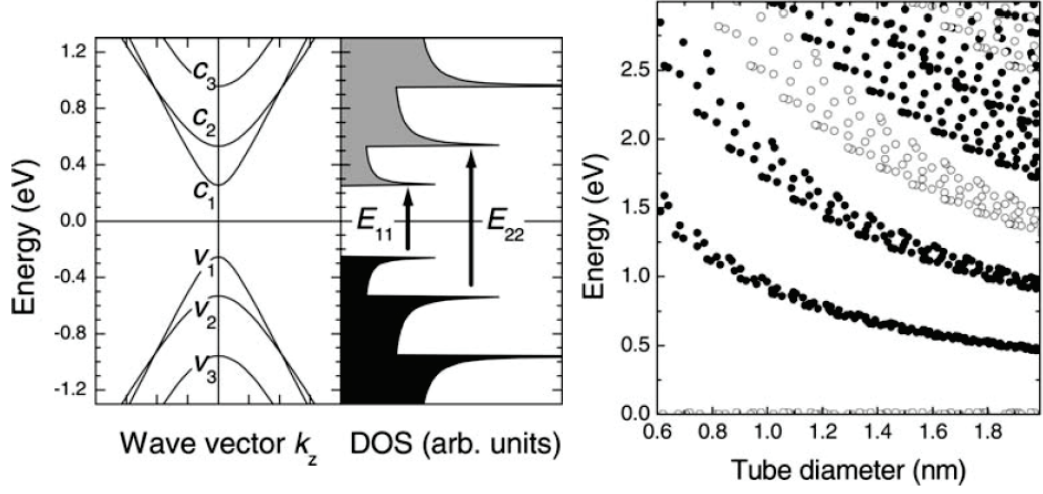


**FIG. 1.6:** (a) Sketch of the energy dispersion relation for a zigzag nanotube and the respective transition energies between van Hove singularities. (b) The Kataura plot. Semiconducting and metallic branches are shown respectively by filled and hollow symbols. Adapted from literature<sup>63</sup>.

## I.2 RAMAN SPECTROSCOPY

Raman effect is the inelastic scattering of a photon and Raman spectroscopy is named after the originating effect. It differs from Rayleigh scattering, which is elastic.

In general, light scattering is the phenomenon in which matter absorbs a photon and emits another almost instantaneously. Upon absorption, the incoming (incident) photon excites one electron from a lower to a higher energetic state, this electron is scattered by a phonon, then it decays to a lower energy state and one photon is emitted (scattered). The electron-phonon interaction has a lifetime  $\sim 10^{-15}s$ , therefore incident and emitted photons are said to be virtually absorbed and scattered respectively. If the incident and scattered photons have the same energy, the scattering is elastic. Different energies between incident and scattered photons means inelastic scattering. The energy loss (or gain) to the scattered photon implies the energy gain (or loss) to the phonon.

The elastic and inelastic light scattering phenomena are sketched in fig. 1.7. Given that the incident photon has energy  $E_i$  and frequency  $\omega_i$ , the scattered photon has energy  $E_s$  and frequency  $\omega_s$  and similarly a phonon has  $E_q$  and  $\omega_q$ , one can write:

$$E_i = \hbar\omega_i \quad (\text{I.2.1})$$

$$E_s = \hbar\omega_s \quad (\text{I.2.2})$$

$$E_q = \hbar\omega_q \quad (\text{I.2.3})$$

The Stokes Raman is featured by:  $E_s = E_i - E_q$ , ( $E_s < E_i$ ). The incident photon is

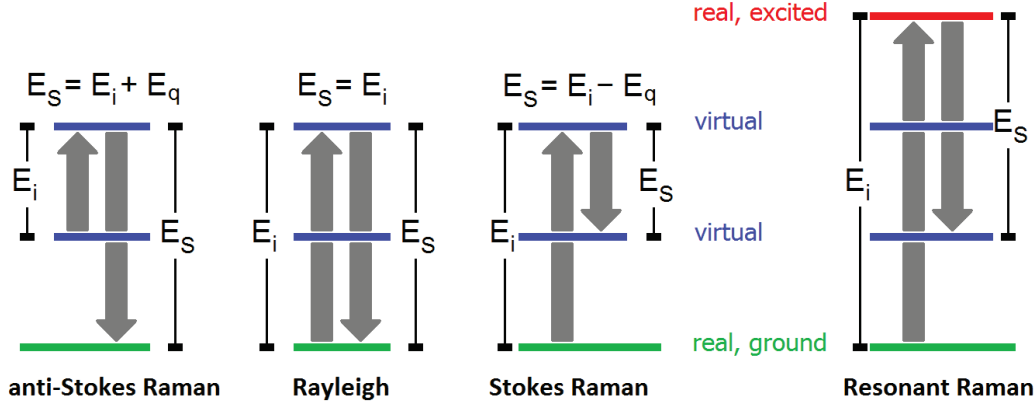


FIG. 1.7: Sketch of Rayleigh (elastic) and Raman (inelastic) scattering phenomena.

virtually absorbed, exciting an electron from its ground state to a virtual, higher energy state. Then, the electron decays to a lower energy state and one photon is emitted.

The anti-Stokes Raman means:  $E_s = E_i + E_q$ , ( $E_s > E_i$ ). The incident photon is virtually absorbed, exciting an electron from a lower energy state to a virtual, higher energy state. Then, the electron decays to its ground state and one photon is emitted.

The Rayleigh scattering happens if:  $E_s = E_i$ ,  $E_q = 0$ . The incident and scattered photons have the same energy, therefore the process is elastic. Differently from Raman scattering, there is no mediation by a phonon to give or loss energy to the scattered photon.

The term virtual state means an state which is not one of those that an electron would occupy through other phenomenon, like absorption. Although, if the energy given by the incident (or given to the scattered) photon during the scattering process matches the value of a transition between two real electronic states, the scattering is resonant. In both Stokes and anti-Stokes processes, the energetic difference between the incoming and scattered photons is equal to the energy of the phonon involved in the scattering process. Thus, the principle of the Raman spectroscopy technique is deliver photons having fixed wavelength and collect photons having wavelengths shifted by the electron-phonon interaction occurring in the material. Then, comparing the difference between incident and scattered wavelengths, one probes the phonon energies of the material.

The scattered radiation is provided by electric and magnetic multi-poles induced by the electric field of the incident radiation. Thus, polarizing conditions must be matched in order to a phonon (related to a vibrational mode) be active on Raman spectroscopy. To demonstrate a qualitative, classic description of the Raman effect<sup>64</sup>, one can writes the dipole  $\vec{P}_{mn}$  induced by the incident electric field  $\vec{E}$ :

$$\vec{P}_{mn} = (\alpha_{ij})_{mn} \vec{E}, \quad (\text{I.2.4})$$

in which  $\alpha$  is the polarizability tensor:

$$P_x = \alpha_{xx}E_x + \alpha_{xy}E_y + \alpha_{xz}E_z \quad (\text{I.2.5})$$

$$P_y = \alpha_{yx}E_x + \alpha_{yy}E_y + \alpha_{yz}E_z \quad (\text{I.2.6})$$

$$P_z = \alpha_{zx}E_x + \alpha_{zy}E_y + \alpha_{zz}E_z. \quad (\text{I.2.7})$$

A Taylor series expansion to  $\alpha$  on the normal coordinate  $q$  gives:

$$(\alpha_{ij}) = (\alpha_{ij})_0 + \left(\frac{d\alpha_{ij}}{dq}\right)q + \frac{1}{2}\left(\frac{d^2\alpha_{ij}}{dq^2}\right)q^2 + \dots \quad (\text{I.2.8})$$

The simplest situation implies a vibrational displacement occurring in one direction around the equilibrium position. Thus the equation above can be rewritten as:

$$\alpha = \alpha_o + \left(\frac{d\alpha}{dq}\right)_0 q + \frac{1}{2}\left(\frac{d^2\alpha}{dq^2}\right)_0 q^2 + \dots \quad (\text{I.2.9})$$

The incident electric field  $\vec{E}$  and the normal coordinate  $q$  can be written as:

$$\vec{E} = \vec{E}_0 \cos(\omega_i t), \quad (\text{I.2.10})$$

$$q = q_0 \cos(\omega_q t), \quad (\text{I.2.11})$$

in which  $\omega_i$  and  $\omega_q$  are the oscillating frequency of  $\vec{E}$  and  $q$  respectively. On a first approximation, the higher order terms of  $\alpha$  can be left aside. Then,  $P_{mn}^{\vec{}}$  can be written in terms of equations I.2.9, I.2.10 and I.2.11:

$$\vec{P} = \alpha_o \vec{E}_0 \cos(\omega_i t) + \left(\frac{d\alpha}{dq}\right)_0 q_0 \cos(\omega_q t) \vec{E}_0 \cos(\omega_i t), \quad (\text{I.2.12})$$

and rewritten by using the identity:

$$\cos(\omega_q t) \cos(\omega_i t) = \frac{1}{2} \cos(\omega_i t + \omega_q t) + \frac{1}{2} \cos(\omega_i t - \omega_q t) \quad (\text{I.2.13})$$

giving as result:

$$\vec{P} = \alpha_o \vec{E}_0 \cos(\omega_i t) + \frac{1}{2} \left(\frac{d\alpha}{dq}\right)_0 q_0 \vec{E}_0 \cos(\omega_i t + \omega_q t) + \frac{1}{2} \left(\frac{d\alpha}{dq}\right)_0 q_0 \vec{E}_0 \cos(\omega_i t - \omega_q t). \quad (\text{I.2.14})$$

The first term in the equation above has the oscillation frequency  $\omega_i$  of the incident photon, being the Rayleigh scattering term. The second and third terms having frequencies  $(\omega_i + \omega_q)$  and  $(\omega_i - \omega_q)$  feature the anti-Stokes and Stokes Raman scattering respectively,

following the equations I.2.1, I.2.2 and I.2.3. Thus, the Raman effect arises only if the polarizability  $\alpha$  change upon the incident radiation, requiring that  $(d\alpha/dq)_0 \neq 0$  in eq. I.2.14.

A qualitative quantum description of the Raman effect starts by writing the components of the tensor  $\alpha$  in terms of the initial  $\psi_m$  and final  $\psi_n$  states of the system:

$$(\alpha_{ij})_{mn} = \int \psi_m(\alpha_{ij})\psi_n d\tau \quad (\text{I.2.15})$$

for which the Taylor formula gives:

$$(\alpha_{ij})_{mn} = (\alpha_{ij})_0 \int \psi_m \psi_n d\tau + \left( \frac{d\alpha_{ij}}{dq} \right) \int \psi_m q \psi_n d\tau. \quad (\text{I.2.16})$$

If initial and final states are equal ( $m = n$ ), then there is Rayleigh scattering. If  $m \neq n$ :

$$\int \psi_m \psi_n d\tau = 0. \quad (\text{I.2.17})$$

giving:

$$(\alpha_{ij})_{mn} = \left( \frac{d\alpha_{ij}}{dq} \right) \int \psi_m q \psi_n d\tau. \quad (\text{I.2.18})$$

Thus, different initial and final states ( $m \neq n$ ) implies at least one changing into the polarizability tensor upon a vibration of the normal coordinate  $q$ , arising the Raman effect and inelastic scattering.

Considering the general case, the polarizability tensor  $\alpha_{ij}$  is given by<sup>65</sup>:

$$(\alpha_{ij})_{mn} = \frac{1}{\hbar} \sum_{r \neq m, n} \left( \frac{\langle \psi_n | \mu_i | \psi_r \rangle \langle \psi_r | \mu_j | \psi_m \rangle}{\omega_r - \omega_m - \omega_0 - i\Gamma_r} + \frac{\langle \psi_n | \mu_j | \psi_r \rangle \langle \psi_r | \mu_i | \psi_m \rangle}{\omega_r - \omega_n + \omega_0 + i\Gamma_r} \right). \quad (\text{I.2.19})$$

The coordinate are given by the indexes  $i$  and  $j$ . Initial, final and virtual states are given by  $|\psi_m\rangle$ ,  $|\psi_n\rangle$  and  $|\psi_r\rangle$ , having indexes  $m$ ,  $n$  and  $r$  respectively. The electric dipole momentum operator is described by  $\mu_i$  e  $\mu_j$ . The incident radiation and electronic transition frequencies are given by  $\nu_0$  and  $\nu_{rm}$ , respectively. The  $\Gamma_r$  is related to the lifetime of the virtual state  $|\psi_r\rangle$ , around  $10^{-15}$ s. The  $|\psi_m\rangle$ ,  $|\psi_n\rangle$  and  $|\psi_r\rangle$  states have electronic and vibrational mixed features. The brackets  $\langle \psi_r | \mu_i | \psi_m \rangle$  and  $\langle \psi_r | \mu_j | \psi_m \rangle$  show the system going from the initial state  $|\psi_m\rangle$  to the virtual state  $|\psi_r\rangle$ . The brackets  $\langle \psi_n | \mu_i | \psi_r \rangle$  and  $\langle \psi_n | \mu_j | \psi_r \rangle$  show the system going from the virtual state  $|\psi_r\rangle$  to the final state  $|\psi_n\rangle$ .

Resonant Raman scattering occurs if the incident photon frequency  $\omega_0$  matches an electronic transition,  $\omega_r - \omega_m$ , which increases  $\alpha_{ij}$  substantially as the first denominator in the

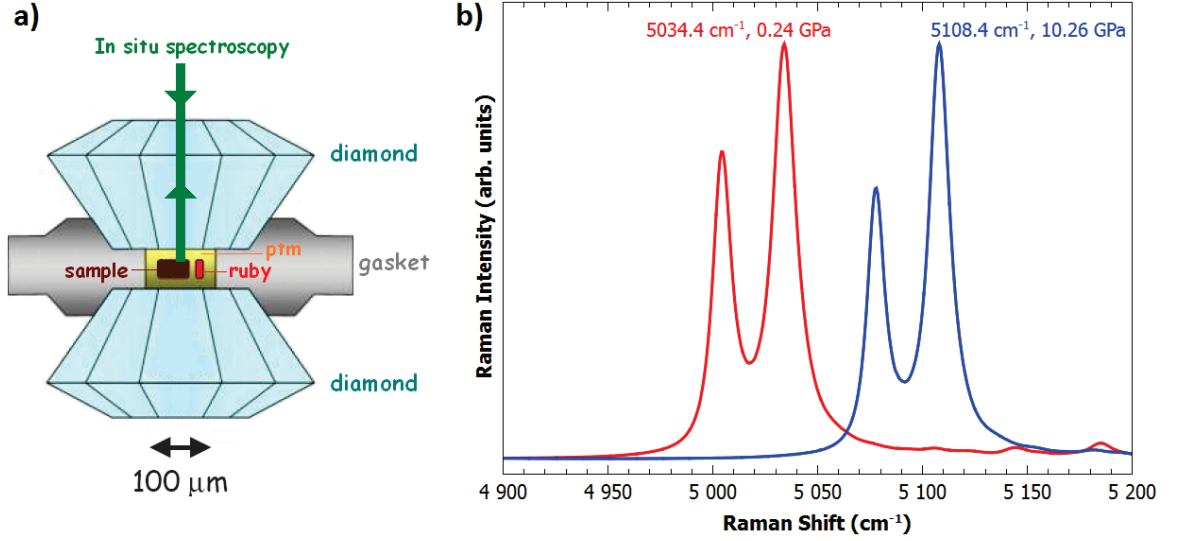


**FIG. 1.8:** (a) Sketch of a *in-situ* high-pressure spectroscopy experiment using a DAC. (b) The shift to higher frequencies of the R1 line of the ruby upon pressure application. Frequency values and the respective calculated pressures (see the text) are labeled.

expression approaches a minimal value. Finally, the Raman intensity depends on the square of  $\alpha_{ij}$ , having the general expression<sup>65</sup>:

$$I_{mn} = \frac{16\pi^2}{9c^4} I_i \nu_s^4 \sum_i \sum_j |(\alpha_{ij})_{mn}|^2, \quad (\text{I.2.20})$$

in which  $I_i$  is the incident radiation intensity and  $\nu_s$  is the scattered frequency.

### I.3 HIGH-PRESSURE PHYSICS

Pressure is inversely proportional to the surface in which the force is applied. Knowing that, one can achieve very high pressures by reducing the contact surface instead of only increasing the applied force. One of the scientific instruments constructed to this ending is the Diamond Anvil Cell (DAC). In a few words, the working principle of a DAC consists in compressing a small size sample between two diamonds having small contact surfaces. Diamond is the hardest material known, virtually incompressible and transparent, being suitable to be used for a high-pressure generating instrument.

The assembling of a DAC is sketched in fig. 1.8a. The diamonds are opposed by their culets (their bottom part). The culet size is given analogously to a diameter, ranging from 1000  $\mu\text{m}$  to 200  $\mu\text{m}$ . Smaller the culet, higher the pressure that can be reached. For example, the meant sizes combined with proper gaskets allow practical maximum pressures  $\sim 5$  GPa and more than 100 GPa, respectively. For comparison, the ambient pressure is  $\sim$

$10^5$  Pa (0.00001 GPa). A common setup for a DAC includes a gasket between the diamonds.

The gasket is a metallic plate which has a hole pierced in its center. While the gasket plasticizes upon the pressure applied by the diamonds, it gives a better control of pressure application. In a downgrade scale of hardness, rhenium, steel and copper are common choices for a gasket. Additionally, a gasket provides uniform surface contacts for the diamonds, providing mechanical stability for the assembling. The common thickness is 30-100  $\mu\text{m}$  (thinner for smaller culets) and the usual hole diameter is 0.3-0.5 of the culet size. The hole seals the sample and it must be filled entirely, either by sample content or by a fluid to complete the volume content.

One usefulness of fluid usage is to provide hydrostatic compression. Among the fluids used as pressure transmitting medium (PTM), argon and helium can provide hydrostatic conditions above 30 GPa. Nonetheless, easier to use paraffin oil and 4:1 methanol:ethanol mixture are common choices, having hydrostaticity up to 5 GPa and 10 GPa, respectively.

The standard method to measure the pressure originates from the fluorescence of a ruby chip, which is disposed alongside the sample. The ruby  $R_1$  fluorescent line shifts to higher energies upon pressure, which is calibrated by the relation<sup>66</sup>:

$$P = \frac{A}{B} \left\{ \left[ 1 + \left( \frac{\Delta\lambda}{\lambda_0} \right) \right]^B - 1 \right\} (GPa) \quad (\text{I.3.1})$$

The values  $A = 1904$  and  $B = 7.665$  are the calibration parameters,  $\lambda_0 = 694.23\text{nm}$  is the  $R_1$  wavelength at ambient pressure and  $\Delta\lambda$  is the shift of  $R_1$  upon pressure application. If the shift of  $R_1$  is measured in units of  $\text{cm}^{-1}$  (usual in Raman spectroscopy), an easy way to write  $\Delta\lambda$  is:

$$\Delta\lambda = \frac{1}{L(\text{cm}^{-1}) - R(\text{cm}^{-1})} 10^7 - \lambda_0(\text{nm}) \quad (\text{I.3.2})$$

in which  $L = 1/\lambda_L$  is the excitation wavelength  $\lambda_L$  converted from nm to  $\text{cm}^{-1}$  and  $R$  is the  $R_1$  shift given in  $\text{cm}^{-1}$ . An example of pressure measurement obtained by this method is shown in fig. 1.8b.

The DAC makes possible in-situ measurements, thus Raman, Infrared, Fluorescence, Photoluminescence, Absorption and X-Ray spectroscopies can be done under high-pressure conditions. Moreover, electric and magnetic measurements can also be done by carrying adaptations to the experimental setup.

The immediate consequence of applying pressure on a material is the decreasing of its volume  $V$ . To fit in the new reduced space, the geometric configuration must change, either by tilting and bending of molecular or crystal unities or simply by shortening of the atomic bonds. In a few words, the shortening of a bond length has a similar consequence to the

increasing of the elastic constant of a simple oscillator: the vibrational frequency increases. In molecules and crystals, the meant bending and tilting can increase or decrease the associated phonon frequencies. As discussed, Raman spectroscopy can probe the frequency  $\omega_i$  of a given phonon mode  $i$ . The scaling between  $V$  and  $\omega_i$  is given by the Gruneisen parameter  $\gamma_i$ , defined as<sup>67</sup>:

$$\frac{\omega_i}{\omega_{i0}} = \left( \frac{V}{V_{i0}} \right)^{-\gamma_i} \quad (\text{I.3.3})$$

in which  $\omega_{i0}$  is the frequency of the phonon  $i$  for the initial volume  $V_{i0}$ . If  $\omega_i$  does not depends on  $V$ , the differentiation of eq. I.3.3 with respect to pressure  $P$  gives:

$$\gamma_i = \frac{1}{\beta} \frac{1}{\omega_i} \left( \frac{\partial \omega_i}{\partial P} \right)_{P=0} \quad (\text{I.3.4})$$

$\beta$  is the isothermal compressibility:

$$\beta = -\frac{1}{V} \left( \frac{\partial V}{\partial P} \right)_T \quad (\text{I.3.5})$$

Optionally,  $\gamma_i$  can be written in terms of the Bulk modulus  $B_M$ :

$$\gamma_i = B_M \frac{1}{\omega_i} \frac{\partial \omega_i}{\partial P} \quad (\text{I.3.6})$$

$$B_M = -V \frac{\partial P}{\partial V} \quad (\text{I.3.7})$$

A typical Raman spectroscopy experiment under high pressure conditions consists in collecting spectra of a sample at different pressures. Thus, one can use Raman spectroscopy to obtain experimentally how  $\omega_i$  evolves in respect to  $P$ , usually by evaluating the pressure derivative  $\alpha_{\omega_i}$ :

$$\alpha_{\omega_i} = \frac{\partial \omega_i}{\partial P} \quad (\text{I.3.8})$$

or equivalently, the normalized pressure derivative  $\Omega_i$ :

$$\Omega_i = \frac{1}{\omega_i} \frac{\partial \omega_i}{\partial P} = \frac{\partial \ln \omega_i}{\partial P} \quad (\text{I.3.9})$$

which is immediately recognizable in the equations I.3.4 and I.3.6.

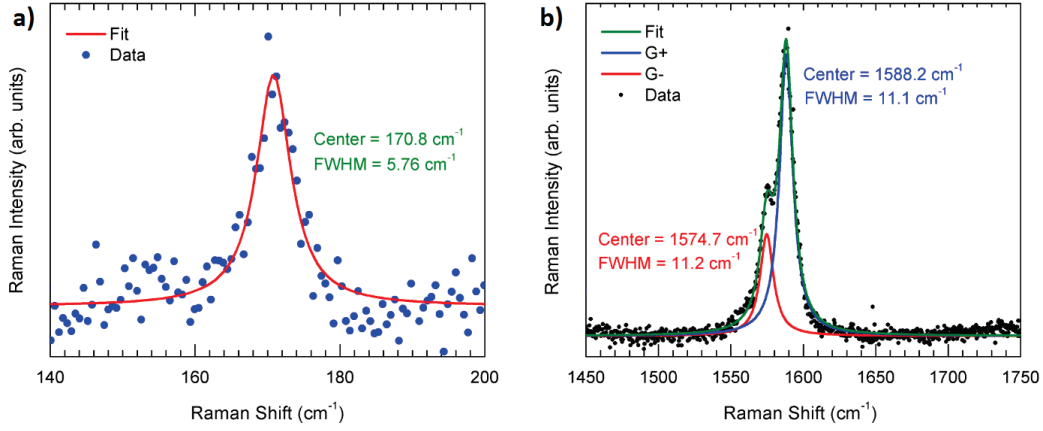


**FIG. 1.9:** (a) RBM spectrum of a SWNT growth by CVD over a silicon substrate. (b) The corresponding G-band spectrum. Curve fitting by Fityk<sup>68</sup>.

#### I.4 RAMAN SPECTROSCOPY OF CARBON NANOTUBES

The out-of-phase displacements between two neighbor atoms in a graphite plane originate the  $E_{2g}$  Raman active mode centered at  $1582\text{ cm}^{-1}$ , known as G-mode. Upon the graphene sheet rolling-up to construct a SWNT, the planar symmetry is broken and the G-mode splits in up to six modes and arise the G-band of a SWNT<sup>60</sup>.

The Raman active modes<sup>1</sup> of the G-band show two main features around the frequency range of  $1500\text{--}1600\text{ cm}^{-1}$ . The lower and the higher frequency features are respectively called G- and G+. As an example, the G-band spectrum of a single nanotube laid on a silicon substrate is shown in fig. 1.9. The G- and G+ Raman peaks are originated by the atomic vibrations shown in fig. 1.10. Considering achiral (zigzag and armchair) SWNTs, the G+ feature originates from  $A_{1g}$  and  $E_{2g}$  vibrations, whereas the G- from  $E_{1g}$  vibrations. In zigzag SWNTs, G+ and G- respectively propagate in axial and circumferential directions of the tube. In armchair SWNTs, the 30 degree difference in chiral angle swaps G+ and G- by in comparison to the zigzag configuration. For the case of chiral SWNTs, the atomic vibrations in axial and circumferential directions show mixed  $A_1$ ,  $E_1$  and  $E_2$  symmetries<sup>60,71–73</sup>. Nevertheless, it was found by calculations<sup>74</sup> and confirmed experimentally<sup>75</sup> that chiral, semiconducting SWNTs have their G+ and G- Raman peaks originated from vibrations in axial and circumferential directions, respectively.

Concerning the direction of propagation in respect to the CNT geometry, the phonons can be longitudinal (L) or transversal (T) to the axis of the nanotube. By activity, they can be optical (O) or acoustic (A). Thus, accordingly to the figure 1.10, G+ and G- are respectively LO and TO in zigzag, conversely they are TO and LO in armchair SWNTs.

<sup>1</sup>SWNTs have also infrared-active modes<sup>69,70</sup>.

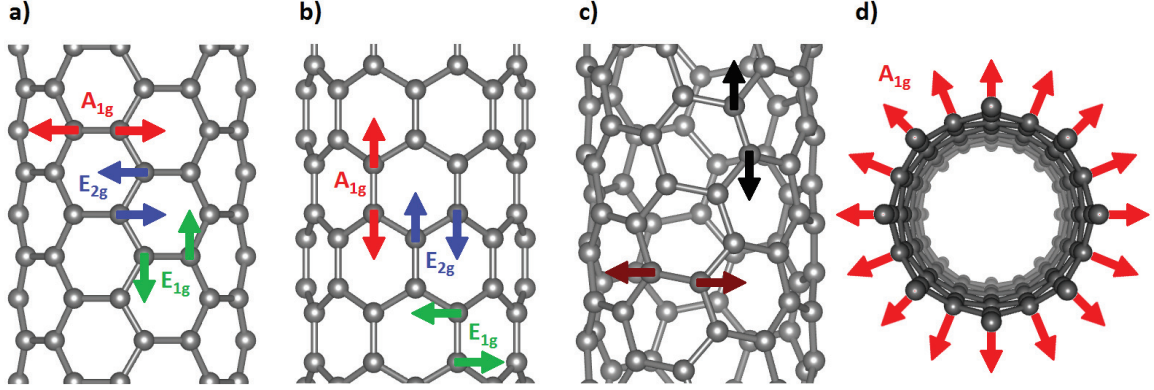


**FIG. 1.10:** The atomic vibrations which generate the G-band and RBM modes of SWNTs. The tangential  $A_{1g}$  and  $E_{2g}$  vibrations give the G+ Raman peak, whereas  $E_{1g}$  vibrations give the G- for armchair (a) and zigzag (b) SWNTs. For semiconducting chiral SWNTs (c), G+ and G- shown mixed  $A_1$ ,  $E_1$  and  $E_2$  symmetries, though G+ (black arrows) and G- (brown arrows) persist in axial and circumferential directions, respectively. The in-phase  $A_{1g}$  vibrations which rise the Radial Breathing Mode of a zigzag SWNT (d).

For semiconducting, chiral ones, G+ and G- keep the LO and TO confinements.

To analyze the Raman spectrum of carbon nanotubes, one must fit the G+ and G- features by functions and evaluate the obtained parameters. For instance, for the G-band spectrum shown in fig. 1.9, G+ and G- were fitted each by a Lorentzian distribution:

$$I_\omega = \frac{I_0}{1 + \left(\frac{\omega - \omega_L}{\gamma}\right)^2} \quad (\text{I.4.1})$$

in which the parameters are: center ( $\omega_L$ ), half width at the half maximum ( $\gamma$ ) and height or intensity ( $I_0$ ). Additionally to the fitted parameters, the line shape aspect of the G-band shall be addressed as it gives insight on metallic and semiconductor behaviors. As an example, fig. 1.11 shows the Raman spectra of a SWNT sample synthesized by the Arc discharge method<sup>77</sup>, which provides SWNTs having diameters  $1.35 \pm 0.25$  nm. These SWNTs were solubilized in a surfactant/water solution<sup>78,79</sup> and deposited on a silicon substrate. The spectra were collected with 532 nm and 633 nm wavelengths, respectively shown in green and red colors. The G-band of the two spectra show very different line shapes, which means that the two wavelengths select different SWNTs present in the sample. Specifically, the green and red colored spectra come from semiconducting and metallic SWNTs.

As the example in fig. 1.11 shows, semiconducting SWNTs have sharp G+ and G- peaks, which can be usually fitted by Lorentzian distributions, having full width at half maximum (FWHM, equal to  $2\gamma$  in equation I.4.1)  $\sim 5 - 15 \text{ cm}^{-1}$ <sup>73,80</sup>. Metallic SWNTs have a broad and asymmetrical G- peak due to an electron-phonon coupling. For metallic SWNTs, the

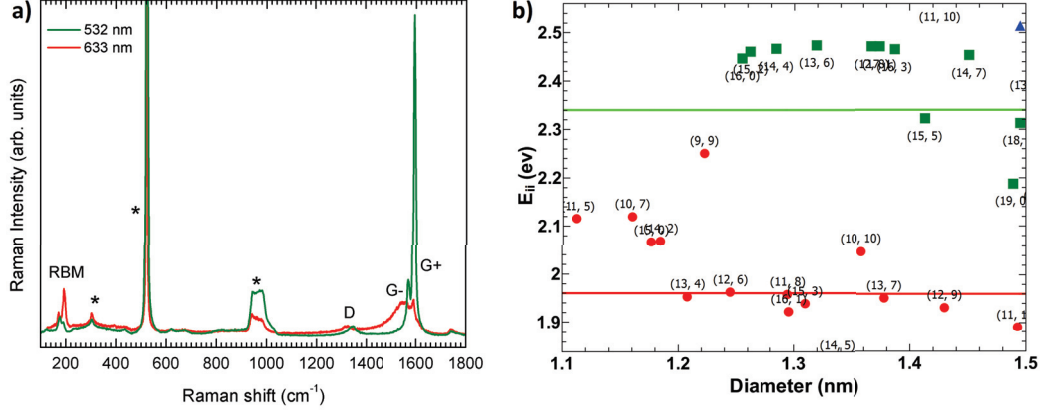


**FIG. 1.11:** (a) Raman spectra of Arc-SWNTs (see the text) collected with 532 nm and 633 nm wavelengths. The features marked by \* belong to the silicon substrate. The spectra are normalized by the Si-peak  $\sim 521 \text{ cm}^{-1}$ . (b) The Kataura plot<sup>76</sup>. The green and red horizontal lines crossing the graph show the corresponding energies of 532 nm (2.33 eV) and 633 nm (1.96 eV) wavelengths. Considering the diameter distribution of  $1.3 \pm 0.1 \text{ nm}$  of Arc SWNTs, which are confirmed by the RBM frequencies (see the text), it can be concluded that the 532 nm and 633 nm laser lines excite semiconducting (green) and metallic (red) SWNTs, respectively.

G- peak can show in some cases a Breit-Wigner-Fano (BWF) function<sup>81</sup>, namely:

$$I_{\omega} = I_0 \frac{\left[1 + \frac{(\omega - \omega_{BWF})}{q\Gamma}\right]^2}{1 + \left[\frac{(\omega - \omega_{BWF})}{\Gamma}\right]^2} \quad (\text{I.4.2})$$

in which  $I_0$ ,  $\omega_{BWF}$ ,  $\Gamma$  and  $q^{-1}$  are respectively: height, center, width and shape. This last parameter gives the asymmetric aspect of the BWF function.

Diameter and chirality must be determined to characterize SWNTs. It is known experimentally that the G+ peak varies very little with the diameter whilst the G- peak shifts to lower frequencies as the nanotube diameter decreases. This result is well summarized by fig. 1.12, obtained from a experimental study over several individual SWNTs<sup>73</sup>. The curves shown in fig. 1.12 are fitted by the equation:

$$\omega_{G-} = 1591 - \frac{C}{d_t^2} \quad (\text{I.4.3})$$

with  $C = 47.7 \text{ cm}^{-1} \text{ nm}^2$  for semiconducting and  $C = 79.5 \text{ cm}^{-1} \text{ nm}^2$  for metallic SWNTs. Roughly, lower the G- frequency, smaller the diameter. Thus, for characterization proposes from the G-band, the difference of frequency of G+ and G- gives an approximation of the diameter and the line shape of G- peak may indicate metallic or semiconductor behavior. Nevertheless, some remarks are made by some studies on the usage of eq. I.4.3 for diameter calculation<sup>82,83</sup>.

Another Raman active mode arises from the symmetry breaking upon the rolling up of the graphene sheet. It consists in the coherent, in-phase vibrations of the atoms in the radial direction of the tube, as illustrated in fig. 1.10. It is called Radial Breathing Mode (RBM) and its Raman frequency  $\omega_{RBM}$  lies in between 100-400  $\text{cm}^{-1}$ <sup>61,73,84</sup>. The RBM spectrum of a single nanotube (the same one of the G-band example) is shown in fig. 1.9.

Both theory and experiments<sup>85-87</sup> have been shown that  $\omega_{RBM}$  depends on the inverse of the nanotube diameter  $d_t$ . Classic elastic theory applied to a tubule shell gives:

$$\omega_{RBM} = \frac{C}{d_t} \quad (\text{I.4.4})$$

in which  $C = 227$ . However, this relation diverges from experimental data and therefore other equations have been proposed. An often used relation to tune the dependence on  $d_t$  through experiments is given by:

$$\omega_{RBM} = \frac{A}{d_t} + B \quad (\text{I.4.5})$$

in which  $A$  and  $B$  are adjustable parameters, having different values accordingly to sample conditions and environment.  $A = 248$  and  $B = 0$  were proposed for isolated SWNTs growth by CVD over silicon substrates<sup>88,89</sup>,  $A = 234$  and  $B = 10$  for bundles<sup>85,86</sup>. These  $A$  and  $B$  values applied in eq. I.4.5 give the curves shown in fig. 1.12. For SWNTs have small diameters, the proximity of the carbon atoms redistributes the  $\text{sp}^2$  bonds. As consequence, the chiral angle influence is not negligible anymore. To account for small  $d_t$ , the inclusion of a term in the equation I.4.5 was proposed<sup>90</sup>:

$$\omega_{RBM} = \frac{A}{d_t} + B + \frac{C + D \cos(3\theta)^2}{d_t^2} \quad (\text{I.4.6})$$

Unfortunately, tuning all the four parameters through experiments can be very difficult. Thus, the equation I.4.5 is still of use in experimental works<sup>10,91</sup>. It must be remarked that characteristics of the sample and the environment must be observed while choosing any of these relations and parameters. Even for the case of samples having many tubes present, one still can use these relations to estimate roughly the diameter distributions. Also, the evaluation of  $d_t$  from  $\omega_{RBM}$  is much more accurate than that given by the G-band features in eq. I.4.3, which is mainly tested for individual nanotubes laid on silicon substrates.

The signal intensity from Raman effect is weak. Considering the very small Raman cross-section of CNTs, resonance conditions must be matched to have their Raman spectra measurable. Often, if one speaks of Raman spectroscopy applied to CNTs, it means Resonance Raman Scattering (RSS) instead of the non-resonant Raman effect. If  $\Delta E$  is the energy which separates two electronic states, there are two possibilities to achieve resonance

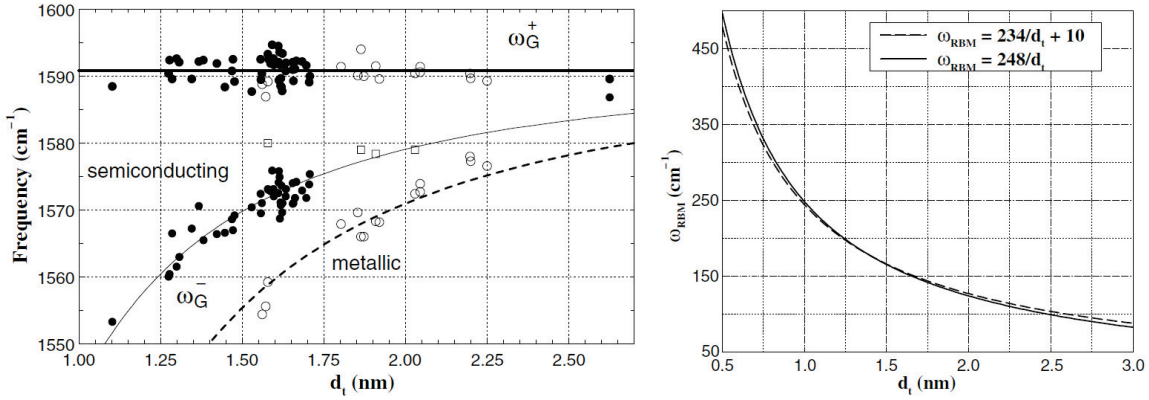


FIG. 1.12: Dependence on diameter of the G-band (a) and RBM (b) features<sup>73</sup>.

conditions. First, if the incident photon energy,  $E_I = \hbar\omega_I$ , is equal to  $\Delta E$ . Second, if the scattered photon energy,  $E_S = \hbar\omega_S$ , is equal to  $\Delta E$  plus the phonon energy,  $E_P = \hbar\omega_P$ , involved in the scattering process. For CNTs,  $\Delta E$  can be any of the  $E_{ii}$  energies which separate two vHS.

The phonon energies of RBM and G-band are  $\sim 20$  meV and  $\sim 200$  meV respectively. Considering a resonance window of  $\sim 10$  meV, the second condition of resonance cannot be achieved at the same time for both RBM and G-band. Therefore, the excitation energy must match an  $E_{ii}$  to study the RBM and the G-band spectra altogether.

Apart from RBM and G-band, there are other features which can be seen in the Raman spectra of carbon nanotubes. Structural defects in the nanotube wall arise a band  $\sim 1350\text{cm}^{-1}$ , called D-band, or disorder band. It has an overtone  $\sim 2700\text{cm}^{-1}$ , called 2D-band. The Raman shift of D and 2D bands varies with the excitation energy about  $53\text{cm}^{-1}\text{eV}^{-1}$  and  $106\text{cm}^{-1}\text{eV}^{-1}$ , respectively<sup>81</sup>. They are credited to second order, double resonance effect<sup>86</sup>. Both D and 2D bands are present in other carbon based materials, for instance, graphene and graphite. For characterization purposes, D-band carries information on disorder or defects present in the carbon wall whilst 2D-band is sensible to chemical effects, doping and charge transfer.

## I.5 HIGH-PRESSURE PHYSICS APPLIED TO CARBON NANOTUBES

The cross-section of bundled carbon nanotubes can assume different shapes, which is attributed to van der Waals interactions among the CNTs sharing their vicinities<sup>92,93</sup>. Among the possible geometries, a slight polygonal shape was reported by synchrotron x-ray diffraction allied to first principle calculations<sup>94</sup>. The same study suggested that pressure application would enhance the polygonal aspect (called polygonization), which neutron diffraction

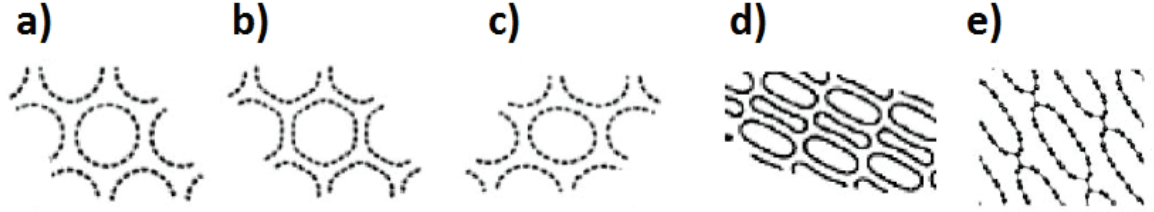


**FIG. 1.13:** Radial cross-section shapes of bundled SWNTs<sup>103</sup>. (a) Circular. (b) Polygonized, showing hexagonal cross-section shape. (c) Ovalized. (d) Racetrack and peanut shapes interleaved. (e) Racetrack interlinked.

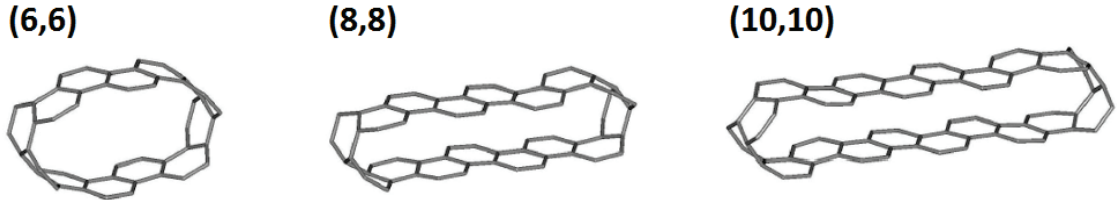


**FIG. 1.14:** Results from DFT calculations showing the unit cell aspect of collapsed SWNTs<sup>99</sup>.

studies confirmed later<sup>95,96</sup>. Upon pressure, shear strain<sup>97</sup> and buckling<sup>98</sup> are expected to change the radial cross-section of CNTs. Further studies done by Density Functional Theory (DFT)<sup>99–101</sup> and Molecular Dynamics (MD) simulations<sup>102</sup> have been suggesting that the cross-section can evolve to polygon, oval, racetrack, peanut and dog bone like shapes, as illustrated in fig. 1.13.

The flattest possible shape of the radial cross-section defines the collapsed phase (or the collapse) of a carbon nanotube. While collapsed, CNTs having large diameter can show a flat like aspect, whilst those having small diameters are mechanically limited to show racetrack or elliptical shapes. As examples, the collapsed unit cells of a few SWNTs are shown in fig. 1.14. The pressure threshold to achieve the collapse was predicted to dependent on the inverse of the diameter<sup>104–106</sup>. This dependence was suggested to follow a  $d_t^{-3}$  law<sup>55</sup>, having the most current corrections given by DFTB calculations<sup>107</sup>.

Collapsed CNTs were experimentally observed at ambient pressure<sup>39,108</sup>. The HRTEM<sup>2</sup> image in fig. 1.15 show different collapsed CNTs, having diameters  $\sim 4.2$ -6.9 nm. This collapsed phase agrees with theoretical predictions, for which a diameter  $\geq 4.16$  nm would auto-collapse accordingly to a  $d_t^{-3}$  law<sup>55</sup>. Moreover, SWNTs lying on substrates are expected to experience a radial deformation, which has evidence on both experiments<sup>44</sup> and molecular dynamics simulations<sup>109</sup>. Albeit the collapsed phase is demonstrated for large diameters, the evolution of the cross-section under pressure and the threshold to reach a

<sup>2</sup>High resolution transmission electron microscope.

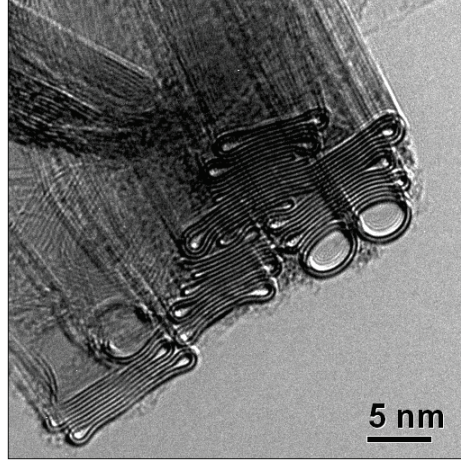


**FIG. 1.15:** HRTEM image show collapsed single (center), double (bottom-left) and triple (upper-right) wall carbon nanotubes. Slight oval shaped DWNTs can be seen in middle-left<sup>39</sup>.

collapsed phase are still experimentally unsettled.

SWNTs derived from diverse methods of synthesis have been studied by high-pressure Raman spectroscopy: DPLA<sup>110</sup>, LA<sup>111</sup>, PLV<sup>112–115</sup>, AD<sup>21,49,54,113,114,116–122</sup>, HiPco<sup>84,104,123–126</sup> and CoMoCAT<sup>127</sup>. In a few words, these studies collect Raman spectra at different pressures, fit functions to the peaks to obtain frequency, FWHM and intensity, then analyze these parameters as functions of pressure. In addition, modification, onset or vanishing of spectral features with the increasing pressure are highlighted.

Some high-pressure studies on SWNTs reported a total loss of RBM resonance  $\sim 1.5$ <sup>112</sup>,  $1.7$ <sup>111</sup>,  $1.8$ <sup>113</sup> and  $2.6$  GPa<sup>49</sup>. This loss of RBM was suggested to be consequence of a phase transition. In some of the mentioned studies, the loss of RBMs was shown concomitant to a lowering of the pressure derivative of the G-band ( $\alpha_G$ ), which supported the suggestion of a phase transition. However, other studies did not confirmed any onset of transition at such low pressures<sup>54,93,118,128</sup>.

A good advance was given by an investigation relying on X-ray and Raman spectroscopy to probe pressure effects on bundled SWNTs. This study reported a loss of a diffraction peak (observed in fig. 1.16a) concomitant to a change of  $\alpha_G$  value (seen in fig. 1.16b)  $\sim 2$  GPa. This event was assigned to a phase transition induced by pressure, being interpreted as a modification of the radial cross-section<sup>21</sup>. Nevertheless, other investigations reported the onset of transitions at much higher pressures.

After a study on HiPco derived SWNTs, fig. 1.17 shows the most intense peak of the G-band (upper curve) as a function of pressure. The G-band shifts to higher frequencies up to  $8.1$  GPa, from which its frequency levels off  $\sim 1650$   $\text{cm}^{-1}$ , assuming a new but lower rate blue-shift  $\sim 15$  GPa. In addition to the experimental result, this study carried calculations

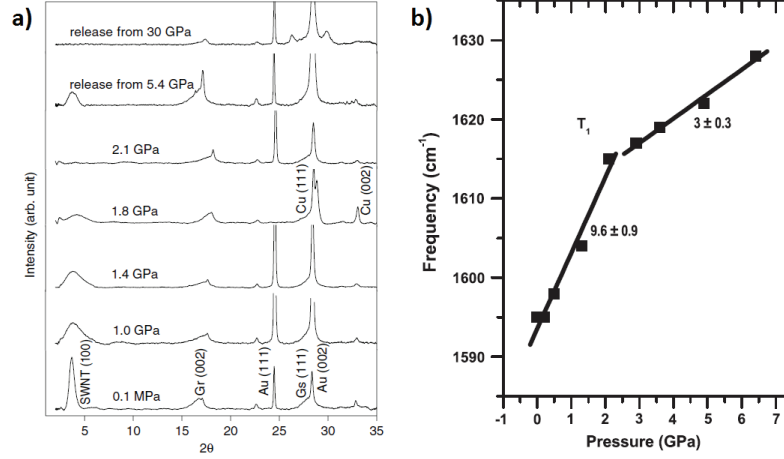


**FIG. 1.16:** Evidence of cross-section modification induced by pressure<sup>21</sup>. a) X-ray diffraction measurement under pressure. The peak corresponding to the SWNT bundle disappear at about 2.1 GPa. b) The most intense peak of the G-band as function of pressure. The change of slope  $\sim 2$  GPa in this curve corresponds to the loss of intensity in X-ray measurements. Solid lines are linear fits, for which the corresponding values of  $\alpha_G$  are labeled.

to verify how the G-band frequency evolves while the edges of a SWNT approach each other, which is expected to happen with the volume reduction induced by pressure. The results are shown in fig. 1.17. Upon the initial volume reduction, the G-band frequency blue-shifts. However, as the distance between the two edges reach values compatible with a collapsed geometry, the G-band frequency levels off. Therefore, this leveling (plateau) seen for G-band evolution was assigned to the onset of the collapse<sup>124</sup>.

Other evidences of collapse were found by different authors. Figure 1.18a shows the evolution of the G-band for SWNTs<sup>53</sup>,  $C_{70}$ @SWNTs<sup>53</sup> and DWNTs<sup>51</sup> respectively in orange, red and blue colored curves<sup>3</sup>. For these three samples, with enough pressure, the blue-shift trend turns to red-shift. Since the blue-shift of the G-band frequency (related to the C-C bond hardening) is the expected response to the increasing pressure, the red-shift (C-C bond softening) would require a change in the curvature of the nanotube wall. Therefore, the inflection point marking the change of trend was interpreted as a signature of collapse. Moreover, highlighting that  $C_{70}$ @SWNTs and AD SWNTs having similar diameters show different collapse thresholds, respectively  $\sim 8$  GPa and  $\sim 15$  GPa (see fig. 1.18), it was suggested that filling has a important role on the structural stability of CNTs<sup>53</sup>.

Effect of filling was reported by other experimental investigations. Figure 1.18b show the pressure response of the Raman modes of I@SWNTs<sup>4</sup>. The leveling of the G-band  $\sim 8$ -9.5 GPa suggests the onset of collapse, resembling the results obtained for  $C_{70}$ @SWNTs<sup>52</sup>.

<sup>3</sup> $C_{70}$ @SWNTs means SWNTs filled with fullerenes, also called  $C_{70}$  peapods.

<sup>4</sup>SWNTs filled by polyiodides,  $I^m$  molecules.

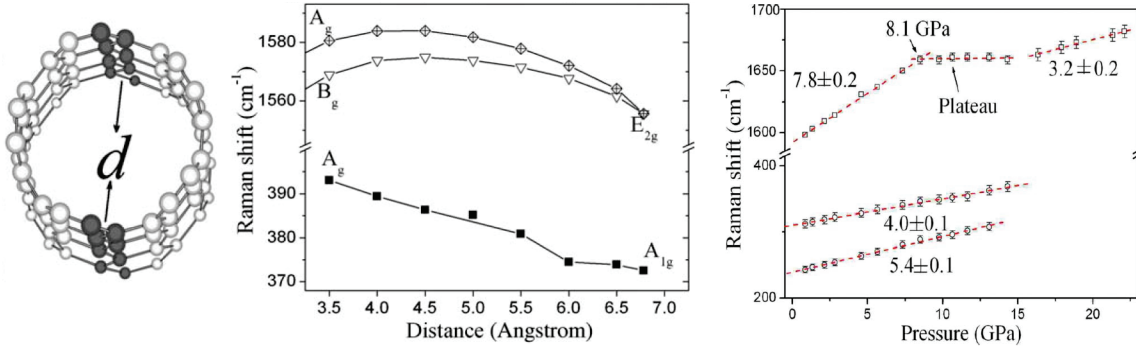


**FIG. 1.17:** Evidence of collapse in CNTs<sup>124</sup>. a) The nanotube construction, in which  $d$  is the shortest distance between edges of the tube. b) The calculated phonon frequencies as functions of  $d$ . c) The experimental phonon frequencies of G-band and RBM. The pressure slopes are labeled, as well the threshold at 8.1 GPa, assigned to the onset of the collapse.

Not only Raman, but also results of absorption spectroscopy on SWNTs and C<sub>60</sub>@SWNTs suggested that filling increase the pressure threshold of a phase transition from 3 to 6.5 GPa in a nitrogen environment, or from 2.5 to 5.5 GPa upon changing the PTM to argon<sup>130</sup>. Moreover, this same study shown a phase transition around 12 GPa for both SWNTs and C<sub>60</sub>@SWNTs samples.

Addressing the inner SWNT of a DWNT as a filler to the outer SWNT, the presence of the inner tube was suggested to provide structural support to the outer tube<sup>131</sup>. High-pressure investigations reported the redshift of the absorption bands of DWNTs were smaller than of empty SWNTs, suggesting that the inner tube provides structural stability<sup>47</sup>. From another study, DWNTs having the outer shell diameter  $\sim 1.56$  nm were found to collapse  $\sim 25$  GPa<sup>51</sup>. Accordingly theoretical predictions within a  $d_t^{-3}$  law, an empty SWNT having such diameter would collapse at pressures below 4 GPa<sup>55</sup>, thus confirming that the inner tube provides stability against pressure.

Another important variable to be considered while studying CNTs is the environment. Aside of pressure, interactions between SWNTs and the media containing them are expected to shift the resonance energies. Among the reported studies, one performed on chirality resolved SWNTs shown that the shifts of both energies and RBM frequencies did not shared a trend. Therefore, the shifts were suggested to be chirality dependent<sup>50</sup>. Straightforwardly, this suggest that the environmental effects are particular for each SWNT.

From a high-pressure experiment performed on AD SWNTs, fig. 1.19a shows the G-band spectra in paraffin, methanol:ethanol and argon environments and fig. 1.19b shows the corresponding evolution of the most intense peak of the G-band. It can be verified in both graphs that for close values of pressure, the line width broadening (a) and the response of the G-band frequency (b) change substantially from a PTM to another. Therefore, the

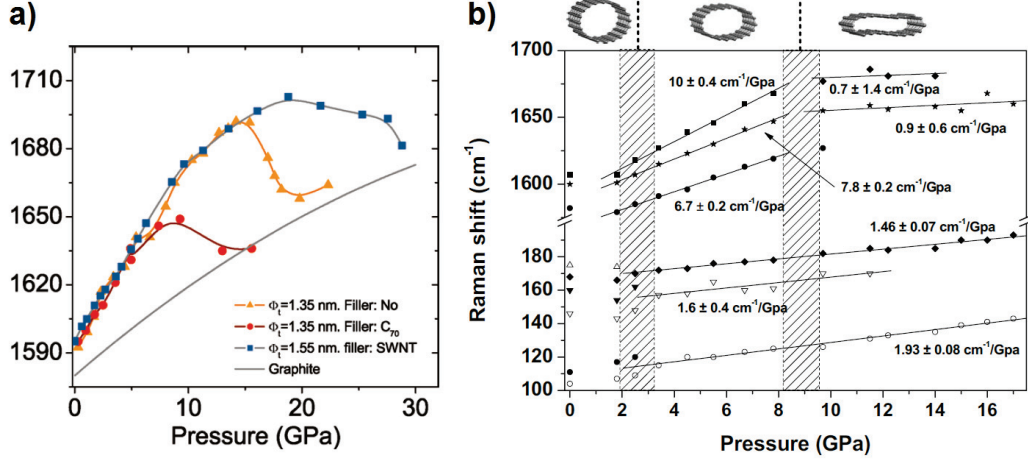


**FIG. 1.18:** a) The most intense peak of the G-band as a function of pressure. Peapods<sup>53</sup>, SWNTs<sup>54</sup>, DWNTs<sup>51</sup> and Graphite<sup>129</sup> are respectively shown in red, orange, blue and grey colors. Solid lines are guides to the data points. b) Raman modes as functions of pressure for I@SWNTs<sup>52</sup>. Highlighted regions in the graph indicate the suggested shape (sketched at the top) of the SWNTs at different pressures. Labels give the values of the pressure derivatives.

pressure response was suggested to depend on the PTM<sup>54</sup>. A strong suggestion of PTM effect was also found lately in a study on chirality resolved samples, which reported different pressure shifts for the G-band under hexane and water environments<sup>127</sup>.

Regarding hydrostatic conditions, it was proposed that liquid and solid environments would give respectively isotropic and anisotropic compression, affecting the threshold of the pressure induced transition for SWNTs<sup>128</sup>, but conversely for DWNTs, a better hydrostaticity is suggested to decrease slightly the transition pressure<sup>132</sup>.

Following some other studies, the dependence on environment for the pressure response may be questioned. Absorption spectroscopy under pressure using helium, argon, CsI and methanol:ethanol mixture as PTMs shown that AD SWNTs would have their cross section changed from circular to oval  $\sim$  2-3 GPa, in despite of the different PTMs used<sup>133</sup>. The contradiction among the results considering the PTM effect can be due to entanglement between pressure and electronic contributions. Also, samples have different distribution of defects, which are not evaluated in-situ. A good example is given by a study on bundled DWNTs intercalated by bromine<sup>134</sup>, for which the collapse pressure was lowered from 21 to 13 GPa in respect to a previous investigation also carried on DWNTs<sup>51</sup>. The two samples were derived from different synthesis. Therefore, the observed lowering of the collapse threshold could be explained by either PTM effect or larger distribution defects<sup>134</sup>. Moreover, the electronic shift of energies could select different resonance conditions.

Diameter is considered the ruling parameter to the collapse by the majority of theoretical predictions. However, calculations for different CNTs having diameter  $\sim$  1.35 nm

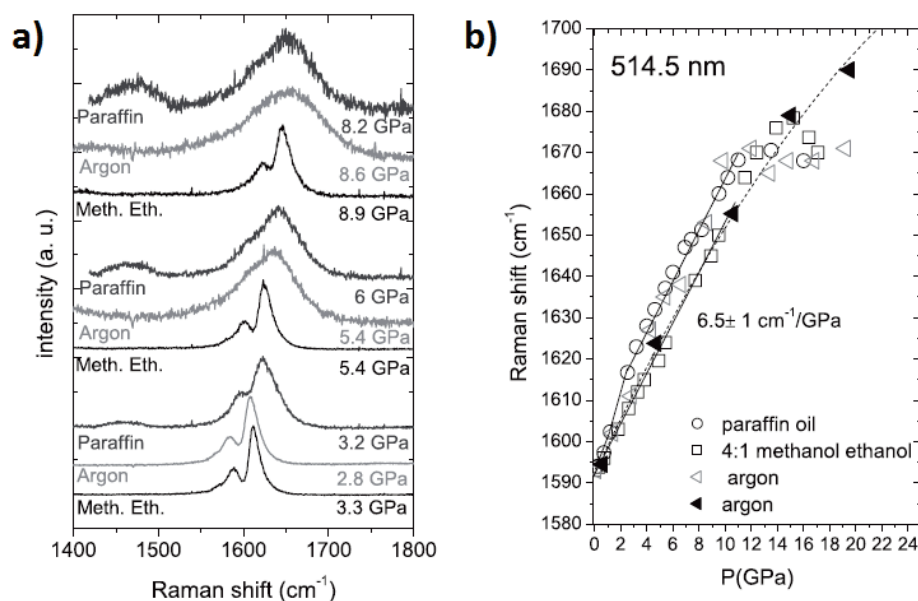


**FIG. 1.19:** Panels *a* and *b* refer to studies done for the same AD sample with 514.5 and 632.8 nm wavelengths respectively. In each panel, the graph at left show G-band spectra collected at different pressures, the graph at right show the G-band Raman shift (its most intense peak) as a function of pressure. The labels indicate the PTM used for each experiment<sup>54</sup>.

found their collapse pressures ranging from 5.5 to less than 1 GPa, suggesting a chirality dependence to the collapse<sup>56</sup>. As discussed in previous section, assignment of chiralities through Raman is made through RBM frequency. Nevertheless, the majority of the high-pressure studies on CNTs were performed in bundles, whose RBMs cannot be resolved. It was demonstrated that optimal unbundling of CNTs can be achieved through nanotube:surfactant:water solutions<sup>78</sup> and further developments provided the separation of diameters, allowing accurate (n,m) chirality assignment<sup>79</sup>. At least one high-pressure Raman study on surfactant-individualized (sodium cholate:water) CNTs managed to furnish pressure derivatives of RBM ( $\alpha_{RBM}$ ) for individual chiralities<sup>84</sup>. The same study found that SDBS:water:CNTs deposited on glass microfiber shown similar  $\alpha_{RBM}$ . These values were found ranging from 5.2 to 8.2  $cm^{-1}GPa^{-1}$ , which overlap the lowest values of measurements performed in bundles.

Early results suggested that inter-tube (van der Waals type) interactions in bundles would have a meaningful influence on the response to pressure of CNTs, especially at lower pressures<sup>135</sup>. Nevertheless, approximate values of  $\alpha_{RBM}$  were reported for bundled<sup>123,126</sup> and surfactant-individualized<sup>84</sup> SWNTs. After this observation, it was suggested that effects of bundling are less influential to the pressure response of CNTs<sup>126</sup>.

Generally, the pressure induced shifts reported for Raman frequencies and absorption

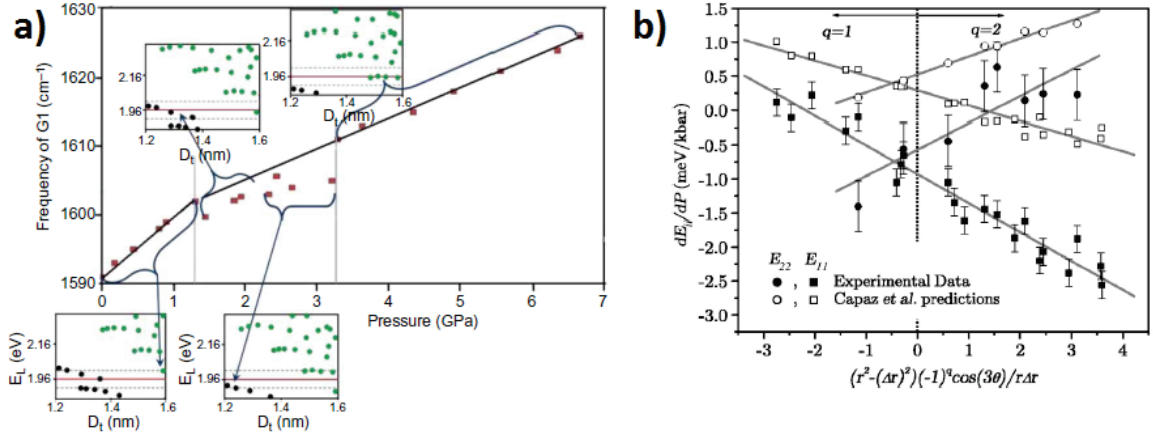


**FIG. 1.20:** a) The most intense peak from the G-band as a function of pressure<sup>136</sup>. b) Energy shifts as a function of pressure<sup>48</sup>.

bands are consequence of changes of the electronic properties. Dispersion of nanotubes in solutions enabled photoluminescence (PL) experiments to be carried for individual chiralities. PL excitation and emission probes the  $E_{11}$  and  $E_{22}$  transition energies, thus giving insight on the electronic structure. The first attempts of evaluate the evolution of PL spectra under pressure found broadening and loss of intensity, in accordance to the observations of RBMs in Raman spectroscopy<sup>84</sup>. Shortly after, a high-pressure study on CNTs dispersed in SDBS:water solution managed to determine the shift with pressure of  $E_{11}$  and  $E_{22}$ <sup>48</sup>. These shifts ( $dE/dP$ ) are plotted in figure 1.20b, which x axis has a dependence proposed by theory<sup>42</sup>. This result shows clearly that pressure shift the Kataura plot as it shifts the transition energies.

These investigations also revealed that in despite of recovered features, some degree of irreversible changes in Raman and PL appeared in lower pressures. Non reversibility would then be linked to structural defects due to the applied pressure. Evaluation of sample quality in CNTs is often done through D-band analysis. It is important to remind that diamond has a peak  $\sim 1350\text{cm}^{-1}$ , thus D-band cannot be followed in-situ in a DAC. Ex-situ high-pressure Raman can be carried out on CNTs. In this case, one compares spectra measured before and after applied pressure. One advantage of ex-situ use is the possibility of evaluating the defects generated by pressure through the D-band analysis. For instance, the recoverability and resilience of CNTs can be studied after extreme compression, as done by shock wave experiments in DWNTs<sup>137</sup>.

One more factor to be considered while studying CNTs at high-pressure is the presence of different SWNTs in the investigated sample. As demonstrated by the results shown in fig. 1.20a, different SWNTs can be resonance with the increasing pressure. The explanation

is that as the electronic dispersion depends on the structure, radial deformation changes the vHS and consequently shifts the resonance energies<sup>136</sup>. Another example was given by Triple Wall Carbon Nanotubes (TWNTs) samples, for which even different tubes belonging to a same TWNT were found in resonance at different pressures<sup>138</sup>. This pressure selectivity of resonance conditions may be one of the reasons why high-pressure studies on CNTs give contradictory results, often being difficult to be interpreted.

To summarize this bibliographical review, the response to pressure of CNTs is suggested as dependent on several variables: environment, filling, diameter and possibly on chirality and distribution of defects. All reviewed high-pressure studies were performed on samples derived from different synthesis, namely: Arc discharge<sup>77</sup>, High Pressure CO Conversion (HiPco)<sup>139</sup>, Chemical Vapor Deposition (CVD)<sup>140</sup>, Double-pulse Laser Ablation (DPLA)<sup>141</sup>, Laser Ablation (LA)<sup>142</sup>, Pulsed Laser Vaporization (PLV)<sup>143</sup> and Co-Mo Catalysis (CoMoCAT)<sup>144</sup>. These techniques provide CNTs having different diameter distributions, chiralities, lengths and distribution of defects. The nowadays difficulties to synthesize samples having individually chosen species of CNTs and the need to consider the many external and intrinsic parameters involved on the pressure stability explain why the results reported in literature still cannot satisfactory bridge theory and experiments on the subject.

## CHAPTER II

### SAMPLES AND EXPERIMENTAL SETUP

This chapter describes single wall carbon nanotubes samples, Raman and high-pressure experimental setup and methods used to perform the experiments which comprise this thesis work. Synthesis of samples were prepared by Sofie Cambré and Wim Wenseleers from University of Antwerp. Their methodology will be summarized for quick reference as it is well described in literature<sup>10,11,78,79</sup>. For reading easiness, characterization of samples by Raman spectroscopy is shown at same time as description of preparation methods. Subsequently, it is shown a summary on equipment and configuration. The methods applied to the data treatment are also presented.

#### II.1 SAMPLES

The first sample was prepared as follows. Surfactant:water solution was prepared by adding sodium deoxycholate (DOC) to D<sub>2</sub>O. Powdered, raw HiPco SWNTs were added to the solution and the mixture was stirred for several days. Stirring facilitates the wrapping of surfactant molecules around the nanotubes, separating them from bundles and thus providing individualization. Additional centrifugation treatment (16215 g during 24h) separated individual SWNTs from any remained bundles. The Raman spectrum of this sample is shown in fig. 2.1a.

It is experimentally demonstrated that open SWNTs in water environment become completely filled by water molecules. As consequence of water-filling, the RBM frequency shifts to a higher value (blue-shifts) and the RBM line width broadens slightly<sup>11</sup>. Therefore, each of the three pair of peaks in fig. 2.1a comprises two RBM resonances of a same (n,m) chirality. The red colored, lower frequency peak is given by RBM resonances of empty SWNTs whilst the blue colored, higher frequency peak comes from RBM resonances of water-filled SWNTs.

The RBM frequencies ( $\omega_{RBM}$ ) obtained by Lorentzian fittings were used to evaluate the diameters through eq. I.4.5, with the parameters A and B given by the literature<sup>10</sup>. For empty tubes, A = 221.8 and B = 11.2. For water-filled, A = 220.8 and B = 14.5. The diameters were then used for the chirality assignment through the Kataura plot shown in fig. 2.2. The 2.18 eV energy indicated by the horizontal orange colored line corresponds to the 568.5 nm wavelength used to measure the RBM spectra. The obtained diameters of 0.75, 0.68 and 0.64 nm which are closer to 2.18 eV match the  $E_{22}$  transition of (6,5), (6,4) and (7,2) chiralities, respectively. For easiness in further reading, this sample will

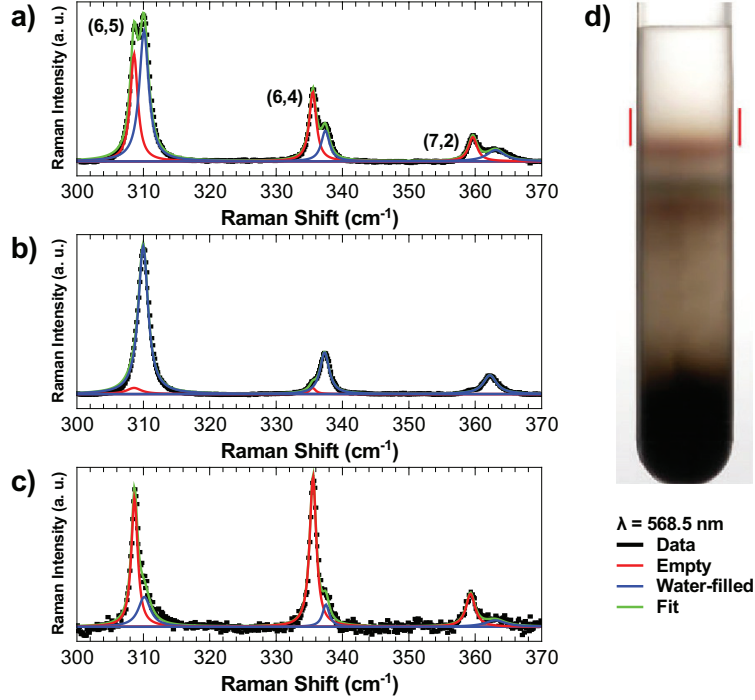


**FIG. 2.1:** High resolution RBM spectra of HiPco derived samples at 568.5 nm wavelength. Black dots are data points. Red and blue colored lines are Lorentzian fittings of empty and water-filled SWNTs, respectively. Green line shows the data fit. Labels name the  $(n,m)$  chiralities. (a) HiPcoM, mixed empty and water-filled SWNTs. (b) HiPcoF, mostly water-filled SWNTs. (c) HiPcoE, mostly empty SWNTs. (d) Photograph of the DGU tube. The two vertical lines indicate the portion from which empty SWNTs were extracted.

be referred as HiPcoM. The 'M' suffix means that it has a mix of empty and water-filled SWNTs at akin ratios for the mentioned chiralities.

The second sample was prepared from purified HiPco SWNTs, which were annealed by high-temperature vacuum treatment to remove residual materials used during the purification procedure. Then, the nanotubes were individualized by DOC solution, similarly to HiPcoM sample. As the purification opens the SWNTs, they became entirely filled with water during solubilisation procedure. To ensure a maximum concentration of individualized SWNTs, the solution was treated by bath sonication for 1h. Raman spectrum of this sample is shown in fig. 2.1b. To fit this spectrum accurately,  $\omega_{RBM}$  and  $\Gamma_{RBM}$  (RBM line width) of both empty and water-filled SWNTs were compared with those of HiPcoM sample (fig. 2.1a). Then, features corresponding to (6,5) and (6,4) chiralities were both fitted by two peaks. Nonetheless, the (7,2)  $\omega_{RBM}$  and  $\Gamma_{RBM}$  values match those of the HiPcoM (7,2) water-filled uniquely, thus requiring only a single Lorentzian for the fitting. For this sample, the blue-shifted RBMs are much stronger in intensity than those having

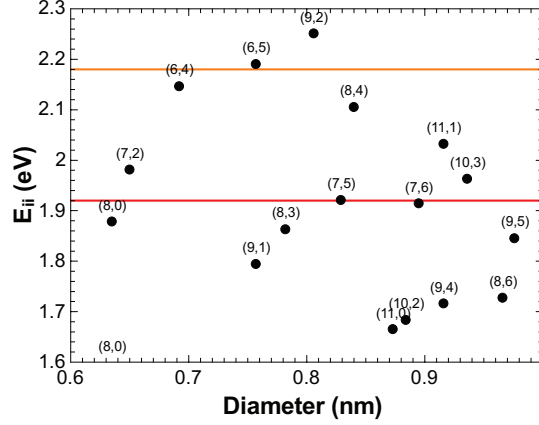


**FIG. 2.2:** Kataura plot<sup>145</sup>. The orange and red colored lines cross the 2.18 eV and 1.92 eV energy values corresponding to the 568.5 nm and 647.1 nm wavelengths, respectively.

frequencies compatible to the empty state, indicating the presence of mostly water-filled nanotubes. Thus, this sample is named HiPcoF ('F' meaning filled with water) for reference in next comparisons.

A third sample was prepared after HiPcoM, by treating it with Density Gradient Ultracentrifugation (DGU). For that, the iohexol gradient medium was diluted in  $D_2O$  by proper methods. Then, HiPcoM sample was added up and centrifuged (122000 g) during 48h. The photograph in figure show the centrifuge tube after the procedure. Lower density portions floating on top were extracted by a syringe. The Raman spectrum of this sample is shown in fig. 2.1c. Fittings were done by comparing  $\omega_{RBM}$  and  $\Gamma_{RBM}$  of all three samples. The overall higher intensity of RBMs show that this third sample has mostly empty nanotubes. Therefore, alike other samples, this one is named HiPcoE ('E' meaning empty).

As illustrated by the data in figures 2.1 a-c, the active RBMs at 568.5 nm have  $\Gamma_{RBM} < 2cm^{-1}$ . Such sharpness is achieved only if the RBM resonances belong to individualized SWNTs, which assures the optimal solubilisation. This fact also excludes any inter-tube interactions asserted to bundling. Although, surfactant-tube interaction still exists, unfortunately it cannot be separated from water-tube (environment-tube) interaction. Up to date, this kind of precise RBM separation is achievable only through proper bile salt surfactant treatment allied to high resolution Raman spectroscopy.

HiPcoF and HiPcoE samples were also probed with 647.1 nm wavelength in order to study different SWNTs. Their Raman spectra are show in fig. 2.3a. The blue-shifting due to water-filling is again noticeable for the HiPcoF spectrum. Figures 2.3b and c show the detailed peak fitting of HiPcoF and HiPcoE samples, respectively. The assignment of chiralities was carried out similarly to the procedure described for the measurements at

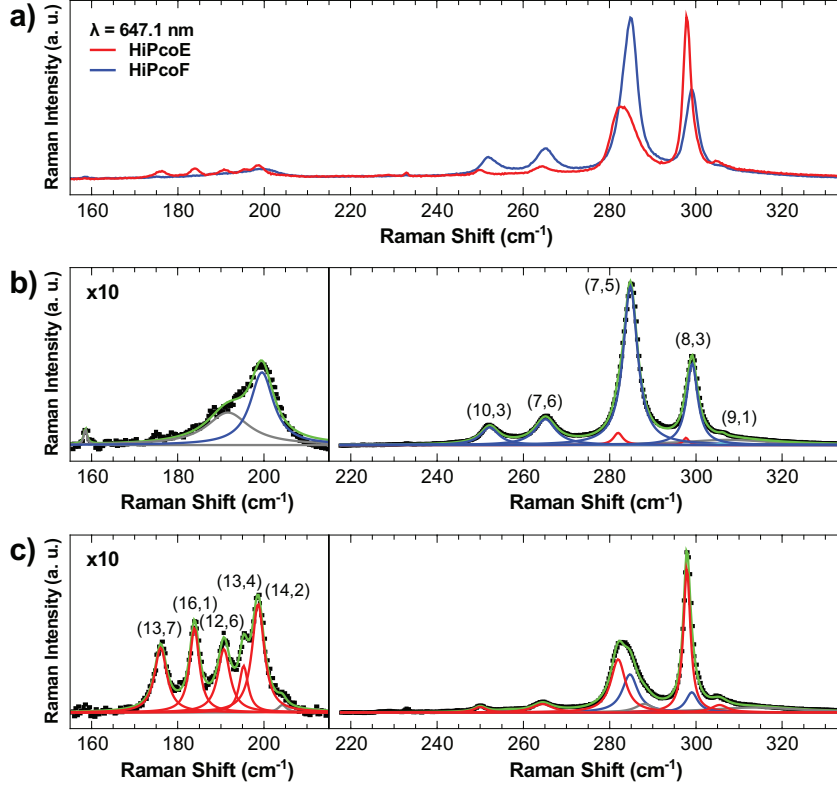


**FIG. 2.3:** RBM spectra of HiPco derived samples excited at 647.1 nm. Black dots are data points. Red and blue colors indicate empty and water-filled configurations. Chiralities are conveniently labeled. a) Superposed spectra of both samples. b) HiPcoF. c) HiPcoE.

568.5 nm. Given the frequencies shown in the left panels (x10 magnified), one has: (13,7), (16,1), (12,6), (13,4) and (14,2) SWNTs, all metallic, having a diameter distribution of  $1.26 \pm 0.1$  nm. Although, for the water-filled sample, only the (14,2) is resolved. Given the frequencies shown in the right panels, one finds: (10,3), (7,6), (7,5), (8,3) and (9,1) SWNTs, all semiconducting, whose averaged diameter is  $0.82 \pm 0.1$  nm. The RBMs of (10,3) and (7,6) for both HiPcoF and HiPcoE can be fitted each by a single peak, resulting larger and blue-shifted RBMs for HiPcoF, as expected by the water-filling. Nonetheless, observing that RBMs of water-filled SWNTs of a same chirality must be always wider and blue-shifted in respect to the empty counterpart, the RBMs of (7,5) and (8,3) must be fitted by two peaks. Therefore, regarding (7,5) and (8,3) chiralities, HiPcoF has an small amount of empty SWNTs, but HiPcoE has a non negligible amount of water-filled ones.

To study SWNTs having thicker and narrow diameter distribution, empty and water-filled samples were prepared by protocols similar to those applied for HiPco, but from Arc discharge derived SWNTs<sup>77</sup>. For simplicity, they will be named likewise others: ArcF (water-filled) and ArcE (empty). Their spectra are shown in fig. 2.4a and b. By the same

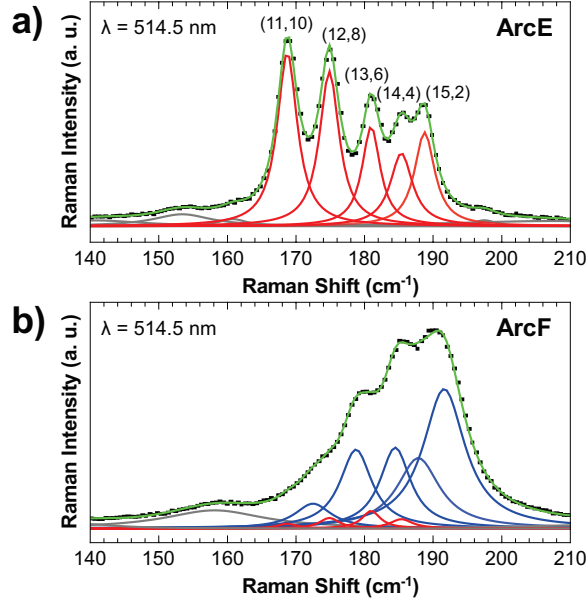


**FIG. 2.4:** RBM spectrum and respective chirality assignment of Arc derived samples. Wavelength for both was 514.5 nm. Data points are shown by black dots. Empty and water-filled configurations are shown in red and blue colors, respectively. Line shape fitting is shown in green color. Chiralities are labeled. a) ArcE. b) ArcF.

procedure applied to the HiPco samples, the diameter evaluation and chirality assignment of ArcE results: (11,10), (12,8), (13,6), (14,4) and (15,2), all of them semiconducting, having a diameter distribution of  $1.32 \pm 0.08$  nm. Important to remark for all these samples, empty and filled naming rely on the dominant configuration for practical use.

## II.2 MORE ON THE SAMPLES

A Raman spectrum covering a broader frequency window of HiPcoM sample (dark grey) is shown in fig. 2.5. In addition to the RBMs previously assigned to (6,5), (6,4) and (7,2) chiralities, there are also several RBM peaks  $\sim 200$ - $260$   $\text{cm}^{-1}$  resonant under 2.18 eV energy. They are too broad and entangled to be resolved individually to be assigned to individual chiralities. Their diameter distribution can be roughly estimated by applying the frequency range of their RBMs in eq. I.4.5, giving  $1.15 \pm 0.2$  nm.

An additional sample was prepared similarly to HiPcoM, though from a different batch of raw HiPco SWNTs. Its RBM spectrum at ambient pressure (light grey) is shown superposed to the one of HiPcoM in fig. 2.5. This additional sample has empty and water-filled (6,5), (6,4) and (7,2) SWNTs resembling HiPcoM, hence it is named HiPcoM'. Nevertheless, concerning the thicker diameters ( $\pm 200$ - $260$   $\text{cm}^{-1}$ ), the highest intensity RBM band

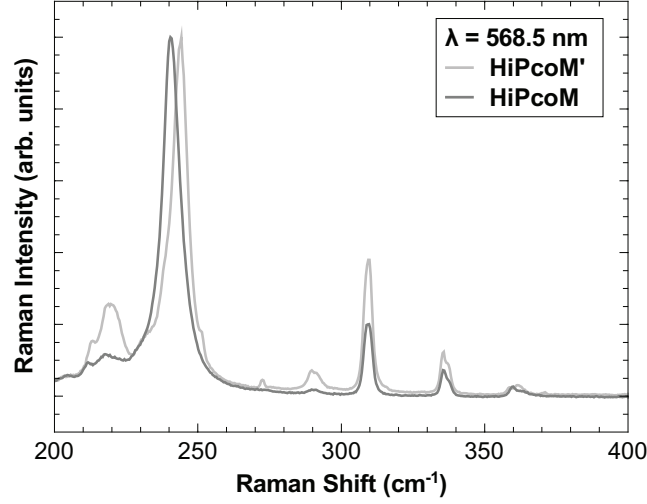


FIG. 2.5: RBM spectra of mixed empty and water-filled samples at 568.5 nm wavelength.

(peaked  $\pm 240 \text{ cm}^{-1}$ ) in HiPcoM is blue-shifted (peaked  $\pm 245 \text{ cm}^{-1}$ ) in HiPcoM'. Therefore, the thicker SWNTs are mostly empty in HiPcoM whilst they are mainly water-filled in HiPcoM'. In both samples, the lower frequency RBMs show much higher intensity in respect to the thinner (6,5), (6,4) and (7,2), suggesting that the SWNTs having the thicker diameters must dominate the G-band spectra of these samples.

The characterization of samples presented up to now relied only on RBMs. Even if they are enough to resolve chiralities, a complete study requires observation of the G-band. Figures 2.6 a to f show the G-band spectra of all samples, conveniently labeled in their respective graphs. The G+ feature is readily spotted  $\pm 1590 \text{ cm}^{-1}$  for all samples, being well fitted by one Voigt profile. The G- profiles however must be discussed for each sample.

HiPcoM' and HiPcoM show a broad G- profile, for which different sets of peaks (plus the G+ one) can provide a good line shape for the G-band. This impossibility to resolve the G- forbids any assignment to diameter distributions based on the frequency difference of G- and G+ peaks. Thus, regarding the G-band, only the line shape can be analyzed for these samples.

HiPcoF and HiPcoE show a large and flattened G- profile, which are much less intense than G+ and requires at least three Voigt peaks to be properly fitted. Curiously for these two samples, one of the three G- peaks (magenta colored in figures 2.6c and d) is found  $\sim 1580 \text{ cm}^{-1}$ , matching a peak occasionally observed for metallic SWNTs deposited on silicon substrates<sup>73</sup> or even in bundles<sup>120</sup>. Therefore, this peak will be assigned to the average  $d_t \sim 1.26 \pm 0.1 \text{ nm}$  of the metallic SWNTs. The remaining two G- peaks cannot be assigned. Other observation on the G-band of HiPcoF and HiPcoE is the lack of a BWF component

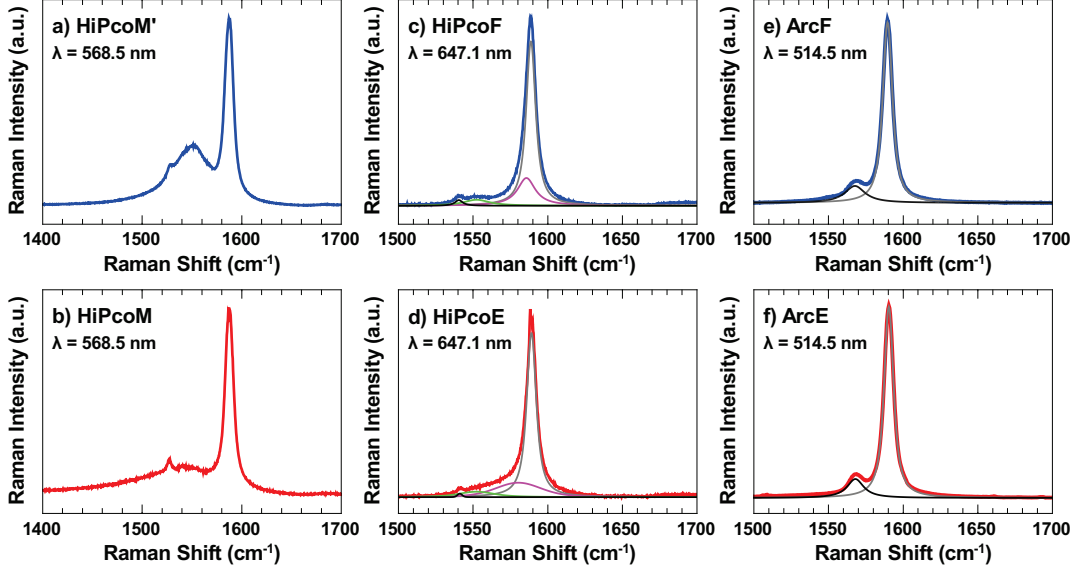


**FIG. 2.6:** *G*-band spectra of the studied samples. Blue and red colors follow the color code for mostly water-filled and empty SWNTs, respectively. When applicable, fitting components are shown in black, grey, green and magenta colors. Samples and wavelengths ( $\lambda$ ) used for the data acquisition are labeled. a) HiPcoM'. b) HiPcoM. c) HiPcoF. d) HiPcoE. e) ArcF. f) ArcE.

in spite of the presence of metallic SWNTs. This agrees with a statement that BWF component is an intrinsic feature of bundled metallic SWNTs<sup>82</sup>.

ArcF and ArcE show a single sharp band in their *G*- profile, thanks to the narrow diameter distribution and the resonance of only semiconducting SWNTs at the 514 nm wavelength. Therefore, their *G*- feature can be assigned to the averaged diameter distribution,  $d_t \sim 1.32$  nm.

### II.3 HIGH-PRESSURE SPECTROSCOPY SETUP

Experiments were performed at Lyon and Antwerp. Samples characteristics, spectrometer, optics and available wavelengths were considered for choosing the setup and facility. Lyon's setup is sketched in fig. 2.7a. The spectrometer comprises a single monochromator, a 1800 groves/mm grating and an air cooled CCD detector. Excitation energy was provided by a 514.5 nm wavelength Argon laser, which was focused in the sample through a 50x objective, giving a spot diameter of 2  $\mu\text{m}$ . Before each experiment, the calibration was adjusted by the two parallel mirrors installed after the laser output as show the sketch. Calibration of frequency shift was verified by the  $521\text{cm}^{-1}$  peak of a silicon wafer. A second notch filter was manually adjusted as needed. The spectral resolution at this setup is  $2\text{cm}^{-1}$ .

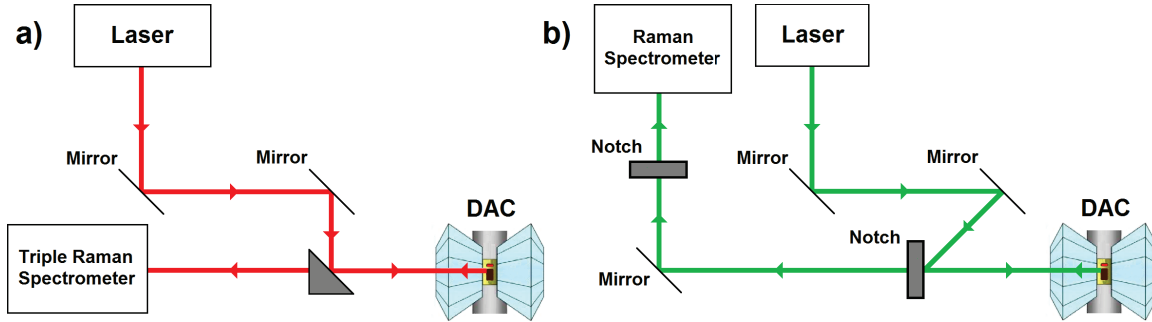


FIG. 2.7: High-pressure Raman spectroscopy setup. a) Antwerp. b) Lyon.

Antwerp's setup is sketched in fig. 2.7b. The Dilor XY800 spectrometer was equipped with a triple monochromator, 1800 groves/mm grating and liquid nitrogen cooled CCD detector. Three excitation wavelengths were available and were chosen accordingly to the diameters intended to be studied. 1) 568.5 nm, provided by a tunable Rhodamine 6G dye-laser pumped by an Argon laser. 2) 647.1 nm, given by a Krypton laser. 3) 514.5 nm, from an Argon laser. The output beam was focused in the sample through a photographic grade objective, which gives a large spot size and consequently provides more collection of scattered light as the laser beam is directed into a liquid volume. Specifically for this setup, the spectral resolution was settable. By setting a slit opening to 200  $\mu\text{m}$  or 50  $\mu\text{m}$ , the dispersion of light provided lower or higher resolution. Calibration in this setup was checked through sharp Raman peaks given by an halogen lamp.

For the HiPco derived samples, it was selected a DAC equipped with two 600  $\mu\text{m}$  culet size diamonds. The gaskets which lodged the samples in between the diamonds were individually prepared as follows. 1) A plate, 200  $\mu\text{m}$  thickness stainless steel disc was indented at its center down to  $\sim 100\mu\text{m}$  through the own DAC. 2) A 250 $\mu\text{m}$  diameter hole was opened at the center by electro erosion. 3) The hole was polished manually with a tungsten tip to remove residual metallic spikes. This configuration allows to increase the pressure up to  $\sim 15$  GPa over a 5 nl volume of sample.

Intending to study ArcF and ArcE samples at higher pressures, a second DAC having 350  $\mu\text{m}$  culet size diamonds was selected. A photograph of this is shown in fig. 2.8. Given these smaller culets, gaskets were similarly prepared but having adapted geometry: 200  $\mu\text{m}$  of initial thickness,  $\sim 40\mu\text{m}$  of indentation at their center and 125 $\mu\text{m}$  diameter hole. With this configuration, pressure can be increased up to 30 GPa, but over much less volume, 0.5 nl.

The procedure to load the DAC was similar for all experiments. A single and small ruby chip was installed over one diamond to probe the pressure. Each sample was dried by gently

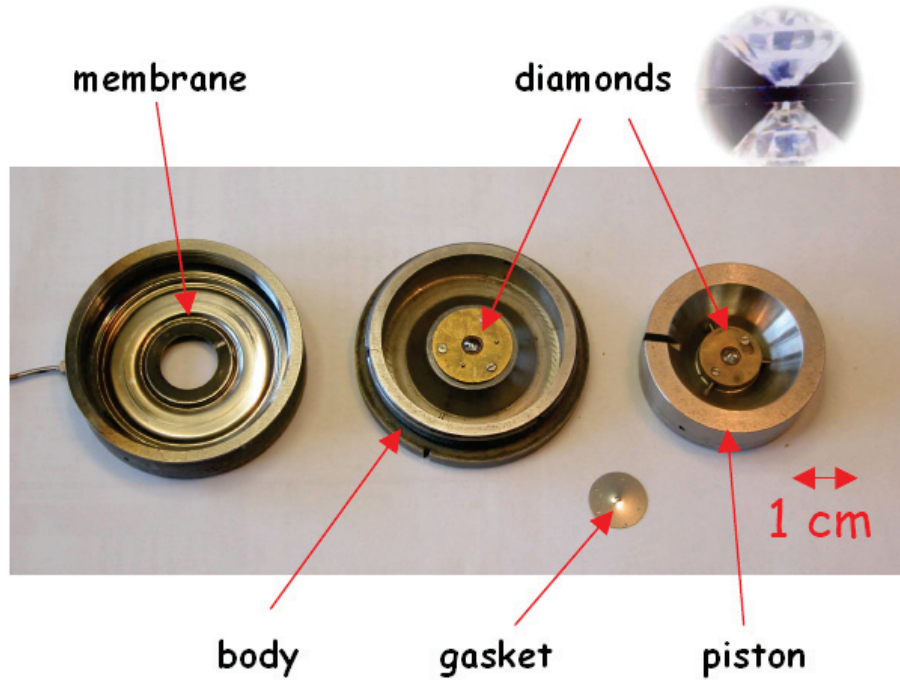


**FIG. 2.8:** Picture of a gas driven Diamond Anvil Cell. Its parts, from left to right: membrane, body, piston and the gasket. On the run, a gas pressurizing system inflates the membrane, which pushes the piston against the body and compress the gasket between them. The sample is installed on the small hole pierced in the gasket center and remains sealed by the anvils and the gasket. In this model, body and piston have a window in their bottom faces, thus the excitation source can reach the sample by passing through one of the diamonds.

blowing nitrogen over a droplet until significant volume reduction. By vaporizing water, the solution aspect became darker, indicating an increased concentration of SWNTs, which improves the signal intensity meaningfully by the increased optical density. Also, vaporizing water increases the DOC concentration and prevents formation of bundles (re-bundling). Sample was then poured into the gasket hole through a glass pipette, covering the entire indentation mark. Afterwards, the DAC was quickly closed and a small starting pressure was applied to avoid air drying or leaks.

For all experiments, the solution worked itself as PTM. At room temperature, water is known to freeze at about 1 GPa. Therefore, for these DOC:SWNT:D<sub>2</sub>O solutions, some facts evidenced the changing from hydrostatic to non-hydrostatic conditions beyond. 1) At about 2 GPa, the ruby fluorescence line instantly red-shifted  $\sim 2\text{cm}^{-1}\text{GPa}^{-1}$ , resuming the usual blue-shift response upon increased pressure. 2) This first fact was accompanied to an image changing of the scattered laser beam. 3) Above a threshold in between 1-2 GPa, the G-band pressure derivative (discussed in next chapter) unusually increased. 4) The G-band broadening ratio increased substantially from 2 GPa. The first fact would happen only upon

a drop in pressure, which is expected immediately after water freezes as its volume expands. The second would require a phase transition. The third indicates an unusual fastened ratio of C-C bond hardening, also linked to the fourth <sup>1</sup>. Moreover, all four facts were observed for all experiments performed with this same PTM, thus excluding any particular sample effect and let as conclusion that hydrostatic regime lasts up to around 2 GPa.

Some details on high-pressure usage must be addressed. Pressure does not reach a stable value instantly after changing the force applied over the diamonds. Plastic deformation of the gasket and PTM (after solidification) leads to a delay for the system stabilizes. Thus, a time interval is desirable before each new sample measurement to avoid large pressure fluctuations during data acquisition. Then, ruby spectra measured before and after each data acquisitions can be averaged to give an usable value, with the difference giving an error bar. As the peaks of the halogen lamp light spectra do not shift with pressure, their frequency shift are due to the loss of calibration of the spectrometer. Thus, halogen lamp was used as a calibrating tool.

All Raman spectra were acquired in backscattering geometry as shown in fig. 2.7. Each experiment was performed following the same basic protocol: 1) Pressure was increased. 2) A 10 minutes delay was taken before next data acquisition. 3) Ruby (for pressure measurement), data (at RBM and G-band regions), halogen lamp (for calibration checking) <sup>2</sup> and ruby again were measured (to account for pressure variations). 4) Pressure was increased and so on until the maximum pressure. Then, release of pressure was carried out similarly.

Whenever required, first treatment consisted of calibrating the acquired data. For this, the Raman Shift (X axis) of each spectrum was shifted by the displacement observed for the peaks of a halogen lamp spectrum measured at the same pressure. This procedure corrects the data by the calibration of the spectrometer. Additionally, each data file was divided a by the respective halogen lamp spectrum file, i.e., both files having the same X axis, Y values were divided, thus weighting all the acquired spectra by the sensitivity of the CCD detector.

---

<sup>1</sup>G-band is discussed in Chapter 4.

<sup>2</sup>This verification was done at each increase of pressure whenever used the high-resolution setup.

## CHAPTER III

## PRESSURE EFFECTS ON THE RADIAL BREATHING MODES

This chapter presents the high-pressure results on RBM resonances. First section describes the experiments and data analysis of the mixed sample, having both empty and water-filled SWNTs. Second section does alike for the two HiPco derived samples, which have mostly empty or mainly water-filled SWNTs, as does the third section for the two Arc discharge derived samples. Fourth section summarizes the data analysis and the fifth discuss the whole dataset. For easiness of comparison, all Raman spectra shown in this chapter are normalized and re-scaled in between 0 and 1 as minimum and maximum intensities. All applied fittings for Raman peaks were done with Lorentzian functions. For compactness, RBM frequency, RBM line width, nanotube diameter and chiral angle are abbreviated as  $\omega_{RBM}$ ,  $\Gamma_{RBM}$ ,  $d_t$  and  $\theta_{Ch}$ , respectively.

## III.1 MIXED EMPTY AND WATER-FILLED SAMPLE

Raman spectra of HiPcoM sample were acquired at different pressures with 568.5 nm wavelength. They are shown in fig. 3.1. At this excitation energy, (6,5), (6,4) and (7,2) chiralities are resonant. The full pressure cycle reached a maximum of 14.6 GPa, with only G-band being measured above 11.5 GPa since RBMs were no further observable. Then, pressure was released, with a few spectra acquired down to 6.8, 5.2, 3.2 and 0.1 GPa.

In order to study the response of RBMs to pressure, peak fitting procedure was carried. According the sample characterization, two peaks were placed to account for empty and water-filled SWNTs of a same chirality. The spectra with their respective Lorentzian fittings are shown in fig. 3.2a. New RBM resonances appeared with the increasing pressure. They correspond to the grey colored peaks in fig. 3.2a, which arise  $\sim 300cm^{-1}$  at 1.5 GPa and  $\sim 350cm^{-1}$  at 3.2 GPa. To keep a smooth evolution of  $\Gamma_{RBM}$  and thus the correct fitting for the identified peaks of (6,5), (6,4) and (7,2) chiralities, these arising peaks were also fitted. For pressures above 3.6 GPa, the  $\omega_{RBM}$  of empty and water-filled nanotubes overlap within their error bars, therefore being impossible to properly fit distinct peaks<sup>1</sup>.

The obtained  $\omega_{RBM}$  and  $\Gamma_{RBM}$  are plotted as functions of pressure in figures 3.2 b and d, respectively. Figure 3.2b shows that  $\omega_{RBM}$  of (6,5), (6,4) and (7,2) SWNTs does not respond linearly to pressure, independently of empty or water-filled states. Then, second order polynomial function was proposed to adjust the  $\omega_{RBM}$  response to pressure, namely:

<sup>1</sup>Similar experiments were carried out for HiPcoM', whose results on RBMs just reproduce HiPcoM.

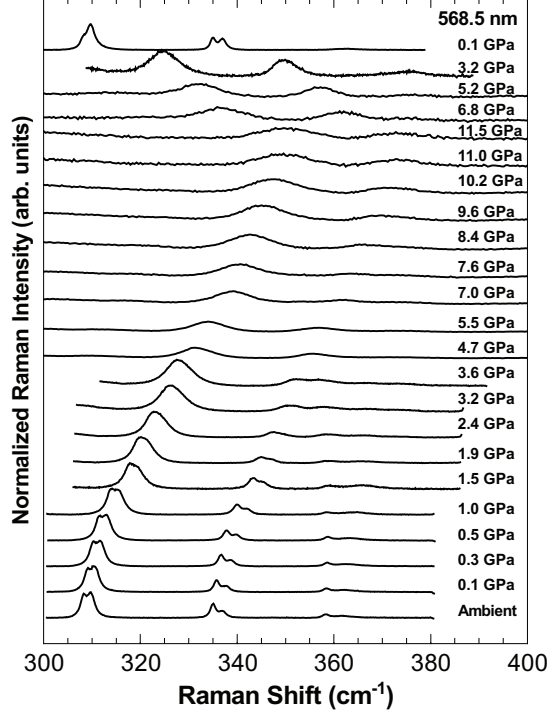


**FIG. 3.1:** RBM spectra of HiPcoM sample at different pressures. Excitation wavelength was 568.5 nm. Pressure values and chiralities are labeled.

$$\omega_{RBM} = \omega_0 + \alpha P + \beta P^2 \quad (\text{III.1.1})$$

Solid lines in fig. 3.2b are fittings given by the equation above, whose first  $\alpha = \partial\omega_{RBM}/\partial P$  and second order  $\beta = \partial^2\omega_{RBM}/\partial P^2$  pressure derivatives are listed in table I.

### III.2 EMPTY AND WATER-FILLED HIPCO SAMPLES

In the case of HiPcoM sample, RBMs were measured at somewhat high pressure. However, resonances from empty and water-filling were indistinguishable above 3.6 GPa, entangling natural evolution and influence of filling. This limitation motivated the study of samples having either mostly empty or mainly water-filled SWNTs, for which HiPcoE and HiPcoF samples were selected. Their collected Raman spectra at different pressures are shown in figures 3.3 a and b, respectively. Both samples were excited with 647.1 nm wavelength, providing resonance to (10,3), (7,6), (7,5) and (8,3) semiconducting, plus (14,2), (13,4), (12,6), (16,1) and (13,7) metallic SWNTs. The pressure cycles reached maximum pressures of 12.8 and 14 GPa for HiPcoF and HiPco samples, respectively.

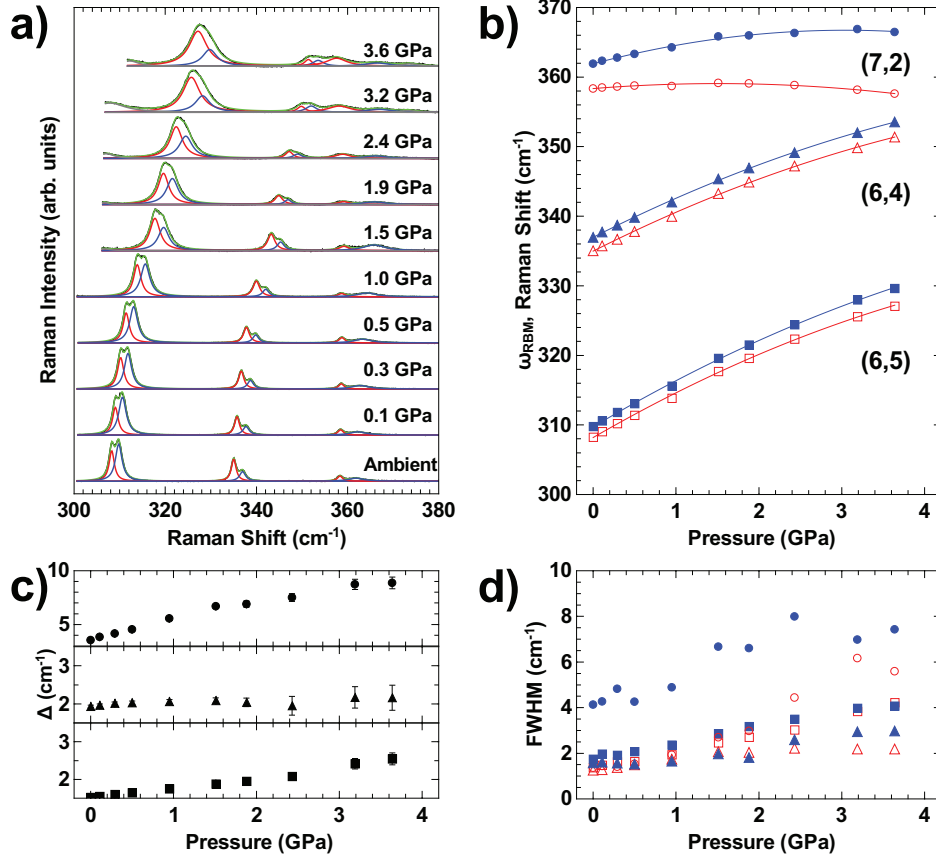


**FIG. 3.2:** (a) Peak fitting of RBM spectra of the HiPcoM sample. Black dots are data points. Red and blue colored peaks are Lorentzian functions which fit the RBMs of empty and water-filled SWNTs, respectively. Grey colored peaks account for RBMs which came into resonance during the pressure run. Green curve shows the fitting line shape. (b) RBM Raman shift ( $\omega_{\text{RBM}}$ ) as a function of pressure, as obtained from the fittings shown in the left panel. The (6,5), (6,4) and (7,2) chiralities are represented by squares, triangles and circles, respectively. Hollow and solid symbols correspond to the  $\omega_{\text{RBM}}$  of empty and water-filled SWNTs, respectively. Red and blue colored lines are second order polynomial functions. (c) Splitting of  $\omega_{\text{RBM}}$  for empty and water-filled configurations with the increasing pressure. (d) Pressure evolution of  $\Gamma_{\text{RBM}}$ , shown with the same encoding.

As shown in last chapter, HiPcoF has a small amount of (7,5) and (8,3) empty nanotubes, though small enough to assume it as being fully composed by water-filled SWNTs. By doing so, each RBM resonance of HiPcoF could be fitted by a single Lorentzian. Conversely, the amount of (7,5) and (8,3) water-filled nanotubes present in HiPcoE sample cannot be neglected. Then, these two chiralities were fitted by two peaks in order to obtain the correct frequencies of empty and water-filled nanotubes.

Since HiPcoE and HiPcoF were studied in separated high-pressure experiments, their spectra were collected at the different pressures, hence peak fitting could not be done simultaneously as at ambient pressure. Thus, the spectra of HiPcoF sample were analyzed first.

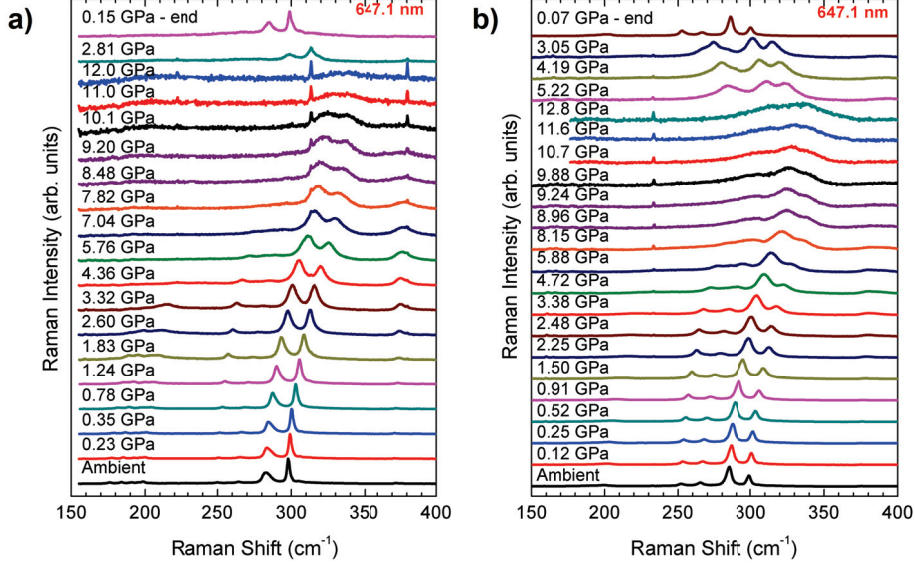


**FIG. 3.3:** RBM spectra of HiPcoE (a) and HiPcoF (b) samples at different pressures. Excitation wavelength was 647.1 nm. Pressure values are labeled.

As each RBM resonance shown in fig. 3.3b was fitted by a single peak, the evolutions of water-filled SWNTs were determined accurately. After, fittings were tried for the HiPcoE data shown in fig. 3.3a, for which the (7,5) and (8,3) chiralities were fitted by a pair of peaks. Then, the so obtained  $\omega_{RBM}$  values of water-filled nanotubes in HiPcoE were projected on the curve obtained from HiPcoF, whereby new values were extrapolated. Then, a second fitting procedure was applied to HiPcoE, but this time, setting  $\omega_{RBM}$  values of water-filled nanotubes according the new ones given by comparing HiPcoF. By doing this, the RBMs of empty nanotubes in HiPcoE sample could be corrected. For those chiralities having only empty nanotubes in HiPcoE sample, RBMs were fitted by a single peak as well.

Fittings were performed while observing the evolution of  $\Gamma_{RBM}$  and chiralities were assigned for the highest pressure values whenever their individual RBMs were distinguishable. The obtained values of  $\omega_{RBM}$  and  $\Gamma_{RBM}$  of both HiPcoE and HiPcoF were then plotted as functions of pressure. The results are shown in figures 3.4 a-e. Figure 3.4a shows a non linear response to pressure for (10,3), (7,6), (7,5) and (8,3) chiralities. Thus, second order polynomial fittings were applied as shown the solid lines in the graph. Figures 3.4 b and c show the evolution of the remaining chiralities, which were assignable uniquely below 2 GPa as their RBMs were lost or became inseparable from others. Because of fitting them with second order polynomials barely gives null  $\beta$  values, linear fittings were applied instead. For all these SWNTs, first and second order (if applicable) pressure derivatives are listed in table I.

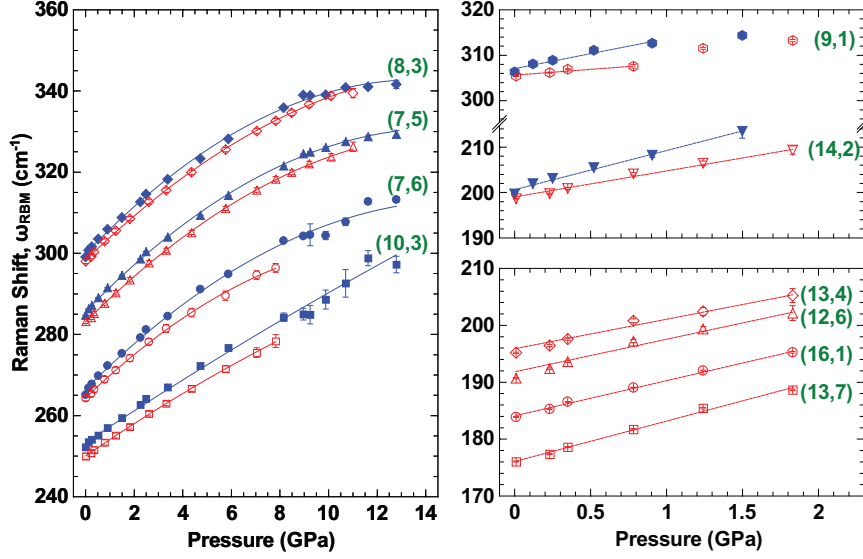


**FIG. 3.4:** Raman shift ( $\omega_{RBM}$ ) as a function of pressure of HiPcoF and HiPcoE samples. Hollow and solid symbols indicate  $\omega_{RBM}$  values of empty and water-filled nanotubes, respectively. Chiralities  $(n,m)$  are labeled. Solid and dashed lines represent second and first order degree polynomial curve fitting, respectively.

### III.3 EMPTY AND WATER-FILLED ARC SAMPLES

Samples derived from Arc discharge SWNTs were selected as they provide different chiralities and narrow distribution of diameters<sup>2</sup>. Then, samples having either mostly empty (ArcE) or water-filled (ArcF) SWNTs were studied under pressure. Their measured spectra are shown in figures 3.5 a and b, respectively. The used 514.5 excitation wavelength provided resonance conditions to semiconducting (15,2), (14,4), (13,6), (12,8) and (11,10) SWNTs in both samples.

Peak fitting procedure was carried after proper background subtraction<sup>3</sup>. Due to line width broadening, the RBMs initially assigned could be individually studied under pressure uniquely while empty, e.g., in ArcE sample, up to 1 GPa only.<sup>4</sup> Then, so obtained parameters  $\omega_{RBM}$  and  $\Gamma_{RBM}$  were plotted as functions of pressure, as show in figures 3.6 b and c, respectively. Within this low pressure range, the RBM response were found linear, represented by the solid lines in fig. 3.6 b. The respective pressure derivatives are summarized in table I.

<sup>2</sup>This advantage will be clear next chapter.

<sup>3</sup>For a complete description on the background treatment applied to these Arc derived samples, see annex.

<sup>4</sup>In ArcF, an attempt to perform fittings by setting up manually the  $\Gamma_{RBM}$  evolution gave inconsistent results which depended on the fitting itself.

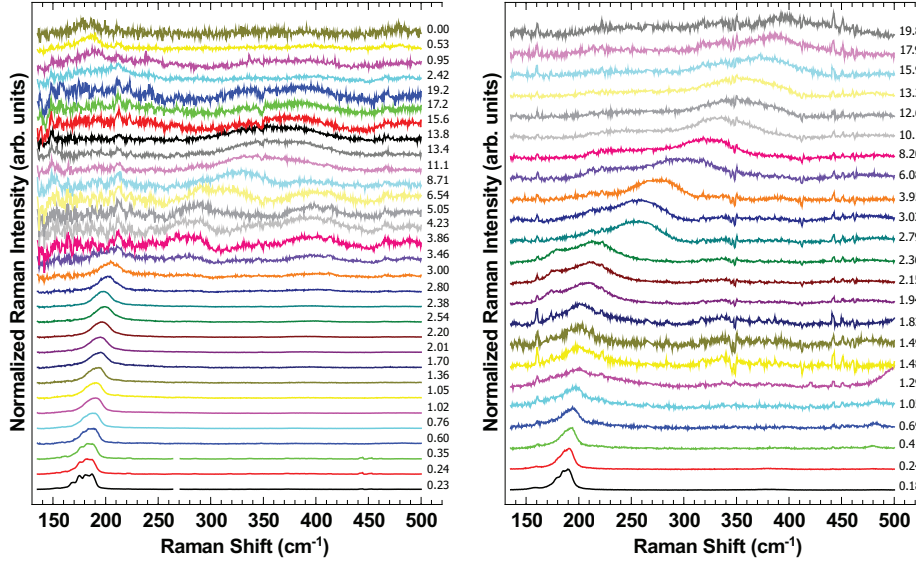


**FIG. 3.5:** Background subtracted, normalized RBM spectra of ArcE (a) and ArcF (b) samples at different pressures. Excitation wavelength was 514.5 nm. Pressure values are labeled.

### III.4 PRESSURE DERIVATIVES

After their evaluation from the graphs shown in figures 3.2a, 3.4 a-c and 3.6a, the first ( $\alpha_{RBM}$ ) and second ( $\beta_{RBM}$ ) order pressure derivatives of  $\omega_{RBM}$  are summarized in table I. All the studied SWNTs are shown with their respective geometrical parameters for reference. Weighting of error bars were accounted during evaluations. For the sake of comparison,  $\alpha_{RBM}$  and  $\beta_{RBM}$  are plotted as functions of diameter and chiral angle in fig. 3.7.

### III.5 DISCUSSION ON THE RADIAL BREATHING MODES

Qualitative changes can be immediately noticed by comparing the diverse Raman spectra. Figures 3.1, 3.3 and 3.5 show the entire pressure cycles of HiPcoM, HiPcoE/F and ArcE/F samples, respectively. Regarding all of them, the RBM resonances progressively shift to higher frequencies, broaden and lose intensity as the pressure increases<sup>5</sup>.

Observing the RBM features in fig. 3.3, empty and water-filled nanotubes are inseparable above 3.6 GPa. From 4.7 to 11.5 GPa, bands of at least (6,5) and (6,4) are observable, with (6,4) progressively gaining intensity in respect to (6,5). Upon releasing pressure, RBMs

<sup>5</sup>Remark that signal to noise ratio decreases with the increasing pressure, which indicates loss of intensity despite that normalization of spectra set all the maximum intensities to a same value. In HiPcoE and HiPcoF, drastic loss of intensity is noticed also by comparing the intensities between RBM features and some spikes. Additionally, acquisition times increased substantially, from a few minutes at the lower pressures up to one hour to barely measure some spectra at the highest pressures.

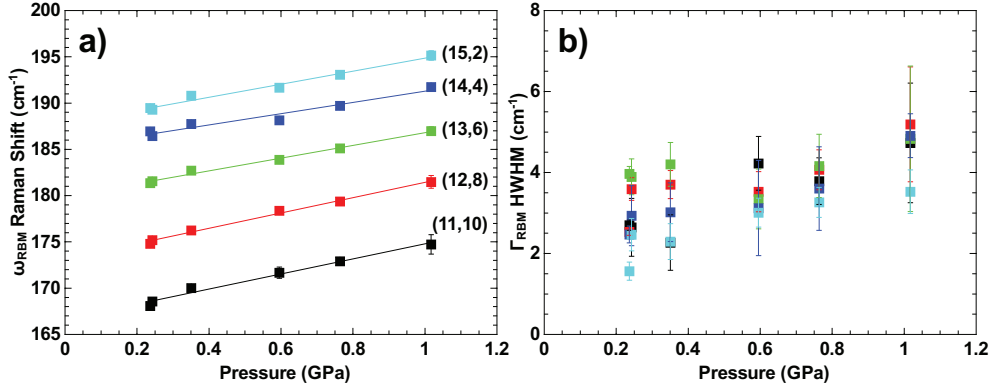


**FIG. 3.6:** (a) Plot of  $\omega_{RBM}$  as a function of pressure of ArcE sample. Chiralities  $(n,m)$  are labeled. Solid lines represent linear fittings. (b) The respective pressure evolution of  $\Gamma_{RBM}$ . Symbols and color code match in both panels.

were progressively recovered, having their intensities increasing as the pressure was released. Although, RBMs of empty and water-filled nanotubes remained indistinguishable until full release of pressure.

Permanent pressure induced modifications can be verified by comparing the spectra collected before and after the experiment, e.g., before any increase and after full release of pressure. In this sense, initial and final RBM profiles of (6,5), (6,4) and (7,2) are compared in fig. 3.9a. The relative intensities of empty and water-filled RBMs for each  $(n,m)$  have changed. Considering (6,5) and (6,4), peaks of water-filled nanotubes became much stronger than those of empty ones, indicating an increased amount of filled nanotubes after the high pressure cycle. Nonetheless, for the (7,2), instead of two, a single Raman band was recovered after the pressure cycle. This band  $\omega_{RBM}$  and  $\Gamma_{RBM}$  matches the water-filled (7,2) original values, proving that empty (7,2) nanotubes disappeared from the spectrum.

Figure 3.8 shows the integrated intensities of RBMs of (6,5), (6,4) and (7,2) before and after the pressure cycle. To draw this graph, intensity was calculated for each RBM feature accounting both peaks of empty and water-filled SWNTs. Since absolute intensities cannot be compared, the values were normalized by the most intense peak of (6,5). By this figure, one verifies that after releasing the pressure, even though the lasting (7,2) feature finished totally water-filled, it became weaker in respect to (6,5) and (6,4) while comparing initial and final values. Thus, not only empty but also water-filled (7,2) nanotubes were damaged.

Analyzing the evolution of RBMs of water-filled (10,3), (7,6), (7,5) and (8,3) SWNTs in fig. 3.3b, the RBMs of (10,3) and (7,6) gain intensity in respect to the initially stronger (7,5) and (8,3). This can suggest a change of resonance conditions, favorable to (10,3) and (7,6). Further, RBMs of all four chiralities are still resonant at 12.8 GPa, while water-filled. During release of pressure, down to 5.2, 4.2 and 3.1 GPa, the RBMs have recovered intensity, yet,

**TABLE I:** First  $\alpha$  and second  $\beta$  pressure derivatives of all studied SWNTs.

| (n,m)   | $d_t(nm)$ | $\theta_{Ch}()$ | E/F | $\omega_0(cm^{-1})$ | $\alpha(cm^{-1}GPa^{-1})$ | $\beta(cm^{-1}GPa^{-2})$ |
|---------|-----------|-----------------|-----|---------------------|---------------------------|--------------------------|
| (7,2)   | 0.64      | 12.2            | E   | 359.7               | $0.96\pm 0.10$            | $-0.31\pm 0.03$          |
|         |           |                 | F   | 362.9               | $3.15\pm 0.17$            | $-0.51\pm 0.05$          |
| (6,4)   | 0.68      | 23.4            | E   | 335.5               | $6.00\pm 0.11$            | $-0.41\pm 0.04$          |
|         |           |                 | F   | 337.4               | $6.02\pm 0.12$            | $-0.40\pm 0.04$          |
| (6,5)   | 0.75      | 27              | E   | 308.6               | $6.89\pm 0.19$            | $-0.46\pm 0.05$          |
|         |           |                 | F   | 310                 | $7.06\pm 0.19$            | $-0.42\pm 0.05$          |
| (9,1)   | 0.75      | 5.2             | E   | 304                 | $3.55\pm 0.42$            |                          |
|         |           |                 | F   | 305.6               | $6.58\pm 0.80$            |                          |
| (8,3)   | 0.77      | 15.3            | E   | 297.1               | $5.80\pm 0.09$            | $-0.17\pm 0.02$          |
|         |           |                 | F   | 298.9               | $6.25\pm 0.16$            | $-0.22\pm 0.01$          |
| (7,5)   | 0.82      | 24.5            | E   | 282.6               | $5.96\pm 0.06$            | $-0.19\pm 0.01$          |
|         |           |                 | F   | 284.4               | $6.17\pm 0.12$            | $-0.21\pm 0.01$          |
| (7,6)   | 0.88      | 27.5            | E   | 263.6               | $5.77\pm 0.16$            | $-0.21\pm 0.02$          |
|         |           |                 | F   | 265.1               | $5.98\pm 0.29$            | $-0.19\pm 0.03$          |
| (10,3)  | 0.92      | 12.7            | E   | 251.8               | $3.97\pm 0.35$            | $-0.03\pm 0.03$          |
|         |           |                 | F   | 252.7               | $4.12\pm 0.35$            | $-0.07\pm 0.01$          |
| (14,2)  | 1.18      | 6.6             | E   | 198.6               | $5.71\pm 0.28$            |                          |
|         |           |                 | F   | 199.4               | $6.62\pm 0.28$            |                          |
| (13,4)  | 1.21      | 13              | E   | 195.3               | $5.17\pm 0.32$            |                          |
| (12,6)  | 1.24      | 19.1            | E   | 190.8               | $5.72\pm 0.40$            |                          |
| (15,2)  | 1.26      | 6.2             | E   | 188.7               | $7.05\pm 0.49$            |                          |
| (14,4)  | 1.28      | 12.2            | E   | 185.3               | $6.08\pm 0.68$            |                          |
| (16,1)  | 1.29      | 3               | E   | 183.8               | $6.18\pm 0.17$            |                          |
| (13,6)  | 1.32      | 18              | E   | 180.9               | $6.87\pm 0.31$            |                          |
| (12,8)  | 1.37      | 23.41           | E   | 174.9               | $8.27\pm 0.34$            |                          |
| (13,7)  | 1.38      | 20.2            | E   | 175.9               | $7.10\pm 0.27$            |                          |
| (11,10) | 1.42      | 28.4            | E   | 168.7               | $8.14\pm 0.53$            |                          |

with RBMs of (10,3) and (7,6) reappearing as strong as the ones of (7,5) and (8,3), showing that they recovered their RBMs much easier. During release of pressure, the recovered RBMs show widths much larger than that observed at equivalent pressures but during the run up, which can be checked by comparing them to those RBMs measured at 5.9, 4.7 and 3.4 GPa. This difference of width can be explained. (i) By an hysteresis like response. After a pressure induced ovalization, these SWNTs would regain the circular shaped cross section only after full or substantial release of pressure <sup>6</sup>. (ii) By a plastic like response of the environment itself. Even fully releasing the pressure over the entire SWNT:DOC:D<sub>2</sub>O

<sup>6</sup>It must be remarked that even after nulling the force applied over the diamond anvils, the solution remained solidified. As the PTM plasticized, pressure was found  $\sim 3$  GPa, even without external force. Ambient pressure was reached only after quickly but gently opening and closing of the DAC, prompting liquefaction of the PTM and thus lowering the pressure from  $\sim 3$  GPa to zero.

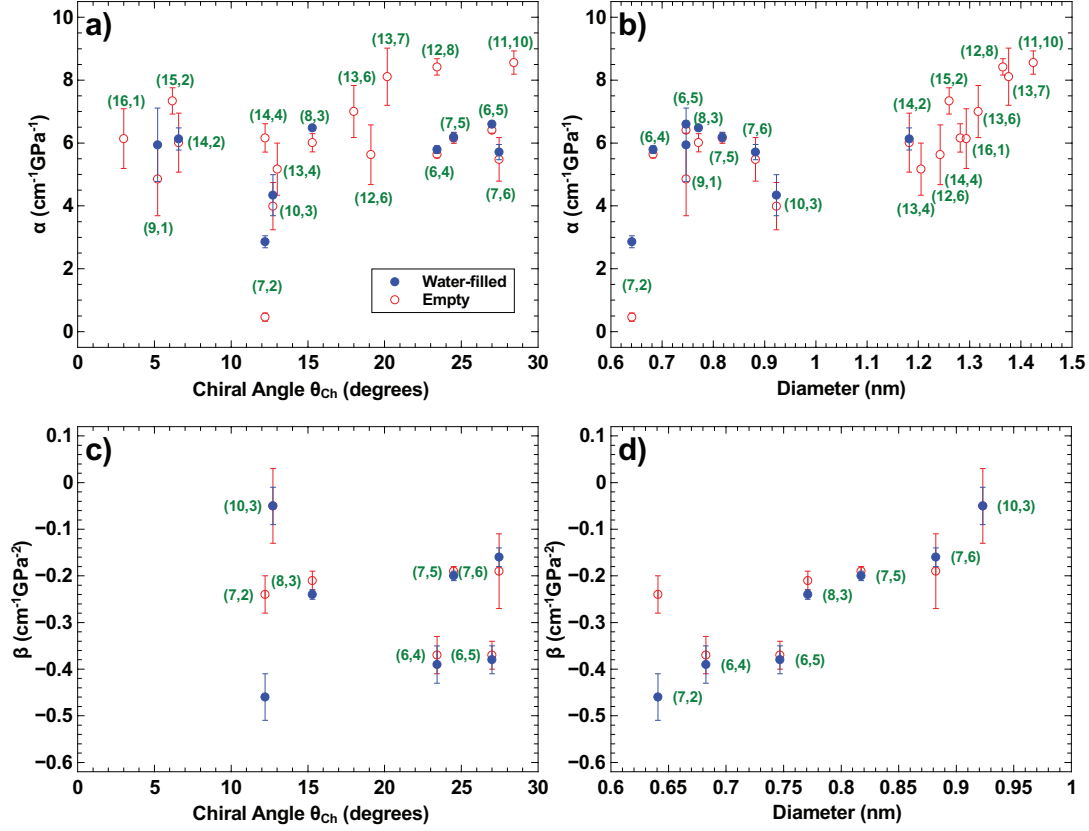


**FIG. 3.7:** First ( $\alpha = \partial\omega_{\text{RBM}}/\partial P$ ) and second ( $\beta = \partial^2\omega_{\text{RBM}}/\partial P^2$ ) order pressure derivatives described as functions of chiral angle (a and c) and diameter (b and d). Hollow and solid symbols indicate empty and water-filled nanotubes, respectively, alike red and blue colors. Labels name the chiralities.

system, the plasticized solid would keep the nanotubes and DOC molecules pressurized. The HiPcoF sample also provide thicker, metallic nanotubes, as show the asymmetric band like feature ( $\sim 160\text{-}220\text{ cm}^{-1}$  at ambient pressure) in which only the (14,2) is resolved. Anyhow, analyzing the whole feature, the RBMs of these thicker water-filled SWNTs are still in resonance at 8.2 GPa.

Figure 3.3a show the evolution of RBMs of mostly empty (10,3), (7,6), (7,5) and (8,3). Contrarily to the water-filled situation, the RBM signals of empty (10,3) and (7,6) remain weak during the run up, even being indistinguishable or vanished above 7.8 GPa. Also, the (7,5) feature becomes dominant at 4.4 GPa. Further, all four lose their RBMs in between 11.0 to 12.0 GPa. Moreover, the RBMs of empty, metallic, thicker (13,7), (16,1), (12,6), (13,4) and (14,2) were individually resolved up to 1.83 GPa, having their intensities zeroed in between 3.3 to 4.4 GPa.

For insight on the permanent pressure induced changes, the RBM spectra of HiPcoE

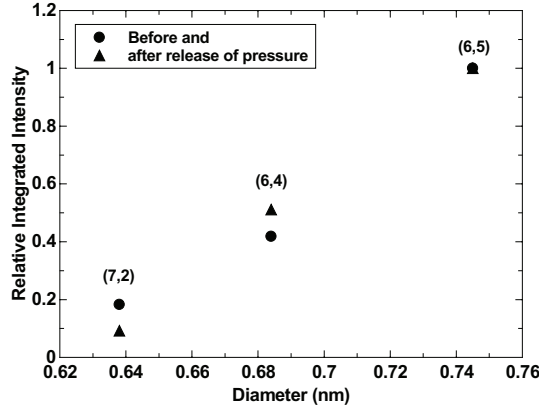


**FIG. 3.8:** Integrated intensity of RBMs before (circles) and after (triangles) the pressure cycle. Each point the graph was calculated accounting both empty and water-filled nanotubes of a same chirality. The values are normalized by the most intense peak of the (6,5) SWNT.

and HiPcoF samples measured before and after the high-pressure cycle are compared in fig. 3.9b. For the water-filled (10,3), (7,6), (7,5) and (8,3), the major changes are the swap of intensities between (8,3) and (7,6), and the slight loss of intensity of (8,3) in respect to (7,5). For the empty ones, all four were shifted to higher frequencies, enough to consider that they became damaged by pressure, thus opened and filled with water. Concerning the thicker nanotubes, which spectra are zoomed in the insets, no RBMs of empty nanotubes were recovered whilst the RBMs of water-filled reappeared.

The comparisons in fig. 3.9 give an information concerning all HiPco samples. The recovered RBMs are individually resolved, which excludes any possibility of re-bundling of SWNTs during the experiments, ruling out inter-tube interactions.

From the Arc samples, the evolution of RBMs of empty and water-filled (15,2), (14,4), (13,6), (12,8) and (11,10) is compared in fig. 3.10. Empty and water-filled configurations are represented by red and blue colors, respectively. Albeit the RBMs of water-filled ones cannot be fitted individually, the shift of whole features of empty and filled can be compared. Thus, alike the other studied SWNTs, the water-filled ones shift faster with pressure. By comparing the intensities, the empty nanotubes lose the RBMs in between 3.5 and 3.9 GPa, whilst the water-filled ones keep their RBMs under higher pressures.

Comparing the panels of fig. 3.10, whilst the RBM signal of ArcE sample shows only the common trend of blue-shift and broadening with the increasing pressure, the ArcF sample shows two new features arising at 1.9 and 2.8 GPa, labeled in the graph by an asterisk and an arrow, respectively. It is known that pressure shifts the resonance energies by changing the van Hove singularities<sup>42,136</sup>. Thus, given a fixed excitation wavelength, nanotubes can enter or leave resonance conditions with pressure. However, considering the diameter range

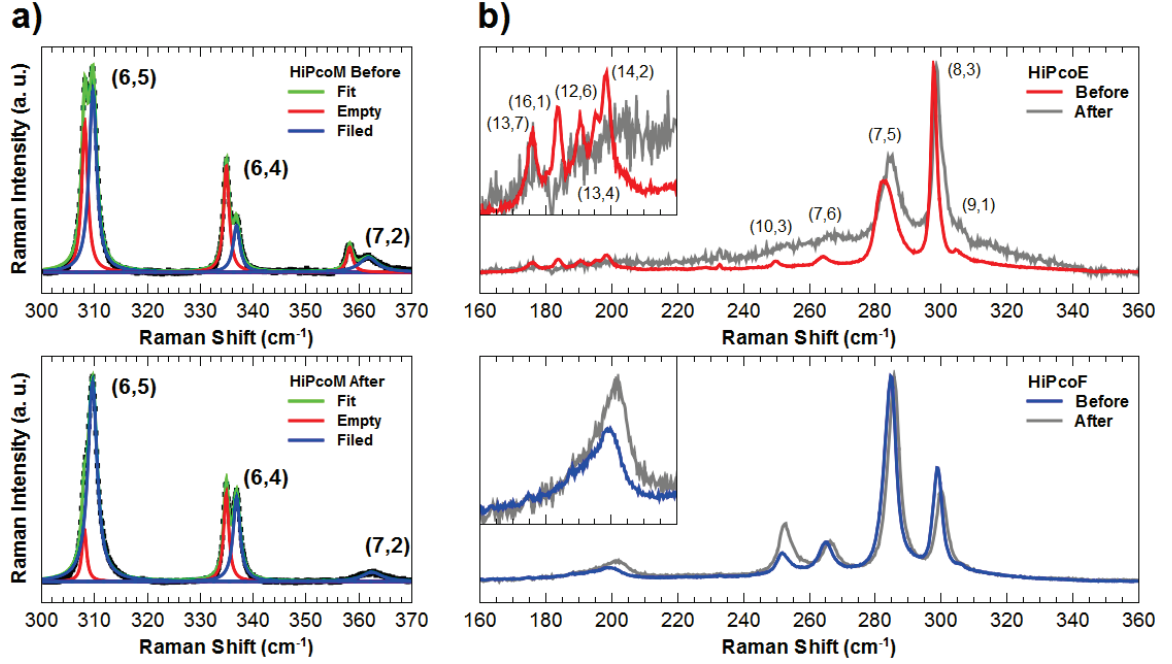


**FIG. 3.9:** Comparison of spectra measured at beginning and ending of the pressure cycles, respectively shown in upper and lower panels. Chiralities are conveniently labeled. (a) HiPcoM sample. Data, line shape fitting, RBMs of empty and water-filled nanotubes are shown in black, green, red and blue colors, respectively. (b) HiPcoE and HiPcoF samples. Spectra measured at the beginning of pressure cycles are shown in red (HiPcoE) and blue (HiPcoF) colors. Spectra measured after are shown in grey color for both samples. The RBM of metallic SWNTs are zoomed in the insets.

of SWNTs synthesized by Arc discharge, a suggested energy shift of 20 meV/GPa would put into resonance only nanotubes having similar diameters to those of (15,2), (14,4), (13,6), (12,8) and (11,10). By consulting the Kataura plot, the lower frequency new feature could be attributed to a SWNT being resonant at 1.9 GPa. The highest frequency new feature at 2.8 GPa however, it cannot be attributed to a RBM for two reasons. As a whole, it shifts excessively faster with pressure for a RBM. Considering the energy shift, there is no diameters matching its frequency. Thus, the new band at 2.8 GPa must have other origin.

It is important to remark that defects may have influence on how resilient a SWNT can be against pressure<sup>56</sup>. Upon opening by ultra sound to obtain water-filling, the SWNTs were invariably damaged. Thereby, the many SWNTs acquired different distribution of defects, which cannot be evaluated in this study<sup>7</sup>. Therefore, it can be suggested that even if water molecules still provide a mechanical support against pressure, the supporting

<sup>7</sup>Evaluation of defects would require an D-band analysis, which is impossible to perform under pressure as D-band and Diamond bands share a very close frequency  $\sim 1350\text{cm}^{-1}$ . Though it is possible to measure D-band before loading and after releasing the pressure, e.g., outside or with the DAC open to avoid the Diamond band, for this sake, it is required to recover or keep the sample in the gasket, which has been proved impossible for SWNT:DOC:D<sub>2</sub>O solution, due to leak or vaporization.

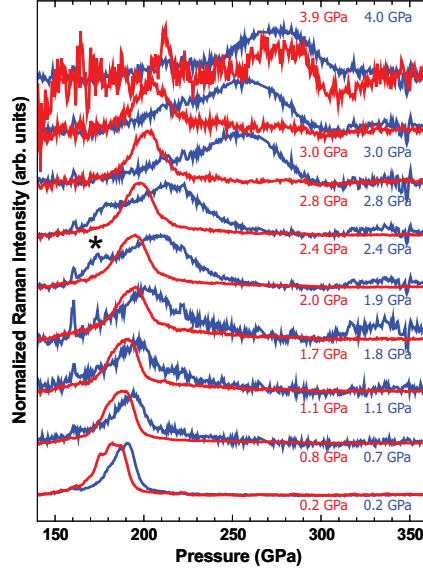


**FIG. 3.10:** Comparison of RBM spectra of ArcE (red color) and ArcF (blue color) samples. Offsets in Y axis are aligned in order to show similar pressures, which respective values are labeled in colors resembling the spectra. The asterisk and arrow symbols mark RBM resonances which arise with pressure at lower and higher frequencies, respectively.

strength could vary with defect distribution, also explaining why some empty (6,5) and (6,4) SWNTs were damaged and became water-filled whilst others remained empty.

The increased filling ratio which was observed after the pressure cycles of HiPcoM and HiPcoE samples can be explained as follows. Invariably, pressure modified the initial circular cross-section, inducing ovalization or even the collapse. Upon release of pressure, two possible outcomes can be suggested. 1) Empty nanotubes became irreversibly collapsed, hence they do not show RBMs in the recovered spectrum. 2) Empty nanotubes regained the circular cross section shape, albeit they were damaged sufficiently to be opened, thus water molecules filled them and consequently their RBMs reappeared shifted to higher-frequencies. Nevertheless, neither of the possibilities solely can explain all the experimental facts. The first statement is negated by the recovered (6,5) and (6,4) empty SWNTs. The second statement does not explain the unrecovered (7,2) empty SWNTs. Though, given the maximum achieved pressures of 12-13 GPa, both statements can assert why the initially empty (10,3), (7,6), (7,5) and (8,3) SWNTs became water-filled.

Pressure derivatives are analyzed as a function of diameter in fig. 3.7a. Concerning the thinner nanotubes, e.g.,  $d_t = 0.68 - 0.88\text{nm}$ , respectively from (6,4), (6,5), (9,1), (8,3). (7,5) and (7,6) SWNTs,  $\alpha_{RBM}$  values were found within  $5 - 7\text{cm}^{-1}\text{GPa}^{-1}$ , agreeing with a previous investigation on surfactant individualized HiPco SWNTs<sup>84</sup>. Conversely for thicker nanotubes, e.g.,  $d_t > 1.1\text{nm}$ , they have shown  $\alpha_{RBM}$  increasing with the diameter, though

having values comparable to some results reported on bundled SWNTs of equivalent diameter distributions<sup>118</sup>.

Figures 3.2b and 3.4a show that  $\omega_{RBM}$  shifts faster if a given nanotube is filled with water. With no exception for the studied chiralities, this fact occurs independently of diameter or chiral angle. To highlight this result, one can observe the splitting between  $\alpha_{RBM}$  values of empty and filled configurations for each given chirality in fig. 3.7a.

Thinking on a simple model to explain this observation, one can assume a SWNT as an hollow, nanometric size but still a bulk like cylinder having slick walls. The internal water molecules interact with the carbon atoms, which is known by the blue-shift of  $\omega_{RBM}$  and broadening of  $\Gamma_{RBM}$  at ambient conditions. Due to the cylindrical geometry, the pressure acts in a radial symmetry, e.g., directly against the RBM vibrational movement. Invariably, the nanotube volume must decrease with the increasing pressure. In the case of empty tubes,  $\omega_{RBM}$  will increase as the diameter diminishes, which is compatible with classic elastic theory (citation). In the case of water-filled tubes however, there is an additional contribution. By forcing the wall against the water molecules inside the nanotube, the filler-wall interaction strengthens. Compressed, the filler molecules would exert a restoring, counter force effect against the external pressure. Thus, this additive contribution provided by the inner content hasten the  $\omega_{RBM}$  shift, increasing  $\alpha_{RBM}$ .

While most of the SWNTs show comparable values of  $\alpha_{RBM}$ , an exception was found for the (7,2) chirality. While empty,  $\omega_{RBM}$  of (7,2) barely blue-shifts at lower pressures if one considers the lower limit of the error bars. Beyond 1.5 GPa, it even red-shifts, which is unique for this chirality. Afresh other SWNTs, filling the (7,2) with water yet augments  $\alpha_{RBM}$ . Albeit the increasing, it remains smaller than that of all other tried SWNTs, either by literature or this work. Even though, the difference between  $\alpha_{RBM}$  of empty and filled states in (7,2) is the largest. This difference of  $\alpha_{RBM}$  values reinforces that water-filling can be a potential mechanical stabilizer for SWNTs.

Classical molecular dynamics shows that compression or tension causes a torsion in chiral (8,2), (8,4) and (8,6) SWNTs, whilst achiral (8,0) and (8,8) are unaffected<sup>146</sup>. This strain-torsion coupling shows a peak for (8,2) chirality, which has chiral angle  $\theta_{Ch} = 10.89$ . Applying this theoretical result to the compression of the (7,2) SWNT, the axial strain caused by pressure induces a torsion component. Thus, by twisting itself, the (7,2) SWNT could damp the  $\omega_{RBM}$  shift, slowing it down in respect to pressure. In addition, theory shows that small diameter SWNTs can be naturally twisted due to a torsion instability<sup>147</sup>. Given the experimental result, this lowering of  $\alpha_{RBM}$  can be stronger or even peaked as the chiral angle approaches 12.2.

To discuss the role of the chiral angle,  $\alpha_{RBM}$  is plotted as function of  $\theta_{Ch}$  in fig. 3.7a.

According to the graph,  $\alpha_{RBM}$  has a minimum given by the (7,2), which has  $\theta_{Ch} = 12.2$  and  $d_t = 0.64nm$ . The next  $\alpha_{RBM}$  closer to the minimum is given by the (10,3), which has  $\theta_{Ch} = 12.7$  and  $d_t = 0.92nm$ . Thus, (7,2) and (10,3) suggest a strong  $\alpha_{RBM}$  dependence on  $\theta_{Ch}$ . Meanwhile, the (14,4), having  $\theta_{Ch} = 12.2$  and  $d_t = 1.28nm$ , it shows  $\alpha_{RBM}$  as high as many other chiralities, regardless of sharing the same chiral angle of the (7,2). Moreover, the (13,4), having  $\theta_{Ch} = 13.0$  and  $d_t = 1.21nm$ , it shows  $\alpha_{RBM}$  with error bars in between (14,4) and (10,3). These observations lead to conclude that  $\alpha_{RBM}$  depends strongly on  $d_t$ , but as this parameter diminishes, specially below nanometric values,  $\alpha_{RBM}$  dependence on  $\theta_{Ch}$  increases meaningfully. Therefore, nanotubes having sub-nanometer diameters would behave differently upon pressure because of their particular geometrical construction, adding torsion instability and self twisting, which are peaked to a chiral angle approaching 12 degrees. Noticeably, the geometrical influence on  $\alpha_{RBM}$  repeats upon filling with water, which enhances the suggestion that  $\alpha_{RBM}$  depends on specific nanotube geometry, e.g., on  $d_t$  and on  $\theta_{Ch}$  as  $d_t$  diminishes.

Other molecular dynamics simulations show that water can assume different arrangements inside a SWNT<sup>13,25,148–150</sup>, which is supported experimentally<sup>10,151</sup>. Upon confinement, theory has been suggesting that bulk water<sup>8</sup> would exist down to diameters of 2.5 nm, it would assume a layered configuration down to 1 nm diameters and for sub-nanometers, water molecules would be queued, organizing a chainlike configuration in which a single molecule occupy a cut of the transversal section at a time<sup>149</sup>. This later arrangement is called single-file water-filling<sup>152,153</sup>. From these calculations<sup>9</sup>, the (10,3) could comport both single or layered filling configurations, suggesting that its 0.92 nm diameter is a threshold for water molecules queuing<sup>150</sup>. Moreover, new phases or phase transitions of water under nano-confinement are also suggested<sup>23,154,155</sup>.

Albeit that no information can be obtained by Raman on the water inside the SWNTs, the splitting of  $\alpha_{RBM}$  values for empty and water-filled can be discussed. To remind, the blue-shift of  $\omega_{RBM}$  due to water-filling does not show a simple trend with either diameter or chiral angle, leading to conclude that it depends on the geometrical arrangement of the water molecules<sup>10</sup>. By observing a repeated lack of trend upon pressure application, it can be suggested that the mechanical support provided by water-filling also depends on the orientation of the water molecules inside the SWNTs.

Figures 3.2 and 3.4 show that  $\omega_{RBM}$  response to pressure is nonlinear. The nonlinearity is observed below 1 GPa, which is lower than the estimated hydrostatic limit of 2 GPa. It even fits within the 1 GPa limit of water itself. Thus, in this case, non linear response cannot

<sup>8</sup>Originally referred as bulk mode water<sup>149</sup>.

<sup>9</sup>For information, single-file water-filling can be described also by Ising model<sup>26</sup>.

be attributed to non hydrostatic compression. Moreover, second degree polynomials well fitted the  $\omega_{RBM}$  behavior. Going to the literature, nonlinear response of RBMs contradicts the majority of the high-pressure experiments performed on SWNTs, which describe the pressure evolution of  $\omega_{RBM}$  by a linear ramping. Nonlinear response was experimentally reported at least once, for bundled, Arc discharge metallic SWNTs ( $d_t = 1.3 \pm 0.2nm$ )<sup>118</sup>. Although, the second order dependence was not discussed.

According to theory,  $\omega_{RBM}$  of individualized (9,9) ( $d_t = 1.22nm$ ) and (10,10) ( $d_t = 1.36nm$ ) SWNTs respond linearly to pressure<sup>112</sup>. Nonetheless, the predicted  $\omega_{RBM} \sim 1.3cm^{-1}GPa^{-1}$  is much smaller than the values observed by several experimental studies, including also the one here, performed for the ArcE sample, which diameters are comparable to those of (9,9) and (10,10). For bundled (9,9) and (10,10) SWNTs,  $\omega_{RBM}$  was predicted to shift following a second degree polynomial and also,  $\Gamma_{RBM}$  was suggested to broaden non homogeneously<sup>112</sup>. The predicted slope of  $9.6cm^{-1}GPa^{-1}$  is large but comparable to the reported values, which led to the suggestions that the slope would be increased due to inter-tube interactions in bundles. Recently,  $\omega_{RBM}$  was found to shift upon pressure at similar slope either in bundled or individualized configurations, contradicting many previous studies<sup>126</sup>.

In carbon materials, nonlinear response to pressure was observed for the G-mode of bundled SWNTs<sup>112,118</sup>, graphene (citation) and graphite<sup>129</sup>. For this last, anharmonic vibrations of the carbon C-C bonds are suggested to explain the nonlinearity. Nevertheless, G-mode and RBM have different origins. Possibly, additional considerations on the molecular nature of SWNTs and the environment must be taken into account. While pressure can be assumed as uniformly distributed over a bulk sample, it would not be the case for an individual SWNT. In surfactant solubilised SWNT samples, inter-tube interactions are zeroed, however, surfactant-tube interaction cannot be quantitatively estimated. Immersed in DOC:D<sub>2</sub>O solution, the SWNTs are wrapped by the DOC molecules, which keep them dispersed. Thus, transmission of pressure from water to the SWNTs is unbeknownst intermediated by the surfactant. In fig. 3.7d, the absolute value of  $\beta_{RBM}$  is inversely proportional to  $d_t$ , indicating that the nonlinear response to pressure is stronger for the smaller diameters. Therefore, application of pressure in molecular scale may work differently than bulk sized materials.

The Gruneisen parameter  $\gamma$  is defined after the normalized (or logarithmic) pressure derivative  $\Omega$  and compressibility  $C$  modulus (see equation I.3.4). Hence, an analysis on  $\Omega_{RBM}$  can give insight on how the compressibility of a SWNT depends on their intrinsic parameters, diameter and chirality. Given all SWNTs studied in this work, their  $\Omega_{RBM}$  were calculated with the values listed in table I and plotted as a function of  $\omega_{RBM}$  in fig.

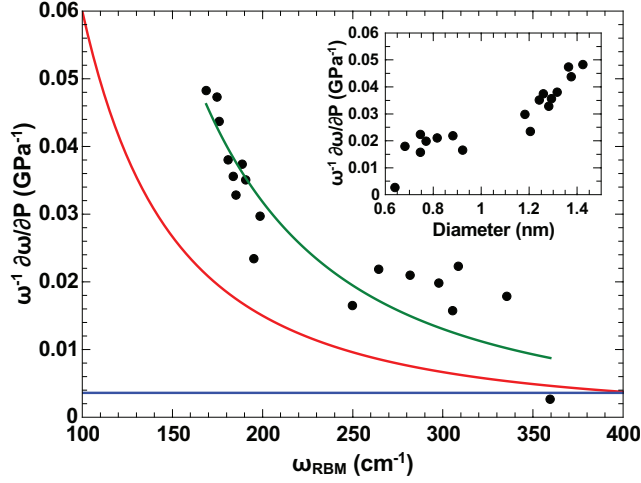


**FIG. 3.11:** Normalized pressure derivatives of RBM ( $\Omega_{RBM}$ ) as a function of RBM frequency ( $\omega_{RBM}$ ). Red colored line is a  $y = 600/x^2$  function put as a guide to the eye. Blue line indicates the theoretical prediction of  $0.0036 \text{ GPa}^{-1}$  to isolated SWNTs<sup>104</sup>. Green line is a  $\Omega_{RBM} = 3672\omega_{RBM}^{-2.2}$  function fitted to the data after a  $y = Ax^{-2.2}$  dependence suggested in literature<sup>156</sup>. The inset shows  $\Omega_{RBM}$  as a function of  $d_t$ .

3.11. As a complement, the inset includes an equivalent plot on  $d_t$ .

In literature,  $\Omega_{RBM}$  is suggested to depend on  $\omega^{-2}$  or  $\omega^{-2.2}$ <sup>104,156</sup>. Fitting the experimental data in 3.11a by the second model, e.g., writing  $\Omega = A\omega_{RBM}^{-2.2}$ , the result is the green colored curve in the graph, with the fitted constant  $A = 3672$ . Two trends are clearly distinguishable in the graph. For the SWNTs having diameters larger than 1 nm,  $\Omega_{RBM}$  decreases with  $\omega_{RBM}$ , or equivalently it increases with  $d_t$ . These thicker SWNTs follows closely the fitted green curve, resembling the data points which gave the suggested dependence<sup>104,156</sup>. However, regarding the SWNTs having sub-nanometric diameters,  $\omega_{RBM}$  diverges from the  $\omega^{-2.2}$  model. Therefore, the suggested dependence does not explains the response to pressure of RBMs of SWNTs having sub-nanometric diameters. Also important, the SWNTs having  $\theta_{Ch}$  approaching 12 degrees show the largest deviations from the fitted curve.

## CHAPTER IV

## PRESSURE EFFECTS ON THE TANGENTIAL MODES

This chapter presents the high-pressure effects on the G-band. First section shows the data and respective peak fitting analysis of all samples. Second section discuss the results altogether. All the Raman spectra shown are normalized and re-scaled without baseline subtraction. All fittings applied to the G-band were carried with Voigt profiles. For simplicity, the abbreviations repeat from last chapter, including the new  $\omega_{G_i}$  and  $\Gamma_{G_i}$  for G-band frequency and line width, respectively, with index  $i = +, -$  standing for the highest (G+) and the lowest (G-) frequency profiles of the G-band.

## IV.1 DATA ANALYSIS

Figure 4.1a shows selected G-band spectra of HiPcoM' sample measured under pressure. By comparing the diverse spectra shown in the graph, one verifies that the line shape of the G- feature are very different. For instance, from 0.5 to 1.3 GPa, G- changes from a broad band shape to a set of more distinguishable peaks, which are also more blue shifted and closer to G+. Therefore, it is impossible to fit G- in these data by setting a same amount of peaks to comprise for a considerable pressure range. Thus, the G-band spectra were fitted to the best possible line shape in order to evaluate the response of the G+ in spite of G-. Although, fittings were applied only to those spectra in which G+ and G- were found distinguishable. These observations on HiPcoM' are applicable to HiPcoM, which was treated similarly and whose spectra measured under pressure are shown in fig. 4.1b.

Figures 4.2 a and b show the G-band spectra at selected pressures of HiPcoF and HiPcoE samples, respectively. The graphs show that G-band line shape does not change meaningfully up to at least 1.5 or 1.2 GPa in HiPcoF and HiPcoE cases, allowing to fit the spectra by three peaks for the G- and one for the G+ feature, similarly to the characterization at ambient pressure. However, at 2.5 or 2.6 GPa for HiPcoF or HiPcoE respectively, the G- line shape changed to a single band, for which attempting to fit three peaks results in unsettling positions and error bars. Therefore, for both samples, G- was fitted by a single peak for all further measured spectra. The resulted  $\omega_{G_i}$  values of HiPcoF and HiPcoE are plotted as functions of pressure in figures 4.3 a and b, respectively.

Similar analysis was carried for ArcF and ArcE samples, from which a few selected spectra measured at different pressures are shown in figures 4.4 a and b, respectively. For both samples, peak fitting was initially carried out setting up two peaks to account for G- and G+. From the obtained the data, G- and G+ are spectrally resolved only up to

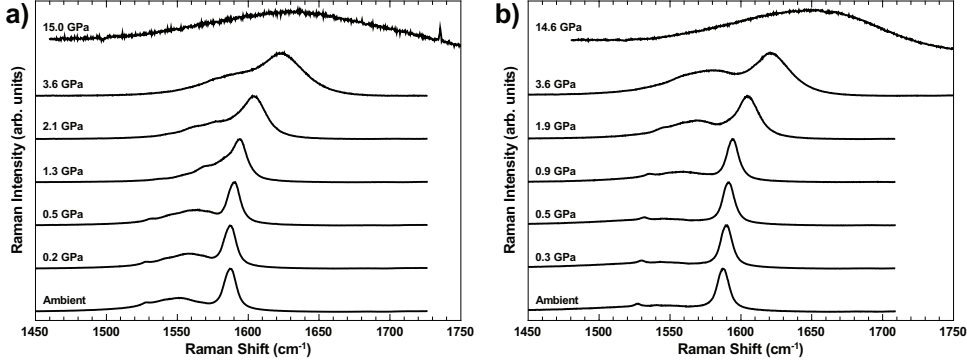


**FIG. 4.1:** *G*-band spectra under pressure of HiPcoM' (a) and HiPcoM (b) samples. Excitation wavelength was 568.5 nm. Pressure values are labeled.

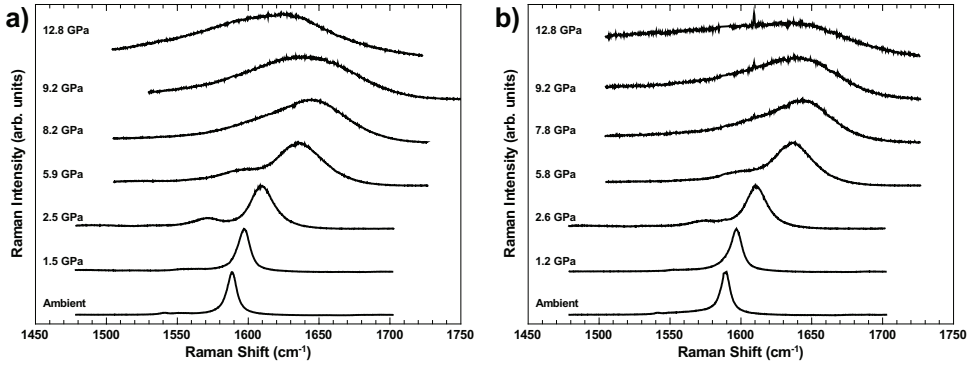


**FIG. 4.2:** *G*-band spectra under pressure of HiPcoF (a) and HiPcoE (b) samples. Excitation wavelength was 647.1 nm. Pressure values are labeled.

4.0 GPa in ArcF and 3.9 GPa in ArcE. Under higher pressures, as the G-band approaches a symmetric line shape, G+ and G- become inseparable and then they cannot be further fitted. Thus, the obtained  $\omega_{G_i}$  values for ArcF and ArcE samples are plotted as functions of pressure in figures 4.5 a and b, respectively.

Having obtained  $\omega_{G_i}$  from fitting the spectra, pressure derivatives were evaluated comprising the hydrostatic range, which has an upper limit of  $\sim 2$  GPa. Figures 4.6 a to f show  $\omega_{G_i}$  plotted as functions of pressure of all samples. On the diverse graphs, squares and circles label  $\omega_{G-}$  and  $\omega_{G+}$  obtained from the Voigts, lines represent fittings applied to evaluate the pressure derivatives. For HiPcoM',  $\omega_{G+}$  shows a non linear response, prompting a second degree polynomial fitting. The resulting first ( $\alpha_{G+} = \partial\omega_{G+}/\partial P$ ) and second ( $\beta_{G+} = \partial^2\omega_{G+}/\partial P^2$ ) order derivatives are respectively  $11.5 \pm 0.1 \text{ cm}^{-1}\text{GPa}^{-1}$  and  $-3.1 \pm 0.1 \text{ cm}^{-1}\text{GPa}^{-2}$ . Proceeding similarly for HiPcoM, one has respectively  $8.1 \pm 0.3 \text{ cm}^{-1}\text{GPa}^{-1}$

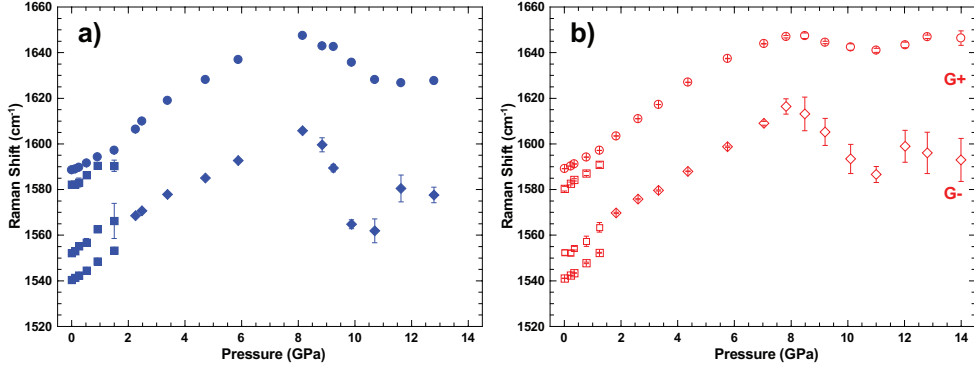


FIG. 4.3:  $G$ -band  $\omega_{G^-}$  and  $\omega_{G^+}$  as functions of pressure of HiPcoF (a) and HiPcoE (b) samples. Solid and hollow symbols indicate water-filled and empty configurations, respectively, as well blue and red colors. Circles and squares indicate  $G^+$  and  $G^-$  features, respectively.

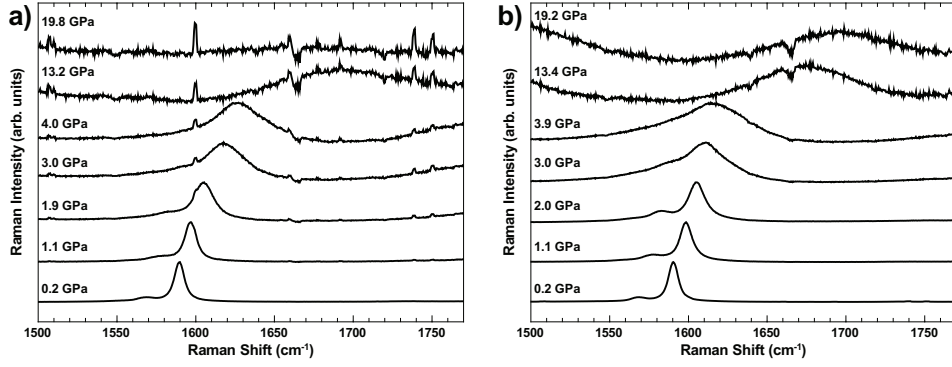
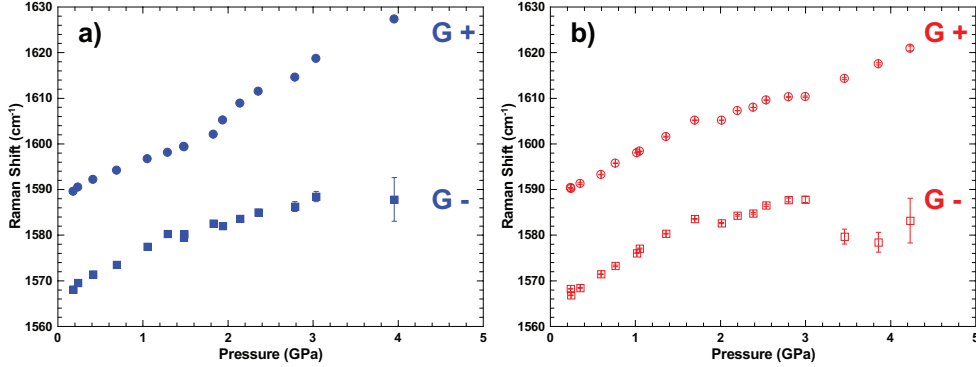


FIG. 4.4:  $G$ -band spectra under pressure of ArcF (a) and ArcE (b) samples. Excitation wavelength was 514.5 nm. Pressure values are labeled.

and  $-1.1 \pm 0.3 \text{ cm}^{-1}\text{GPa}^{-2}$ . Because of this small second order derivative which has large error, a linear fitting was also applied to  $\omega_{G^+}$ , giving  $\alpha_{G^+} = 7.0 \pm 0.2 \text{ cm}^{-1}\text{GPa}^{-1}$ . Contrarily to these two samples, the other four show their  $\omega_{G_i}$  parameters responding linearly, at least for the studied pressure range. For an easier comparison, the derivatives ( $\alpha_{G_i} = \partial\omega_{G_i}/\partial P$ ) of  $G^-$  and  $G^+$  are listed for ArcE—F and HiPcoE—F samples in table II.

TABLE II: Pressure derivatives of  $G$ -band modes. All values are in  $\text{cm}^{-1}\text{GPa}^{-1}$  units.

| HiPco  | $G_L^-$       | $G_H^-$        | $G_M^-$        | $G^+$          |
|--------|---------------|----------------|----------------|----------------|
| Empty  | $9.5 \pm 0.3$ | $9.5 \pm 1.2$  | $8.4 \pm 0.4$  | $6.6 \pm 0.1$  |
| Filled | $9.0 \pm 0.4$ | $11.5 \pm 1.2$ | $10.3 \pm 0.9$ | $6.5 \pm 0.2$  |
| Arc    |               |                | G-             | G+             |
| Empty  |               |                | $12.0 \pm 0.2$ | $10.4 \pm 0.4$ |
| Filled |               |                | $10.0 \pm 0.4$ | $7.1 \pm 0.3$  |



**FIG. 4.5:**  $\omega_{G_i}$  as a function of pressure of ArcF (a) and ArcE (b) samples. Solid and hollow symbols indicate water-filled and empty configurations, respectively, as well blue and red colors. Circles and squares indicate G+ and G- features, respectively.

## IV.2 ON THE ANALYSIS OF THE G-BAND

Before proceeding the discussion, it is worthy to comment on the usual methodology found in the literature to analyze the G-band. At lower pressures, G+ and G- features are usually peak fitted as long as they are distinguishable and can furnish  $\omega_{G+}$  and  $\omega_{Gm}$  parameters. At higher pressures, upon G+ and G- lose their individual resolutions, the G-band is fitted by a single peak or simply the frequency value at the maximum intensity of the G-band ( $\omega_{Gm}$ ) is studied as a function of pressure. Then, provided that  $\omega_{G+}$  or  $\omega_{Gm}$  do not depend strongly on  $d_t$ , the resulted pressure dependence is averaged for the entire diameter distribution of the sample. Nonetheless, even though this approach bypasses the issue of losing G+ and G- resolution, it has issues to be addressed.

As shown in fig. 1.19, at pressures  $\pm 8$  GPa, G- and G+ are well separated in methanol:ethanol mixture but conversely they are not if argon is the PTM instead. Thus, not only pressure but also the environment (the used PTM) influences the broadening of the G-band and the resolution of its features<sup>54</sup>. Therefore, there is no evidence allowing to assume that the symmetric and broadened G-band observed at higher pressures is either equivalent to or carries mostly the contribution of G+. Nevertheless, this assumption is done whenever  $\omega_{Gm}$  or  $\omega_{G+}$  are plotted against pressure. Whenever G+ and G- are distinct peaks,  $\omega_{Gm}$  equals to  $\omega_{G+}$ , carrying information on just one feature of the G-band. Otherwise,  $\omega_{Gm}$  is the center of the G-band feature as a whole, which cannot be simply assigned to the G+ feature. In a few words,  $\omega_{Gm}$  has different meanings depending on the line shape of the G-band.

Once G+ and G- resolution is lost, either  $\omega_{G+}$  or  $\omega_{Gm}$  are unsuitable parameters for analyzing the G-band within a full pressure cycle. Thus, for evaluating how the G-band

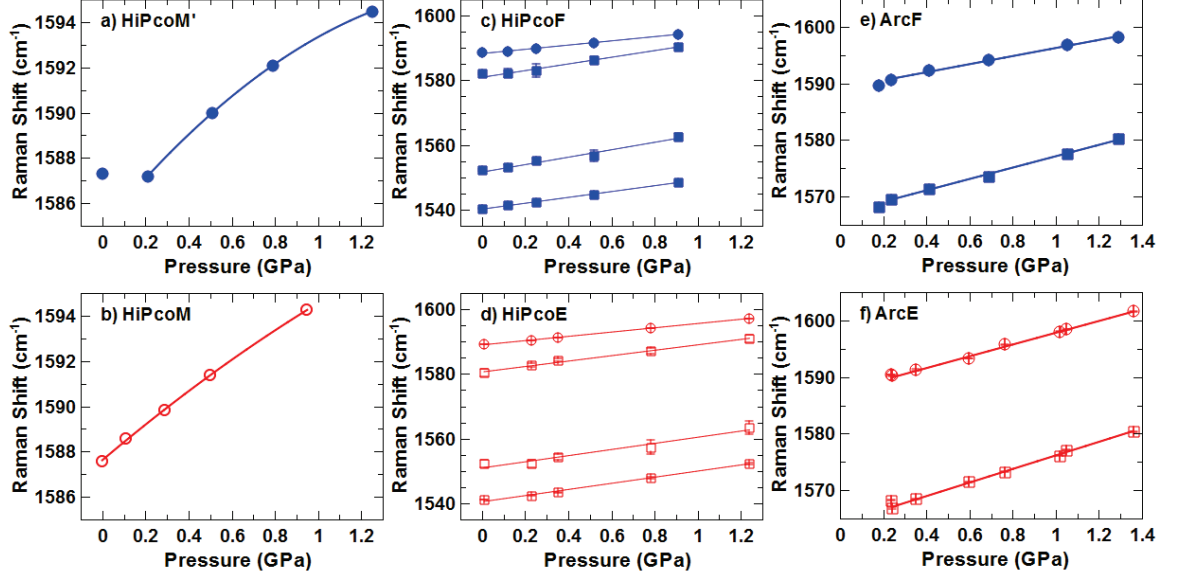


**FIG. 4.6:**  $G$ -band,  $\omega_{G_i}$  as function of pressure. Blue and red colors as well solid and hollow symbols indicate water-filled and empty configurations. Dashed and solid lines are respectively second and first order polynomial fittings applied to the data. a) HiPcoM'. b) HiPcoM. c) HiPcoF. d) HiPcoE. e) ArcF. f) ArcE.

evolves as a whole feature, a different parameter must be proposed. It must be evaluable for each spectrum in spite of the line shape (which changes with pressure or with PTM) and also carry information simultaneously on  $G+$  and  $G-^1$ . Therefore, this parameter is defined by accounting all  $j$  frequencies comprising the  $G$ -band spectrum ( $\omega_{G_j}$ ) weighted by their respective intensities ( $\Lambda_{G_j}$ ), namely:

$$\omega_{G_c} = \frac{\sum_j \omega_{G_j} \Lambda_{G_j}}{\sum_j \omega_{G_j}} \quad (\text{IV.2.1})$$

Thinking on frequency and intensity as position and mass respectively, the suggested parameter  $\omega_{G_c}$  is very analogous to a center of gravity (CoG)<sup>2</sup>. Even though CoG can be calculated in spite of  $G$ -band line shape, some precautions must be observed to use this parameter.

For the case of samples having large diameter distributions, different SWNTs (having distinct diameters) match resonance conditions as the pressure increases. Reminding that each measured spectrum comprises the entire sample, because  $\omega_{G_i}$  depends on  $d_t$ , the many distinct SWNTs will contribute randomly to the  $G-$ . Precisely, both pressure-induced mechanical modifications and pressure-selectivity of resonance conditions can modify the

<sup>1</sup>Equivalently, carry information on both LO and TO phonons of the  $G$ -band.

<sup>2</sup>This parameter was originally proposed by Sofie Cambre.

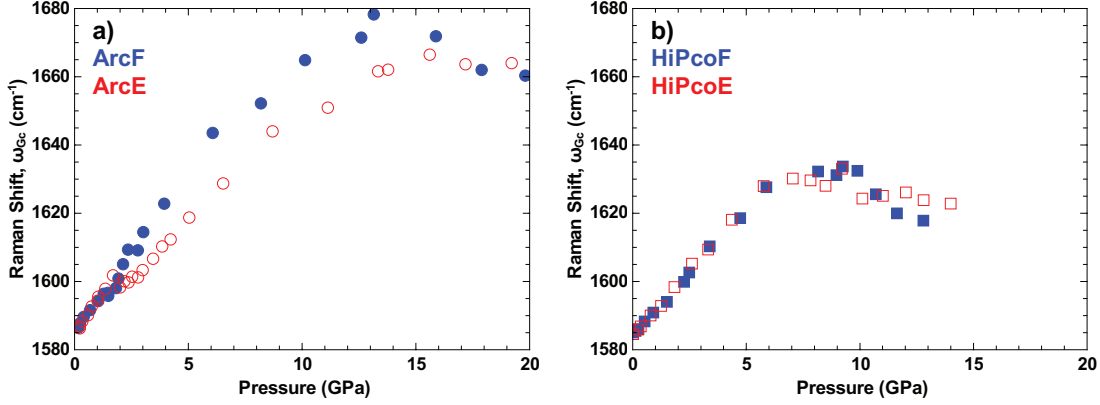


**FIG. 4.7:** *G*-band analysis,  $\omega_{Gc}$  as a function of pressure. Blue and red colors as well solid and hollow symbols indicate water-filled and empty configurations, respectively. Circles and squares encode Arc and HiPco derived samples, respectively. a) ArcF and ArcE. b) HiPcoF and HiPcoE.

line shape, frequency and width of the spectrum. Therefore, while studying the pressure response of CoG, variations in the curve due to the modification of resonance conditions could be wrongly assigned to mechanical modifications, or the inverse. Samples having metallic SWNTs also must be treated cautiously by the CoG approach because of the electron-phonon coupling, specially if the BWF function must be used to fit the spectra.

The CoG parameter is suitable to analyze SWNT samples having narrow diameter distributions and semiconducting SWNTs. ArcF and ArcF samples match well these conditions. Nevertheless, evaluation of CoG in spectra of the HiPco derived samples must be carried cautiously. HiPcoF and HiPcoE have metallic and semiconducting SWNTs, whose diameter distributions are respectively  $1.26 \pm 0.1$  nm and  $0.82 \pm 0.1$  nm. Under lower pressures, this initial assignment can be fully trusted. As the RBMs of the semiconducting ones (see fig. 2.3) are much stronger than those of the metallic ones, the former can be expected to dominate the G-band spectra. Under high pressures however, new resonance conditions take place and more SWNTs contribute to the G-band. Even if no new upcoming RBM resonances appear and those initial of the semiconducting SWNTs can be measured above 10 GPa, it must be reminded that G-band has a much broader resonance window than RBMs. Therefore, the lack of RBM signal does not mean that G-band will not be measurable. The  $\omega_{Gc}$  parameter was evaluated for the G-band spectra of ArcF and ArcE samples. They are plotted as functions of pressure in fig. 4.7a. This parameter was also evaluated for the HiPcoF and HiPcoE, though some considerations will be remarked for their interpretations.

### IV.3 SPECTRAL LINE SHAPE

Regarding all samples,  $\omega_{G_i}$  blue-shifts and  $\Gamma_{G_i}$  broadens under lower pressures, which happens due to the shortening of the C-C bonds. This broadening of  $\Gamma_{G_i}$  hasten beyond  $\sim 2.0\text{GPa}$ . This vale of pressure coincides to the transition from hydrostatic to non-hydrostatic limit, suggesting an inhomogeneous application of pressure upon solidification of the environment. Noticeably, the G-band of all samples experiment a progressive loss of intensity with the increasing pressure. For instance, in HiPcoE sample, the plasma line  $\sim 1609\text{ cm}^{-1}$ , being just visible at 9.2 GPa, surpasses the G-band maximum intensity at 12.8 GPa. As other example, in the ArcF sample, the G-band is barely mensurable at 19.8 GPa. It must be reminded that while applying pressure, the gasket becomes thinner, which changes the optical path and consequently may contribute to the loss of intensity. Other qualitative observations were made for each sample individually.

In respect to the G-band spectra of HiPcoM' and HiPcoM samples, the G- profile changes often with the increasing pressure. Reminding that the G- feature is highly sensitive to  $d_t$  and metallicity, some causes can be suggested. (i) As the pressure increases, it modifies the geometry of the many SWNTs present in the sample. By modifying the structure, the  $E_{ii}$  values are also changed, which enhances the resonance conditions for certain SWNTs but worsen for others, which was demonstrated by changing the excitation energy in other studies<sup>136</sup>. Consequently, the spectral changes of G- would be associated with changing resonant conditions. (ii) There is a change into the metallic characteristics of these SWNTs, which invariably changes the G- line shape. (iii) The pressure-induced modifications is very particular for a given (n,m) SWNT, hence there is sensitive not only to diameters, but to chiral angle and as well to metallic or semiconductor characteristics. It is important to remark that these suggestions are not self excluding. Anyhow, these many spectral changes combined with the large diameter distribution do not allow to perform an analysis for the G- in these samples. Being impossible to assign the G-band to a determined set of SWNTs, evaluating the  $\omega_{G_c}$  parameter is useless. Regarding the G+ feature, an analysis is limited up to pressures  $\pm 8\text{ GPa}$ , from which their G-bands become large and symmetrical.

By looking the spectra of both HiPcoF and HiPcoE samples upward in pressure, one verifies the G- feature steadily gaining intensity relatively to the G+. Conversely, the increase of intensity in G- is much less important in ArcF and ArcE. At the higher pressures, as exemplified by the spectra measured  $\pm 8, 9$  and  $13\text{ GPa}$ , the G-band in HiPcoF and HiPcoE keeps an asymmetrical shape in spite of their line width broadening. While these two samples do not lose their G—G+ resolution within the studied pressures, the G-band spectra of ArcE—F and HiPcoM—M' show total loss of resolution at  $\pm 6.0\text{ GPa}$  and  $8.0$

GPa, respectively.

The loss of the asymmetric shape for the G-band is demonstrated to change not only with the pressure, but also with the environment<sup>118</sup>. In this work however, all experiments were performed under the same environment. By observing that ArcE(F) and HiPcoE(F) have respectively larger and smaller diameter distributions, but the former show loss of G-/G+ resolution at considerable lower pressure, it can be suggested that this event has a link to the cross-section modification. Upon the flattening of the nanotube wall, the cylindrical symmetry is certainly lost. Therefore, it is reasonable to think that G+ and G- would not exist as separate features after the full collapse since they are originated by the symmetry breaking upon rolling up the monolayer graphene.

#### IV.4 IRREVERSIBLE CHANGES INDUCED BY PRESSURE

The G-band spectra can give insight on irreversible modifications induced by pressure. For this end, spectra before and after the pressure cycles are superposed in figures 4.8 a to d<sup>3</sup>.

In HiPcoM' case, relative intensities of G- and G+ are conserved before (blue) and after (gray) the cycle while G+ broadened and G- experienced several alterations. The feature ( $\sim 1550 \text{ cm}^{-1}$ , before cycle) associated to the SWNTs having large diameters is recovered, though slightly red-shifted, showing that these SWNTs were structurally modified at some degree. Upon recovery, the lowest frequency portion of the spectrum is evidently broadened and asymmetric in shape, which suggests that the electronic structure of some SWNTs were modified. The sharp peak  $\sim 1527 \text{ cm}^{-1}$  is also recovered. This frequency value roughly corresponds to  $d_t \sim 0.86 \text{ nm}$ , giving one more evidence that thinner SWNTs tend to be more resilient against pressure.

In HiPcoM, all G-band features were recovered, though with few differences. In respect to G+, the G- feature  $\sim 1550 \text{ cm}^{-1}$  reappears less intense than previously, suggesting that thick diameter SWNTs experienced irreversible modifications. The lowest frequency portion reappears though slightly broadened. The sharp peak  $\sim 1527 \text{ cm}^{-1}$  is also recoverable.

In HiPcoF and HiPcoE, all spectral features reappeared upon release of pressure. Very slight changes were observed for frequency and FWHM of the G- peak associated to the metallic SWNTs.

---

<sup>3</sup>Attempts to measure the spectra of the Arc samples after their pressure cycles failed due to a technical impediment. As the PTM remains solid upon releasing the force applied over the diamonds, a hand driven opening and closing was required to reach ambient pressure. In this process, loss of sample is unavoidable, which is critical considering the volume used of Arc derived samples, ten times less than that used of the HiPco.

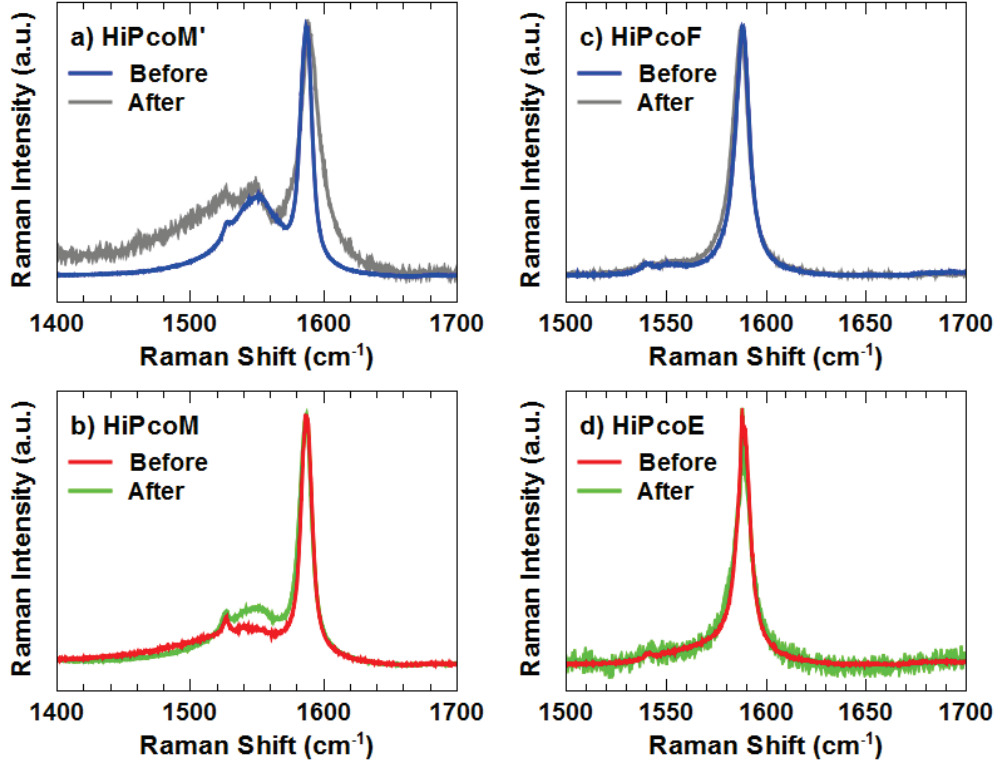


FIG. 4.8: *G*-band spectra before and after the pressure cycles. Legends are conveniently placed for all samples. a) HiPcoM'. b) HiPcoM. c) HiPcoF. d) HiPcoE.

#### IV.5 PRESSURE DERIVATIVES UNDER HYDROSTATIC CONDITIONS

The pressure derivatives of the *G*-band for Arc discharge derived SWNTs can be found in different works in literature. Although, all values were evaluated in bundled SWNTs. As the Arc derived SWNTs studied in this work are unbundled, a comparison among results follows, taking into account experiments on samples derived by same synthesis method, thus having approximate diameter distributions, performed with the same 2.41 eV excitation energy and considering the pressure ranges for which hydrostatic conditions can be assumed.

For the ArcE case, the pressure derivative of the *G*+ ( $10.4 \pm 0.4 \text{ cm}^{-1}\text{GPa}^{-1}$ ) resembles the value obtained for bundled Arc discharge SWNTs compressed without PTM ( $9.6 \pm 0.9 \text{ cm}^{-1}\text{GPa}^{-1}$ )<sup>21</sup> and in paraffin oil environment ( $10.0 \pm 1.0 \text{ cm}^{-1}\text{GPa}^{-1}$ )<sup>54</sup>. For the ArcF case however, the pressure slope ( $7.1 \pm 0.3 \text{ cm}^{-1}\text{GPa}^{-1}$ ) is closer to the value reported for bundled Arc discharge SWNTs, though compressed in 4:1 methanol:ethanol mixture ( $6.5 \pm 1.0 \text{ cm}^{-1}\text{GPa}^{-1}$ )<sup>54</sup>. An intermediate value of  $8.0 \pm 0.5 \text{ cm}^{-1}\text{GPa}^{-1}$  is reported while using pure ethanol as the PTM<sup>120</sup>.

One high-pressure study on bundled Arc discharge SWNTs considering various types of

PTM found the pressure derivative of G+ ranging from  $9.0 \pm 0.6$  to  $10.6 \pm 0.2 \text{ cm}^{-1}\text{GPa}^{-1}$ . In this study, the PTM was suggested to permeate the interstitial space in bundles and the difference of values for the slopes was suggested to be a consequence of the different permeations given by each PTM<sup>119</sup>. In this scenario, pressure would be transmitted not only externally to the entire bundles, but also between the SWNTs by the liquid occupying the interstitial spaces.

Considering the Arc discharge derived samples, the agreement among values of  $\alpha_{G+}$  obtained for the surfactant individualized in this work and for the bundled configurations found in literature leads to suggest that inter-tube interactions in bundles does not affect strongly how the G+ feature evolves with the pressure, at least for the studied diameters. This result allows a direct comparison among the G-band evolutions under pressure shown in this work (unbundled) and those of the literature (bundled).

The pressure derivatives of the G+ of both HiPcoE ( $6.6 \pm 0.1 \text{ cm}^{-1}\text{GPa}^{-1}$ ) and HiPcoF ( $6.5 \pm 0.2 \text{ cm}^{-1}\text{GPa}^{-1}$ ) well correspond to a previously estimated value for HiPco SWNTs  $\sim 6.4 \text{ cm}^{-1}\text{GPa}^{-1}$ <sup>84</sup>. This later value was estimated for SWNTs either individualized by surfactant (sodium-cholate:D<sub>2</sub>O solution) or by deposited onto glass microfibers (compressed in 4:1 methanol:ethanol mixture), probed with the same 633 nm wavelength in both cases.

Pressure derivatives are not vastly reported for G- feature as they are for the G+. Possibly because of large diameter distributions of the tried samples, which associated to the dependence of  $\omega_{G-}$  on  $d_t$  complicates the analysis of the G- feature. In this work, the optimal diameter sorting allowed such analysis. The ArcE sample shows  $\alpha_{G-}$  ( $12.0 \pm 0.2 \text{ cm}^{-1}\text{GPa}^{-1}$ ), larger than ArcF ( $10.0 \pm 0.4 \text{ cm}^{-1}\text{GPa}^{-1}$ ). For the HiPcoE and HiPcoF samples, each of the two lower frequency G- components show  $\alpha_{G-}$  values being equal by their error bars, respectively  $9.5 \pm 0.3 \text{ cm}^{-1}\text{GPa}^{-1}$  and  $9.0 \pm 0.4 \text{ cm}^{-1}\text{GPa}^{-1}$  or  $9.5 \pm 1.2 \text{ cm}^{-1}\text{GPa}^{-1}$  and  $11.5 \pm 1.2 \text{ cm}^{-1}\text{GPa}^{-1}$  for empty or water-filled configurations. The G- component which is closer in frequency to the G+ however, it shows higher values upon water-filling. Since this component (centered  $\sim 1580 \text{ cm}^{-1}$  at ambient pressure) is assigned to metallic SWNTs, which have a better polarizability, this increasing value of  $\alpha_{G-}$  may be due to an interaction with the polar water-filling molecules. It is remarkable that any of the G- components shifts much faster than G+ for each sample individually, suggesting that the transversal direction is softer than the axial.

Regarding ArcE, HiPcoM and HiPcoE samples, which have mostly empty SWNTs,  $\alpha_{G+}$  increases with diameter, which suggests that thicker SWNTs are generally more compressible than thinner ones. Comparing  $\alpha_{G+}$  of ArcE and ArcF, which have same diameter distribution but opposite empty and water-filled configurations, the pressure derivatives of

both G+ and G- are larger for the empty SWNTs. This fact can be explained by suggesting that the presence of water inside these SWNTs provides mechanical support, which turns them less compressible and consequently lowers the pressure derivative.

Conversely to the Arc samples, whose  $\alpha_{G+}$  increases upon water-filling, HiPcoE and HiPcoF show equal values within error bars. One possible explanation may be linked to a lesser compressibility of the SWNTs having smaller diameters, which would require more pressure to be strongly forced against the filler content. A second suggestion would come from the influence of filling. Following results from computer simulations<sup>13</sup>, the SWNTs of the ArcF sample ( $\langle d_t \rangle = 1.32 \pm 0.08$  nm) can be expected to comport layered configurations of water molecules, whereas the semiconducting SWNTs of the HiPcoF sample ( $\langle d_t \rangle = 0.82 \pm 0.1$  nm) are more likely to comport single-file water-filling. Thus, the equality of  $\alpha_{G+}$  for small diameters and inequality for large ones could be linked to different influence of filling configurations.

The strong non-linear response to hydrostatic compression shown by G+ on HiPcoM' contrasts with the results shown by the other samples. In HiPcoM case, the very small value obtained for the second order derivative can be explained by the presence of water-filled SWNTs, reminding that the empty-labeled samples are not composed of solely empty SWNTs. HiPcoE—E and ArcE—F responded linearly.

Considering the SWNTs present in HiPcoM' sample, those which contribute more strongly to the G-band are metallic, having  $\langle d_t \rangle = 1.15 \pm 0.2$  nm whereas the SWNTs of ArcF are semiconducting, having  $\langle d_t \rangle = 1.32 \text{ nm} \pm 0.2$  nm. As both samples have mainly water-filled SWNTs, filling solely cannot explain the non linear response. As the metallic SWNTs ( $\langle d_t \rangle = 1.26 \pm 0.1$  nm) show linear response, effects due to metallicity only can be ruled out. Both ArcE and HiPcoE show linear response, thus excluding diameters as an single cause. Therefore, non linear pressure response of the G+ is observed for SWNTs matching simultaneously three criteria: large  $\langle d_t \rangle$ , metallic and filled.

In case of graphite, the anharmonicity of the C-C vibrations leads to a non linear response to pressure of the G-mode<sup>129</sup>. Perhaps, water-filling in amounts possible to be find only inside large diameters can somehow interfere on the polarizability of the wall in metallic SWNTs, leading to a anharmonic response of the vibrational mode. Although, such suggestion requires more clarifications which cannot be given by the data presented here.

## IV.6 COLLAPSE

In literature, the pressures for which SWNTs undergo collapse are estimated by analyzing the G-band response. Mostly of the works rely only on how  $\omega_{G+}$  evolves, as summarized

by the review in Chapter 1. Upon the onset of collapse, the cross-section of a SWNT must change from circular to elliptical, racetrack or peanut like shapes. Therefore, the cylindrical symmetry is expected to change stronger in the transversal than longitudinal direction. In the case of armchair SWNTs, for which the G+ feature originates from TO phonons, the evolution of  $\omega_{G+}$  could be assumed to carry mostly of the information on the change of curvature of the wall and the consequent cross-section modification. In the case of chiral semiconducting SWNTs however, as their G+ and G- originate respectively from LO and TO phonons, the evolution of both  $\omega_{G-}$  and  $\omega_{G+}$  must be considered.

Analyzing the pressure response of  $\omega_{G-}$  and  $\omega_{G+}$  for the ArcF sample in fig. 4.5a, one verifies that both parameters blue-shift steadily up to 1.5-1.8 GPa. Thereafter, their behavior split:  $\omega_{G+}$  shows a non linear evolution whose slope is clearly increased, whereas  $\omega_{G-}$  show a slower pace increasing. For comparison, the pressure response of the ArcE sample is shown in fig. 4.5b. Even showing different slopes than those of ArcF, both  $\omega_{G-}$  and  $\omega_{G+}$  also evolves smoothly up to 1.7-2.0 GPa. Further,  $\omega_{G+}$  experiences a drastic reduction of slope and shows a leveling at 2.8 GPa, which is similarly observed for  $\omega_{G-}$ . For the next measurement of ArcE up in pressure, at 3.4 GPa,  $\omega_{G+}$  experiences a meaningful increasing of slope, though lower in value than that shown below 1.7 GPa. Nevertheless, from 3.4 GPa, the most expressive change is observed for the  $\omega_{G-}$ , whose value drops and considering the error bars, it levels off. This change of behavior in  $\omega_{G-}$  observed for the empty SWNTs is accompanied by the vanishing of the RBM resonances in between 3.4 to 3.8 GPa. However, by the ArcF sample, it was observed that the water-filled SWNTs continue to show RBM modes up to at least 13 GPa.

The leveling of the G-band evolution is interpreted as the onset of the collapse<sup>124</sup>. By observing the leveling of the G-band followed by the loss of RBM resonances in ArcE sample, it can be clearly suggested that the empty SWNTs collapse at about 3.4 - 3.8 GPa. Notably, this pressure value agrees well with theoretical predictions. Remarkably, the splitting observed on the behavior of the G-band of ArcE and ArcF samples occurs at pressures close to that hydrostatic conditions are lost. If it is not a coincidence, upon loss of hydrostaticity, it can be suggested that different stress components in the solid environment would favor the cross-section modification.

Through the evolution of the G-band, a simple figure about how a SWNT shape evolves can be constructed. Certainly, the SWNT volume must decrease upon pressure application. At lower pressures, the C-C bonds shorten (which is shown by the increasing phonon frequency) to account for the volumetric reduction. Upon further increasing of pressure, the C-C bonds shorten at lower rate up to a limit for which no further shortening is possible for accommodating the volumetric reduction. Therefore, another degree of freedom must

be considered. The only possibility would be change the angles between consecutive C-C bonds, bending the nanotube wall and consequently leading to the ovalization. Then, the limit case for the ovalization is the collapse. Upon reaching the collapsed geometry, as the nanotube wall is flattened, the G-band would resume the blue-shift response, though at smaller rate than shown while having tubular symmetry, or even blue-shifting similarly to graphite.

Because of G- and G+ become inseparable for both ArcF and ArcE at about 4 GPa, any further analysis must be done by their  $\omega_{Gc}$  parameter, whose responses to the pressure are shown by figures 4.7a and b. Depending on the observed pressure range, the two curves in the graph show different phases, which are described as follows.

For the ArcE case: (i) 0.2 to 1.7 GPa: blue-shift; (ii) 2.0 to 3.0 GPa: leveling; (iii) 3.4 to 8.7 GPa: low rate blue-shift (iv) 11.1 to 19.2 GPa: graphite-like behavior. Therefore, phase *i* correspond to the C-C hardening analogously to the response given by  $\omega_{G+}$ . As RBMs are still observed within the entire phase *ii*, the collapse process, e.g., ovalization to racetrack or peanut like shape is estimated to begin at 2.0 GPa and finish upon the sure loss of the RBM modes accompanied by the change of slope observed for G- at 3.8 GPa. Phases *iii* and *iv* show the post collapse evolution, which reasonably can be suggested as similar to two planes of graphite, or two-layer graphene.

For the ArcF case: (i) 0.2 to 1.5 GPa: blue-shift; (ii) 1.8 to 2.4 GPa: high rate blue-shift; (iii) 2.8 to 12.6 GPa: non-linear blue-shift; (iv) 13.2 to 19.8 GPa: red-shift. Thus, phase *i* corresponds to the evolution of  $\omega_{G+}$  mainly. In phase *ii*, the filler mechanically counters the ovalization by forcing a strong hardening of the C-C bonds. The transition from phase *ii* to *iii* is followed by the onset of the new RBM feature discussed last chapter, which is associated to the curved edges of the nanotubes while assuming the new shape upon reduction of volume. The inflexion of the curve which marks the transition from phase *iii* to *iv* corresponds to a second signature of collapse given in literature<sup>53</sup>. Finally, phase *iv* would correspond to the collapse process of the water-filled SWNTs, with onset at 13.2 GPa and finishing at 17.9 GPa.

The pressure response of the G-band was also analyzed for the HiPcoF and HiPcoE samples. In respect to both samples, as shown by fig. 4.3,  $\omega_{G-}$  and  $\omega_{G+}$  show a steady blue-shift below 2 GPa, for which pressure slopes were discussed. Thereafter,  $\omega_{G-}$  and  $\omega_{G+}$  experience an increasing to their slopes, lasting up to about 8 GPa. From then, for HiPcoF,  $\omega_{G+}$  show inflection whilst for HiPcoE, it shows a mix of inflection and leveling. Also,  $\omega_{G-}$  drops in value and levels off. Additionally, the evolution with pressure of the  $\omega_{G+}$  parameter was also analyzed by the graphs show in fig. 4.7b. For both samples, three different evolutions can be observed: (i) blue-shift; (ii) slightly increased blue shift; (iii)

the collapse process. A curious observation for these two HiPco samples is the collapse signature appearing  $\sim 8$  GPa for both, regardless of empty and filled configurations.

Albeit the responses of the G-band suggest the onset of collapse for HiPcoF and HiPcoE, some remarks must be made on the diameter distributions of these samples. Semiconducting and metallic SWNTs were found resonant at ambient pressure, having diameters centered at about 0.82 and 1.26 nm, respectively. As shown in last chapter, the RBMs of the semiconducting were measurable up to 10 GPa and at least up to 14 GPa for HiPcoE and HiPcoF. Because there is no possibility for a empty, collapsed SWNT show RBM, the transition spotted at about 8 GPa through the G-band cannot be assigned to the semiconducting SWNTs identified at ambient pressure. Also, the metallic SWNTs were found collapsed  $\sim 4$  GPa.

To explain why the G-band spectrum shows the collapse signature whereas the RBM spectrum show resonances for the HiPcoF and HiPcoE samples, one needs to consider the resonance conditions. It must be reminded that G-band can be resonant with the incoming or the scattered photon whilst the RBM can be resonant with the former only. Thus, the G-band has a larger resonance window. With the increasing pressure and consequent shift of the Kataura plot, the G-band modes of different SWNTs can become resonant, but not necessarily the RBM modes. Indeed, this pressure selectivity can be favored for samples having broad diameter distributions, which is the case of the experimented HiPco samples. Therefore, the most logical explanation for the mismatched information given by G-band and RBM spectra of these HiPco samples is that with the increasing pressure, the RBM and G-band are given by different SWNTs. As by the obtained data it is impossible to assert the diameter distribution at higher-pressures, the collapse signature given by the G-band of the studied HiPco samples cannot be attributed to specific diameters. Although, knowing that the energies in the Kataura plot down shift the with pressure, it can be suggested that the observed collapse signature must be given by SWNTs whose diameters are thicker than those showing RBMs at 8 GPa and above, but at same time thinner than those of Arc samples.

Upon the collapse onset, it was found that samples having mostly empty SWNTs (ArcE and HiPcoE) show leveling whereas those having mainly water-filled SWNTs (ArcF and HiPcoF) show inflexion par their G-band responses to pressure. Since empty and filled states can be trusted for the studied samples, the comparison suggests that leveling and inflection are the signatures of collapse for respectively empty and filled SWNTs. This finding may bring some clarification to the disagreement between theoretical predictions and experimental investigations on the pressure required to collapse SWNTs.

As shown in last section, the pressure derivatives were found quite similar for either

unbundled or bundled SWNTs, which suggests that the hardening of the C-C bonds itself may not depend strongly on inter-tube interactions. Remarking as well that values for unbundled and bundled were found for different PTMs, the environmental role, even being crucial for  $E_{ii}$ , it may not affect strongly the C-C hardening upon pressure<sup>4</sup>. Thus, it will be assumed that there are no forbidding constraints to compare the collapse pressures  $P_c$  obtained by this set of experiments for unbundled and those found in literature for bundled SWNTs. For the following discussion, it is also important to remind that this work spots the collapse by using the  $\omega_{G_c}$  parameter instead of  $\omega_{G+}$ , thus, is possible that some  $P_c$  values were not reported accurately.

For bundled, open-ended Arc SWNTs ( $d_t \sim 1.35$  nm) excited at 514.5 nm, the evolution of the G-band (see figure 1.19) shows a inflection  $\sim 14$  GPa or  $\sim 15$  GPa while compressed in paraffin oil or methanol:ethanol mixture respectively<sup>54</sup>. These values of  $P_c$  are close to the  $\sim 13.2$  GPa found for the water-filled Arc SWNTs in this work, and they are much higher than the theoretically predicted for empty SWNTs having such diameters. Therefore, as these SWNTs were open, the observations indicate that they could have been filled by the PTM, which would explains the increasing of the collapse pressures as well the same kind of signature for the G-band.

In argon environment, there are conflicting results for Arc SWNTs at the same 514.5 nm wavelength, showing no evidence of collapse up to  $\sim 38$  GPa<sup>118</sup> or an onset  $\sim 10$  GPa<sup>54</sup>. Although, the later study compared the spectra  $\sim 4$  GPa of the two studies, which revealed different line shapes. The latter also reported an increasing of the line width in between 2 to 4 GPa. Therefore, the possible explanation is that these two studies investigated on different SWNTs.

Another disagreement is found for SWNTs compressed in methanol:ethanol mixture, for which the collapse is reported  $\sim 14$  GPa<sup>54</sup> and undetected up to  $\sim 43$  GPa<sup>53</sup>. It must be remarked that the synthesis method are not the same in these investigations, which could mean different targeted SWNTs and therefore distinct responses to pressure. Moreover, the data points given by the later study are scattered, very spaced on the pressure scale and thus difficult to interpret. For instance, considering the ArcE sample, if the data points were suppressed in between 3 to 4 GPa (see fig. 4.7), the phase transition would pass unseen.

In literature, the G-band data under pressure for HiPco samples present the same issues found in this work. Nevertheless, some comparisons can take place. A clear collapse signature for HiPco SWNTs (see fig. 1.17) was found  $\sim 8.1$  GPa in liquid argon environment while probing with 830 nm wavelength<sup>124</sup>. The same study found a leveling  $\sim 8$ -10 GPa by

---

<sup>4</sup>Perhaps, the frequency shifts found upon immersion in different liquids are due to electronic shifts instead of solvation pressure.

compressing the sample without PTM, but excited at 514.5 nm wavelength<sup>5</sup>. These values correspond well to those found for the HiPco samples in this work.

Analyzing Arc and HiPco SWNTs, the obtained values for the onset of leveling or inflection of the G-band show some agreement in spite of the environment. The pressure was shown to be the main factor in all of these experiments. Even if this fact does not discard, it opens a question about how strong is the influence of the environment (and hydrostatic conditions) on the collapse pressure. Have been discussed the pressure and the environment, the next external variable (diameter and chirality are intrinsic to the SWNTs) which acts on the collapse is the filling.

For the following general comparison, it will be considered experiments performed on samples having diameter distributions centered  $\sim 1.35$  nm for SWNTs and  $\sim 1.56$  nm for DWNTs. By sorting filler (from higher to lower homogeneity) and its respective collapse pressure (approximated value in GPa units), one has: argon ( $i$  38)<sup>54</sup>, SWNT (21)<sup>51</sup>, paraffin oil (15)<sup>53</sup>, water (13.2), C<sub>60</sub> (12-13)<sup>130</sup>, I<sup>-</sup> (8-10)<sup>52</sup> and C<sub>70</sub> (8)<sup>53</sup>. Finally,  $P_c \sim 3.8$  GPa for empty SWNTs.

The whole scenario of collapse could be described as follows. The small molecules of argon would provide the fuller possible filling, giving great structural stability and explaining the unobserved collapse. A SWNT filling another (the DWNT case) provides good mechanical stability, though it lets a spacing between its wall and the outer one, lowering the collapse pressure in respect to argon. Paraffin oil, water, C<sub>60</sub> and iodides would provide less wadding because their molecules are larger than argon ones. The C<sub>70</sub>, being the largest molecules among the discussed fillers, they would be more spaced inside a SWNT, interacting less homogeneously but still providing a counter pressure support. The absence of filler (empty) shows the lowest collapse pressure. Therefore, filler content generally provides structural stability against pressure and homogeneity of filling further increases the stability.

---

<sup>5</sup>This same study shown the leveling onset at very different pressures, ranging from 2.5 to 9.4 GPa while compressing HiPco SWNTs without PTM, but changing the excitation wavelength to 633 nm or 830 nm.

## CONCLUSIONS

Pressure derivatives of the RBMs were obtained for eighteen chiralities. The values show a leveling  $\sim 6 \text{ cm}^{-1}\text{GPa}^{-1}$  for the diameters smaller than 1 nm, though steadily increasing for the diameters larger than 1.2 nm. For a few chiralities, the pressure derivatives were found to become larger upon water-filling. The obtained values are useful for future studies on the mechanical stability of SWNTs and also to evaluate the Gruneisen parameters for the RBMs.

In the case of (7,2) chirality, the pressure derivative of its RBM shows a minimum, suggesting a reduced stability due to an additional degree of freedom to accommodate the mechanical deformation, possibly related to a torsional instability predicted for diameters smaller than 1 nm and chiral angle approaching 15. The minimum is also shown upon water-filling, indicating persistence of the effect of chirality. The reduced stability of (7,2) chirality is also confirmed by observing the radial breathing modes after releasing the pressure from a maximum of 15 GPa. The water-filled (7,2) is recovered whereas the empty disappeared from the spectrum.

Regarding several chiralities, all of them having diameters smaller than 1 nm, the response to pressure of their RBM modes were found non linear. This observation took place within the estimated hydrostatic pressures, even below the 1 GPa freezing pressure of water at room temperature. Given the radial symmetry of SWNTs, for which pressure acts directly against the RBM, it can be suggested that pressure is transmitted non homogeneously in the molecular scale.

For SWNTs having very small diameters, 0.68 and 0.74 nm, RBM modes of both empty and water-filled were recovered after a pressure cycle of 15 GPa, and were observable through the whole experiment. On diameters ranging from 0.78 to 0.92 nm, RBM modes of empty SWNTs were observable up to  $\sim 10$  GPa, being recovered after cycle, though blue-shifted, indicating that they were damaged by pressure, consequently opened and become water-filled upon returning to ambient pressure. On the same diameters but water-filled, RBMs were clearly detectable through the entire pressure cycle, such was for the smaller ones. They were all recovered to their initial positions also. On larger diameters, from 1.16 to 1.36 nm, RBMs were lost above 4 GPa and unrecoverable after similar pressure cycles, indicating that SWNTs reached an irreversible collapse or they were destroyed. By observing in such order of increasing diameters respectively no, mild or severe damage upon pressure application, the stability is clearly suggested to be proportional to the inverse of the diameter.

Pressure derivatives of the G+ and G- features were obtained. They are useful itself for evaluating the Gruneisen parameters. The higher values observed for the larger diameters

suggest that they are more easily compressed than thinner ones, which agrees with the expected inverse to the diameter stability. Moreover, the presence of water inside the SWNTs whose diameters are larger than 1 nm lowered the pressure derivatives, whereas no significant difference was noticed for SWNTs having diameters smaller than 1 nm.

Simultaneous analysis of the pressure response of RBM and G-band concluded that SWNTs having diameters  $\sim 1.32 \pm 0.08$  nm undergo a collapsed phase  $\sim 3.8$  GPa. This value is consistent with theoretical predictions reported in literature for the 1.35 nm diameter, armchair (10,10) SWNT. Furthermore, water-filling of these SWNTs increased the collapse pressure to  $\sim 17.9$  GPa. This significant increasing suggests that water as filler provides excellent counter pressure support and therefore improves the mechanical stability.

At least for the given diameter distributions, this study bring some clarification about the pressure range for which empty SWNTs collapse. Several known values given by experiments are far overestimated in respect to the theoretical predictions. In this work, upon filling, the resulted collapse pressure is close to the experimental values previously assigned to empty SWNTs in literature. Since in this work empty and filled states are undoubtedly distinguished, it can be suggested that some previous studies reported collapse pressures for PTM-filled SWNTs instead of truly empty ones.

The present study also brings clarification on the behavior of the G-band frequency upon the collapse onset. By investigating empty and water-filled SWNT samples having two different diameter distributions, it can be suggested that during the collapse process, empty SWNTs show a leveling whilst filled SWNTs show inflection of the G-band frequency response to pressure.

Inserting the present work in literature contribute to clarify the roles of environment and filling on the pressure-stability. A comparison has found close values of collapse pressure for similar diameters while considering different PTM, suggesting that the environment is less influential than previously thought. Generally, the presence of filler content increase the collapse pressure of SWNTs and the homogeneity of filling boosts the increasing. Although, a precise experimental quantification on how the collapse pressure and the structural stability depend on the intrinsic parameters, namely diameter and chirality, it still depends on future investigations. As suggestion, high-pressure experiments must be carried on samples having SWNTs of a same chirality, or even on samples constituted of a individual SWNT.

## BIBLIOGRAPHY

- [1] S. IJIMA, "HELICAL MICROTUBULES OF GRAPHITIC CARBON," *NATURE*, vol. 354, pp. 56–58, NOV 7 1991. 1
- [2] M. Treacy, T. Ebbesen, and J. Gibson, "Exceptionally high Young's modulus observed for individual carbon nanotubes," *NATURE*, vol. 381, pp. 678–680, JUN 20 1996. 1
- [3] A. Krishnan, E. Dujardin, T. W. Ebbesen, P. N. Yianilos, and M. M. J. Treacy, "Young's modulus of single-walled nanotubes," *Phys. Rev. B*, vol. 58, pp. 14013–14019, Nov. 1998. 1
- [4] J. P. Lu, "Elastic properties of carbon nanotubes and nanoropes," *Phys. Rev. Lett.*, vol. 79, pp. 1297–1300, Aug. 1997. 1
- [5] M.-F. Yu, B. S. Files, S. Arepalli, and R. S. Ruoff, "Tensile loading of ropes of single wall carbon nanotubes and their mechanical properties," *Phys. Rev. Lett.*, vol. 84, pp. 5552–5555, June 2000. 1
- [6] M. Falvo, G. Clary, R. Taylor, V. Chi, F. Brooks, S. Washburn, and R. Superfine, "Bending and buckling of carbon nanotubes under large strain," *NATURE*, vol. 389, pp. 582–584, OCT 9 1997. 1
- [7] A. Kasumov, R. Deblock, M. Kociak, B. Reulet, H. Bouchiat, I. Khodos, Y. Gorbatov, V. Volkov, C. Journet, and M. Burghard, "Supercurrents through single-walled carbon nanotubes," *SCIENCE*, vol. 284, pp. 1508–1511, MAY 28 1999. 1
- [8] M. Dresselhaus, G. Dresselhaus, and A. Jorio, "Unusual properties and structure of carbon nanotubes," *Annual Review of Materials Research*, vol. 34, no. 1, pp. 247–278, 2004. 1
- [9] M. Chorro, G. Kan, L. Alvarez, J. Cambedouzou, E. Paineau, A. Rossberg, M. Kociak, R. Aznar, S. Pascarelli, P. Launois, and J. Bantignies, "1d-confinement of polyiodides inside single-wall carbon nanotubes," *Carbon*, vol. 52, no. 0, pp. 100–108, 2013. 1
- [10] S. Cambré, B. Schoeters, S. Luyckx, E. Goovaerts, and W. Wenseleers, "Experimental observation of single-file water filling of thin single-wall carbon nanotubes down to chiral index (5,3)," *Physical Review Letters*, vol. 104, p. 207401, May 2010. 1, 19, 29, 52

- [11] W. Wenseleers, S. Cambré, J. Čulín, A. Bouwen, and E. Goovaerts, “Effect of water filling on the electronic and vibrational resonances of carbon nanotubes: Characterizing tube opening by raman spectroscopy,” *Adv. Mater.*, vol. 19, p. 2274, Sept. 2007. 29
- [12] E. Paineau, P.-A. Albouy, S. Rouzire, A. Orecchini, S. Rols, and P. Launois, “X-ray scattering determination of the structure of water during carbon nanotube filling,” *Nano Letters*, vol. 13, no. 4, pp. 1751–1756, 2013. PMID: 23517435.
- [13] A. Alexiadis and S. Kassinos, “Influence of water model and nanotube rigidity on the density of water in carbon nanotubes,” *Chemical Engineering Science*, vol. 63, no. 10, pp. 2793–2797, 2008. 1, 52, 65
- [14] M. Chorro, A. Delhey, L. Noé, M. Monthieux, and P. Launois, “Orientation of  $c_{70}$  molecules in peapods as a function of the nanotube diameter,” *Phys. Rev. B*, vol. 75, p. 035416, Jan. 2007. 1
- [15] S. Rols, J. Cambedouzou, M. Chorro, H. Schober, V. Agafonov, P. Launois, V. Davydov, A. V. Rakhmanina, H. Kataura, and J.-L. Sauvajol, “How confinement affects the dynamics of  $c_{60}$  in carbon nanopeapods,” *Phys. Rev. Lett.*, vol. 101, p. 065507, Aug. 2008.
- [16] B. Verberck, J. Cambedouzou, G. Vliegthart, G. Gompfer, and P. Launois, “A monte carlo study of  $\{C_{70}\}$  molecular motion in  $c_{70}@swnt$  peapods,” *Carbon*, vol. 49, no. 6, pp. 2007–2021, 2011.
- [17] C. Bousige, S. Rols, E. Paineau, S. Rouzière, C. Mocuta, B. Verberck, J. P. Wright, H. Kataura, and P. Launois, “Progressive melting in confined one-dimensional  $c_{60}$  chains,” *Phys. Rev. B*, vol. 86, p. 045446, July 2012.
- [18] C. Bousige, S. Rols, H. Kataura, and P. Launois, “Translational dynamics of one-dimensional fullerene chains encapsulated inside single-walled carbon nanotubes,” *Fullerenes, Nanotubes and Carbon Nanostructures*, vol. 20, no. 4-7, pp. 395–400, 2012.
- [19] C. Bousige, S. Rols, E. Paineau, S. Rouzire, C. Mocuta, H. Kataura, and P. Launois, “In situ x-ray diffraction observation of two-step fullerene coalescence in carbon peapods,” *EPL (Europhysics Letters)*, vol. 103, no. 6, p. 66002, 2013.
- [20] C. Bousige, S. Rols, J. Ollivier, H. Schober, P. Fouquet, G. G. Simeoni, V. Agafonov, V. Davydov, Y. Niimi, K. Suenaga, H. Kataura, and P. Launois, “From a one-dimensional crystal to a one-dimensional liquid: A comprehensive dynamical study of  $c_{60}$  peapods,” *Phys. Rev. B*, vol. 87, p. 195438, May 2013. 1

- [21] S. Karmakar, S. Sharma, P. Teredesai, D. Muthu, A. Govindaraj, S. Sikka, and A. Sood, "Structural changes in single-walled carbon nanotubes under non-hydrostatic pressures: x-ray and raman studies," *New J. Phys.*, vol. 5, pp. 143.1–143.11, Oct. 2003. 1, 2, 22, 23, 63
- [22] C. Journet, S. Moulinet, C. Ybert, S. Purcell, and L. Bocquet, "Contact angle measurements on superhydrophobic carbon nanotube forests: Effect of fluid pressure," *EUROPHYSICS LETTERS*, vol. 71, pp. 104–109, JUL 2005. 1
- [23] K. Koga, G. Gao, H. Tanaka, and X. Zeng, "Formation of ordered ice nanotubes inside carbon nanotubes," *Nature*, vol. 412, no. 6849, pp. 802–805, 2001. 1, 52
- [24] Y. Gogotsi, J. Libera, A. Guvenc-Yazicioglu, and C. Megaridis, "In situ multi-phase fluid experiments in hydrothermal carbon nanotubes," *Applied Physics Letters*, vol. 79, no. 7, pp. 1021–1023, 2001.
- [25] R. Mashl, S. Joseph, N. Aluru, and E. Jakobsson, "Anomalously immobilized water: A new water phase induced by confinement in nanotubes," *Nano Letters*, vol. 3, no. 5, pp. 589–592, 2003. 52
- [26] J. Koefinger and C. Dellago, "Single-file water as a one-dimensional ising model," *New Journal of Physics*, vol. 12, 2010. 1, 52
- [27] L. Bocquet and E. Charlaix, "Nanofluidics, from bulk to interfaces," *Chemical Society Reviews*, vol. 39, no. 3, pp. 1073–1095, 2010. 1
- [28] G. Hummer, J. Rasaiah, and J. Noworyta, "Water conduction through the hydrophobic channel of a carbon nanotube," *Nature*, vol. 414, no. 6860, pp. 188–190, 2001. 1
- [29] K. Falk, F. Sedlmeier, L. Joly, R. R. Netz, and L. Bocquet, "Molecular origin of fast water transport in carbon nanotube membranes: Superlubricity versus curvature dependent friction," *Nano Letters*, vol. 10, no. 10, pp. 4067–4073, 2010. 1
- [30] A. Noy, H. G. Park, F. Fornasiero, J. K. Holt, C. P. Grigoropoulos, and O. Bakajin, "Nanofluidics in carbon nanotubes," *Nano Today*, vol. 2, pp. 22–29, Dec. 2007. 1
- [31] Y. Maniwa, K. Matsuda, H. Kyakuno, S. Ogasawara, T. Hibi, H. Kadowaki, S. Suzuki, Y. Achiba, and H. Kataura, "Water-filled single-wall carbon nanotubes as molecular nanovalves," *Nature Materials*, vol. 6, no. 2, pp. 135–141, 2007. 1

- [32] C. Dellago, M. Naor, and G. Hummer, “Proton transport through water-filled carbon nanotubes,” *Physical Review Letters*, vol. 90, no. 10, 2003. 1
- [33] Y. Zhao, L. Song, K. Deng, Z. Liu, Z. Zhang, Y. Yang, C. Wang, H. Yang, A. Jin, Q. Luo, C. Gu, S. Xie, and L. Sun, “Individual water-filled single-walled carbon nanotubes as hydroelectric power converters,” *Advanced Materials*, vol. 20, no. 9, pp. 1772+, 2008. 1
- [34] C. Liu, Y. Y. Fan, M. Liu, H. T. Cong, H. M. Cheng, and M. S. Dresselhaus, “Hydrogen storage in single-walled carbon nanotubes at room temperature,” *Science*, vol. 286, no. 5442, pp. 1127–1129, 1999. 1
- [35] Y. Wu and G.-Y. Kim, “Carbon nanotube reinforced aluminum composite fabricated by semi-solid powder processing,” *Journal of Materials Processing Technology*, vol. 211, no. 8, pp. 1341–1347, 2011. 1
- [36] M. Majid, G. Majzoubi, G. Noozad, A. Reihani, S. Mortazavi, and M. Gorji, “Fabrication and mechanical properties of mwcnts-reinforced aluminum composites by hot extrusion,” *Rare Metals*, vol. 31, no. 4, pp. 372–378, 2012. 1
- [37] B. Vigolo, P. Poulin, M. Lucas, P. Launois, and P. Bernier, “Improved structure and properties of single-wall carbon nanotube spun fibers,” *Applied Physics Letters*, vol. 81, no. 7, pp. 1210–1212, 2002. 1
- [38] V. Pichot, S. Badaire, P. A. Albouy, C. Zakri, P. Poulin, and P. Launois, “Structural and mechanical properties of single-wall carbon nanotube fibers,” *Phys. Rev. B*, vol. 74, p. 245416, Dec. 2006.
- [39] M. Motta, A. Moisala, I. Kinloch, and A. Windle, “High performance fibres from dog bone carbon nanotubes,” *Advanced Materials*, vol. 19, no. 21, pp. 3721–3726, 2007. 1, 21, 22
- [40] M. M. Shulaker, G. Hills, N. Patil, H. Wei, H.-Y. Chen, H. S. PhilipWong, and S. Mitra, “Carbon nanotube computer,” *NATURE*, vol. 501, pp. 526+, SEP 26 2013. 1
- [41] A. Bozhko, D. Sklovsky, V. Nalimova, A. Rinzler, R. Smalley, and J. Fischer, “Resistance vs. pressure of single-wall carbon nanotubes,” *APPLIED PHYSICS A-MATERIALS SCIENCE & PROCESSING*, vol. 67, pp. 75–77, JUL 1998. 1
- [42] R. B. Capaz, C. D. Spataru, P. Tangney, M. L. Cohen, and S. G. Louie, “Hydrostatic pressure effects on the structural and electronic properties of carbon nanotubes,”

- Physica Status Solidi B: Basic Solid State Physics*, vol. 241, no. 14, pp. 3352–3359, 2004. 1, 27, 48
- [43] V. Perebeinos and J. Tersoff, “Carbon nanotube deformation and collapse under metal contacts,” *Nano Letters*, vol. 14, no. 8, pp. 4376–4380, 2014. PMID: 25014612. 1
- [44] Y. Zhang, J. Zhang, H. Son, J. Kong, and Z. Liu, “Substrate-induced Raman frequency variation for single-walled carbon nanotubes,” *JOURNAL OF THE AMERICAN CHEMICAL SOCIETY*, vol. 127, pp. 17156–17157, DEC 14 2005. 1, 21
- [45] C. Caillier, A. Ayari, V. Gouttenoire, J.-M. Benoit, V. Jourdain, M. Picher, M. Paillet, S. Le Floch, S. T. Purcell, J.-L. Sauvajol, and A. San Miguel, “An Individual Carbon Nanotube Transistor Tuned by High Pressure,” *ADVANCED FUNCTIONAL MATERIALS*, vol. 20, pp. 3330–3335, OCT 8 2010. 1
- [46] A. Jayaraman, “Diamond anvil cell and high-pressure physical investigations,” *Rev. Mod. Phys.*, vol. 55, pp. 65–108, Jan. 1983. 2
- [47] B. Anis, K. Haubner, F. Börrnert, L. Dunsch, M. H. Rümmeli, and C. A. Kuntscher, “Stabilization of carbon nanotubes by filling with inner tubes: An optical spectroscopy study on double-walled carbon nanotubes under hydrostatic pressure,” *Phys. Rev. B*, vol. 86, p. 155454, Oct. 2012. 2, 24
- [48] R. S. Deacon, K.-C. Chuang, J. Doig, I. B. Mortimer, and R. J. Nicholas, “Photoluminescence study of aqueous-surfactant-wrapped single-walled carbon nanotubes under hydrostatic pressure,” *Phys. Rev. B*, vol. 74, p. 201402, Nov. 2006. 2, 27
- [49] A. Sood, P. Teresdesai, D. Muthu, R. Sen, A. Govindaraj, and C. Rao, “Pressure behaviour of single wall carbon nanotube bundles and fullerenes: A Raman study,” *PHYSICA STATUS SOLIDI B-BASIC RESEARCH*, vol. 215, pp. 393–401, SEP 1999. International Conference on Solid State Spectroscopy - (ICSSS), SCHWABISCH-GMUND, GERMANY, SEP 05-07, 1999. 2, 22
- [50] A. J. Ghandour, A. Sapelkin, I. Hernandez, D. J. Dunstan, I. F. Crowe, and M. P. Halsall, “Raman excitation spectroscopy of carbon nanotubes: effects of pressure medium and pressure,” *High Pressure Research*, vol. 32, no. 1, pp. 67–71, 2012. 49th Conference of the European High Pressure Research Group (EHPRG), Budapest, HUNGARY, AUG 28-SEP 02, 2011. 2, 24
- [51] A. L. Aguiar, E. B. Barros, R. B. Capaz, A. G. Souza Filho, P. T. C. Freire, J. Mendes Filho, D. Machon, C. Caillier, Y. A. Kim, H. Muramatsu, M. Endo, and

- A. San-Miguel, "Pressure-induced collapse in double-walled carbon nanotubes: Chemical and mechanical screening effects," *J. Phys. Chem. C*, vol. 115, pp. 5378–5384, Apr. 2011. 23, 24, 25, 70
- [52] L. Alvarez, J.-L. Bantignies, R. Le Parc, R. Aznar, J.-L. Sauvajol, A. Merlen, D. Machon, and A. San Miguel, "High-pressure behavior of polyiodides confined into single-walled carbon nanotubes: A raman study," *Phys. Rev. B*, vol. 82, p. 205403, Nov. 2010. 23, 25, 70
- [53] C. Caillier, D. Machon, A. San-Miguel, R. Arenal, G. Montagnac, H. Cardon, M. Kalbac, M. Zukalova, and L. Kavan, "Probing high-pressure properties of single-wall carbon nanotubes through fullerene encapsulation," *Phys. Rev. B*, vol. 77, p. 125418, Mar. 2008. 23, 25, 67, 69, 70
- [54] A. Merlen, P. Toulemonde, N. Bendiab, A. Aouizerat, J. Sauvajol, G. Montagnac, H. Cardon, P. Petit, and A. San Miguel, "Raman spectroscopy of open-ended single wall carbon nanotubes under pressure: effect of the pressure transmitting medium," *Physica Status Solidi B-Basic Solid State Physics*, vol. 243, no. 3, pp. 690–699, 2006. 2, 22, 25, 26, 58, 63, 69, 70
- [55] J. A. Elliott, J. K. W. Sandler, A. H. Windle, R. J. Young, and M. S. P. Shaffer, "Collapse of single-wall carbon nanotubes is diameter dependent," *Physical Review Letters*, vol. 92, p. 095501, Mar. 2004. 2, 21, 24
- [56] C.-C. Ling, Q.-Z. Xue, L.-Y. Chu, N.-N. Jing, and X.-Y. Zhou, "Radial collapse of carbon nanotubes without and with stone-wales defects under hydrostatic pressure," *RSC Adv.*, vol. 2, pp. 12182–12189, 2012. 2, 26, 49
- [57] J. Frey and D. Doren, "Tubtube 3.2," 2003. 4, 6, 7
- [58] K. Momma and F. Izumi, "VESTA3 for three-dimensional visualization of crystal, volumetric and morphology data," *Journal of Applied Crystallography*, vol. 44, pp. 1272–1276, Dec. 2011. 4, 6, 7
- [59] A. H. Castro Neto, F. Guinea, N. M. R. Peres, K. S. Novoselov, and A. K. Geim, "The electronic properties of graphene," *Rev. Mod. Phys.*, vol. 81, pp. 109–162, Jan. 2009. 5
- [60] R. Saito, G. Dresselhaus, and M. S. Dresselhaus, *Physical Properties of Carbon Nanotubes*. Imperial College Press, 1998. 4, 6, 16

- [61] M. Dresselhaus, G. Dresselhaus, R. Saito, and A. Jorio, "Raman spectroscopy of carbon nanotubes," *Physics Reports*, vol. 409, no. 2, pp. 47–99, 2005. 6, 19
- [62] G. Samsonidze, R. Saito, A. Jorio, M. Pimenta, A. Souza, A. Gruneis, G. Dresselhaus, and M. Dresselhaus, "The concept of cutting lines in carbon nanotube science," *Journal of Nanoscience and Nanotechnology*, vol. 3, no. 6, pp. 431–458, 2003. 8
- [63] M. Cardona and R. Merlin, "Light scattering in solids ix," in *Light Scattering in Solid IX* (M. Cardona and R. Merlin, eds.), vol. 108 of *Topics in Applied Physics*, pp. 1–14, Springer Berlin Heidelberg, 2007. 9
- [64] D. A. Long, *The Raman Effect*. John Wiley Sons LTD, 2002. 10
- [65] E. Le Ru and P. Etchegoin, *Pinciples of Surface Enhanced Raman Spectroscopy and related plasmonic effects*. Elsevier, 2009. 12, 13
- [66] H. Mao, J. Xu, and P. Bell, "Calibration of the ruby pressure gauge to 800-kbar under quasi-hydrostatic conditions," *Journal of Geophysical Research*, vol. 91, pp. 4673–4676, Apr. 1986. 14
- [67] B. Weinstein and R. Zallen, "Pressure-raman effects in covalent and molecular solids," in *Light Scattering in Solids IV* (M. Cardona and G. Gntherodt, eds.), vol. 54 of *Topics in Applied Physics*, pp. 463–527, Springer Berlin Heidelberg, 1984. 15
- [68] M. Wojdyr, "*Fityk*: a general-purpose peak fitting program," *Journal of Applied Crystallography*, vol. 43, pp. 1126–1128, Oct. 2010. 16
- [69] J.-L. Bantignies, J.-L. Sauvajol, A. Rahmani, and E. Flahaut, "Infrared-active phonons in carbon nanotubes," *Phys. Rev. B*, vol. 74, p. 195425, Nov. 2006. 16
- [70] K. Sbai, A. Rahmani, H. Chadli, J.-L. Bantignies, P. Hermet, and J.-L. Sauvajol, "Infrared spectroscopy of single-walled carbon nanotubes," *The Journal of Physical Chemistry B*, vol. 110, no. 25, pp. 12388–12393, 2006. PMID: 16800564. 16
- [71] A. Jorio, G. Dresselhaus, M. S. Dresselhaus, M. Souza, M. S. S. Dantas, M. A. Pimenta, A. M. Rao, R. Saito, C. Liu, and H. M. Cheng, "Polarized raman study of single-wall semiconducting carbon nanotubes," *Physical Review Letters*, vol. 85, pp. 2617–2620, Sept. 2000. 16
- [72] S. Reich, C. Thomsen, and P. Ordejón, "Phonon eigenvectors of chiral nanotubes," *Phys. Rev. B*, vol. 64, p. 195416, Oct. 2001.

- [73] A. Jorio, A. G. Souza Filho, G. Dresselhaus, M. S. Dresselhaus, A. K. Swan, M. S. Ünlü, B. B. Goldberg, M. A. Pimenta, J. H. Hafner, C. M. Lieber, and R. Saito, “G-band resonant raman study of 62 isolated single-wall carbon nanotubes,” *Phys. Rev. B*, vol. 65, p. 155412, Mar. 2002. 16, 17, 18, 19, 20, 34
- [74] S. Piscanec, M. Lazzeri, J. Robertson, A. C. Ferrari, and F. Mauri, “Optical phonons in carbon nanotubes: Kohn anomalies, peierls distortions, and dynamic effects,” *Phys. Rev. B*, vol. 75, p. 035427, Jan. 2007. 16
- [75] H. Telg, J. G. Duque, M. Staiger, X. Tu, F. Hennrich, M. M. Kappes, M. Zheng, J. Maultzsch, C. Thomsen, and S. K. Doorn, “Chiral index dependence of the g+ and g raman modes in semiconducting carbon nanotubes,” *ACS Nano*, vol. 6, no. 1, pp. 904–911, 2012. 16
- [76] A. R. T. Nugraha, R. Saito, K. Sato, P. T. Araujo, A. Jorio, and M. S. Dresselhaus, “Dielectric constant model for environmental effects on the exciton energies of single wall carbon nanotubes,” *Applied Physics Letters*, vol. 97, no. 9, pp. –, 2010. 18
- [77] C. Journet, W. Maser, P. Bernier, A. Loiseau, M. delaChapelle, S. Lefrant, P. Deniard, R. Lee, and J. Fischer, “Large-scale production of single-walled carbon nanotubes by the electric-arc technique,” *NATURE*, vol. 388, pp. 756–758, AUG 21 1997. 17, 28, 32
- [78] W. Wenseleers, I. Vlasov, E. Goovaerts, E. Obraztsova, A. Lobach, and A. Bouwen, “Efficient isolation and solubilization of pristine single-walled nanotubes in bile salt micelles,” *Advanced Functional Materials*, vol. 14, pp. 1105–1112, Nov. 2004. 17, 26, 29
- [79] S. Cambré and W. Wenseleers, “Separation and diameter-sorting of empty (end-capped) and water-filled (open) carbon nanotubes by density gradient ultracentrifugation,” *Angewandte Chemie, International Edition*, vol. 123, no. 12, p. 2816, 2011. 17, 26, 29
- [80] A. Jorio, C. Fantini, M. S. S. Dantas, M. A. Pimenta, A. G. Souza Filho, G. G. Samsonidze, V. W. Brar, G. Dresselhaus, M. S. Dresselhaus, A. K. Swan, M. S. Ünlü, B. B. Goldberg, and R. Saito, “Linewidth of the raman features of individual single-wall carbon nanotubes,” *Phys. Rev. B*, vol. 66, p. 115411, Sept. 2002. 17
- [81] S. Brown, A. Jorio, P. Corio, M. Dresselhaus, G. Dresselhaus, R. Saito, and K. Kneipp, “Origin of the Breit-Wigner-Fano lineshape of the tangential G-band feature of metallic carbon nanotubes,” *PHYSICAL REVIEW B*, vol. 63, APR 15 2001. 18, 20

- [82] M. Paillet, P. Poncharal, A. Zahab, J.-L. Sauvajol, J. C. Meyer, and S. Roth, “Vanishing of the breit-wigner-fano component in individual single-wall carbon nanotubes,” *Phys. Rev. Lett.*, vol. 94, p. 237401, June 2005. 18, 35
- [83] M. Paillet, T. Michel, J. C. Meyer, V. N. Popov, L. Henrard, S. Roth, and J.-L. Sauvajol, “Raman active phonons of identified semiconducting single-walled carbon nanotubes,” *Physical Review Letters*, vol. 96, p. 257401, June 2006. 18
- [84] S. Lebedkin, K. Arnold, O. Kiowski, F. Hennrich, and M. M. Kappes, “Raman study of individually dispersed single-walled carbon nanotubes under pressure,” *Phys. Rev. B*, vol. 73, p. 094109, Mar. 2006. 19, 22, 26, 27, 50, 64
- [85] M. Milnera, J. Kürti, M. Hulman, and H. Kuzmany, “Periodic resonance excitation and intertube interaction from quasicontinuous distributed helicities in single-wall carbon nanotubes,” *Physical Review Letters*, vol. 84, pp. 1324–1327, Feb. 2000. 19
- [86] A. Jorio, M. A. Pimenta, A. G. S. Filho, R. Saito, G. Dresselhaus, and M. S. Dresselhaus, “Characterizing carbon nanotube samples with resonance raman scattering,” *New Journal of Physics*, vol. 5, no. 1, p. 139, 2003. 19, 20
- [87] P. T. Araujo, I. O. Maciel, P. B. C. Pesce, M. A. Pimenta, S. K. Doorn, H. Qian, A. Hartschuh, M. Steiner, L. Grigorian, K. Hata, and A. Jorio, “Nature of the constant factor in the relation between radial breathing mode frequency and tube diameter for single-wall carbon nanotubes,” *Physical Review B*, vol. 77, no. 24, 2008. 19
- [88] A. Jorio, R. Saito, J. H. Hafner, C. M. Lieber, M. Hunter, T. McClure, G. Dresselhaus, and M. S. Dresselhaus, “Structural ( n, m) determination of isolated single-wall carbon nanotubes by resonant raman scattering,” *Physical Review Letters*, vol. 86, pp. 1118–1121, Feb. 2001. 19
- [89] A. Jorio, M. A. Pimenta, A. G. Souza Filho, G. G. Samsonidze, A. K. Swan, M. S. Ünlü, B. B. Goldberg, R. Saito, G. Dresselhaus, and M. S. Dresselhaus, “Resonance raman spectra of carbon nanotubes by cross-polarized light,” *Physical Review Letters*, vol. 90, p. 107403, Mar. 2003. 19
- [90] A. Jorio, C. Fantini, M. A. Pimenta, R. B. Capaz, G. G. Samsonidze, G. Dresselhaus, M. S. Dresselhaus, J. Jiang, N. Kobayashi, A. Grüneis, and R. Saito, “Resonance raman spectroscopy (n,m)-dependent effects in small-diameter single-wall carbon nanotubes,” *Phys. Rev. B*, vol. 71, p. 075401, Feb. 2005. 19

- [91] S. Bachilo, M. Strano, C. Kittrell, R. Hauge, R. Smalley, and R. Weisman, "Structure-assigned optical spectra of single-walled carbon nanotubes," *Science*, vol. 298, pp. 2361–2366, Dec. 2002. 19
- [92] R. RUOFF, J. TERSOFF, D. LORENTS, S. SUBRAMONEY, and B. CHAN, "RADIAL DEFORMATION OF CARBON NANOTUBES BY VAN-DER-WAALS FORCES," *NATURE*, vol. 364, pp. 514–516, AUG 5 1993. 20
- [93] C. Thomsen, S. Reich, A. R. Goi, H. Jantoljak, P. M. Rafailov, I. Loa, K. Syassen, C. Journet, and P. Bernier, "Intermolecular interaction in carbon nanotube ropes," *physica status solidi (b)*, vol. 215, no. 1, pp. 435–441, 1999. 20, 22
- [94] J. Tang, L.-C. Qin, T. Sasaki, M. Yudasaka, A. Matsushita, and S. Iijima, "Compressibility and polygonization of single-walled carbon nanotubes under hydrostatic pressure," *Physical Review Letters*, vol. 85, pp. 1887–1889, Aug. 2000. 20
- [95] S. M. Sharma, S. Karmakar, S. K. Sikka, P. V. Teredesai, A. K. Sood, A. Govindaraj, and C. N. R. Rao, "Pressure-induced phase transformation and structural resilience of single-wall carbon nanotube bundles," *Phys. Rev. B*, vol. 63, p. 205417, May 2001. 21
- [96] S. Rols, I. N. Goncharenko, R. Almairac, J. L. Sauvajol, and I. Mirebeau, "Polygonization of single-wall carbon nanotube bundles under high pressure," *Phys. Rev. B*, vol. 64, p. 153401, Sept. 2001. 21
- [97] S. Reich, H. Jantoljak, and C. Thomsen, "Shear strain in carbon nanotubes under hydrostatic pressure," *Phys. Rev. B*, vol. 61, pp. R13389–R13392, May 2000. 21
- [98] C. Q. Ru, "Elastic buckling of single-walled carbon nanotube ropes under high pressure," *Phys. Rev. B*, vol. 62, pp. 10405–10408, Oct. 2000. 21
- [99] S.-P. Chan, W.-L. Yim, X. G. Gong, and Z.-F. Liu, "Carbon nanotube bundles under high pressure: transformation to low-symmetry structures," *Phys. Rev. B*, vol. 68, p. 075404, Aug. 2003. 21
- [100] S. Reich, C. Thomsen, and P. Ordejón, "Elastic properties and pressure-induced phase transitions of single-walled carbon nanotubes," *physica status solidi (b)*, vol. 235, no. 2, pp. 354–359, 2003.
- [101] X. Yang, G. Wu, and J. Dong, "Structural transformations of double-walled carbon nanotube bundle under hydrostatic pressure," *Applied Physics Letters*, vol. 89, no. 11, pp. –, 2006. 21

- [102] P. Tangney, R. B. Capaz, C. D. Spataru, M. L. Cohen, and S. G. Louie, “Structural transformations of carbon nanotubes under hydrostatic pressure,” *Nano Letters*, vol. 5, no. 11, pp. 2268–2273, 2005. 21
- [103] A. San-Miguel, “Nanomaterials under high-pressure,” *Chemical Society Reviews*, vol. 35, pp. 876–889, 2006. 21
- [104] U. D. Venkateswaran, D. L. Masica, G. U. Sumanasekara, C. A. Furtado, U. J. Kim, and P. C. Eklund, “Diameter dependent wall deformations during the compression of a carbon nanotube bundle,” *Phys. Rev. B*, vol. 68, p. 241406, Dec. 2003. 21, 22, 54
- [105] T. Tang, A. Jagota, C.-Y. Hui, and N. J. Glassmaker, “Collapse of single-walled carbon nanotubes,” *Journal of Applied Physics*, vol. 97, no. 7, pp. –, 2005.
- [106] V. Gadagkar, P. K. Maiti, Y. Lansac, A. Jagota, and A. K. Sood, “Collapse of double-walled carbon nanotube bundles under hydrostatic pressure,” *Phys. Rev. B*, vol. 73, p. 085402, Feb. 2006. 21
- [107] T. F. T. Cerqueira, S. Botti, A. San-Miguel, and M. A. L. Marques *Carbon*, vol. 69, pp. 355–360, 2014. 21
- [108] J. Xiao, B. Liu, Y. Huang, J. Zuo, K.-C. Hwang, and M.-F. Yu, “Collapse and stability of single-and multi-wall carbon nanotubes,” *Nanotechnology*, vol. 18, no. 39, p. 395703, 2007. 21
- [109] K. Yan, Q. Xue, Q. Zheng, D. Xia, H. Chen, and J. Xie, “Radial collapse of single-walled carbon nanotubes induced by the cu<sub>2</sub>o surface,” *The Journal of Physical Chemistry C*, vol. 113, no. 8, pp. 3120–3126, 2009. 21
- [110] E. D. Obraztsova, H. T. Lotz, J. A. Schouten, M. E. Kooi, A. V. Osadchy, V. L. Kuznetsov, and V. I. Zaikovskii, “In situ raman investigations of single-wall carbon nanotubes pressurized in diamond anvil cell,” *AIP Conference Proceedings*, vol. 486, no. 1, pp. 333–337, 1999. 22
- [111] M. J. Peters, L. E. McNeil, J. P. Lu, and D. Kahn, “Structural phase transition in carbon nanotube bundles under pressure,” *Phys. Rev. B*, vol. 61, pp. 5939–5944, Mar. 2000. 22
- [112] U. D. Venkateswaran, A. M. Rao, E. Richter, M. Menon, A. Rinzler, R. E. Smalley, and P. C. Eklund, “Probing the single-wall carbon nanotube bundle: Raman scattering under high pressure,” *Phys. Rev. B*, vol. 59, pp. 10928–10934, Apr. 1999. 22, 53

- [113] U. Venkateswaran, E. Brandsen, U. Schlecht, A. Rao, E. Richter, I. Loa, K. Syassen, and P. Eklund, “High pressure studies of the raman-active phonons in carbon nanotubes,” *Physica Status Solidi B: Basic Solid State Physics*, vol. 223, no. 1, pp. 225–236, 2001. 22
- [114] J. Sandler, M. S. P. Shaffer, A. H. Windle, M. P. Halsall, M. A. Montes-Morán, C. A. Cooper, and R. J. Young, “Variations in the raman peak shift as a function of hydrostatic pressure for various carbon nanostructures: A simple geometric effect,” *Phys. Rev. B*, vol. 67, p. 035417, Jan. 2003. 22
- [115] U. Schlecht, U. Venkateswaran, E. Richter, J. Chen, R. Haddon, P. Eklund, and A. Rao, “High-pressure Raman study of debundled single-walled carbon nanotubes,” *JOURNAL OF NANOSCIENCE AND NANOTECHNOLOGY*, vol. 3, pp. 139–143, FEB-APR 2003. 22
- [116] C. Thomsen, S. Reich, H. Jantoljak, I. Loa, K. Syassen, M. Burghard, G. Duesberg, and S. Roth, “Raman spectroscopy on single- and multi-walled nanotubes under high pressure,” *Applied Physics A*, vol. 69, no. 3, pp. 309–312, 1999. 22
- [117] P. V. Teredesai, A. Sood, D. Muthu, R. Sen, A. Govindaraj, and C. Rao, “Pressure-induced reversible transformation in single-wall carbon nanotube bundles studied by raman spectroscopy,” *Chemical Physics Letters*, vol. 319, no. 34, pp. 296–302, 2000.
- [118] A. Merlen, N. Bendiab, P. Toulemonde, A. Aouizerat, A. San Miguel, J. L. Sauvajol, G. Montagnac, H. Cardon, and P. Petit, “Resonant raman spectroscopy of single-wall carbon nanotubes under pressure,” *Phys. Rev. B*, vol. 72, p. 035409, July 2005. 22, 51, 53, 62, 69
- [119] J. E. Proctor, M. P. Halsall, A. Ghandour, and D. J. Dunstan, “High pressure raman spectroscopy of single-walled carbon nanotubes: Effect of chemical environment on individual nanotubes and the nanotube bundle,” *Journal of Physics and Chemistry of Solids*, vol. 67, no. 12, pp. 2468–2472, 2006. 64
- [120] A. J. Ghandour, D. J. Dunstan, A. Sapelkin, J. E. Proctor, and M. P. Halsall, “High-pressure Raman response of single-walled carbon nanotubes: Effect of the excitation laser energy,” *PHYSICAL REVIEW B*, vol. 78, SEP 2008. 34, 63
- [121] A. J. Ghandour, D. J. Dunstan, A. Sapelkin, I. Hernandez, M. P. Halsall, and I. F. Crowe, “Effect of water on resonant raman spectroscopy of closed single-walled carbon nanotubes,” *physica status solidi (b)*, vol. 248, no. 11, pp. 2548–2551, 2011.

- [122] A. J. Ghandour, D. J. Dunstan, and A. Sapelkin, “Raman g-mode of single-wall carbon nanotube bundles under pressure,” *Journal of Raman Spectroscopy*, vol. 42, no. 8, pp. 1611–1613, 2011. 22
- [123] U. D. Venkateswaran, M.-. Gosselin, B. Postek, D. L. Masica, G. Chen, R. Gupta, and P. C. Eklund, “Radial and tangential vibrational modes of hipco-derived carbon nanotubes under pressure,” *physica status solidi (b)*, vol. 235, no. 2, pp. 364–368, 2003. 22, 26
- [124] M. Yao, Z. Wang, B. Liu, Y. Zou, S. Yu, W. Lin, Y. Hou, S. Pan, M. Jin, B. Zou, T. Cui, G. Zou, and B. Sundqvist, “Raman signature to identify the structural transition of single-wall carbon nanotubes under high pressure,” *Phys. Rev. B*, vol. 78, p. 205411, Nov. 2008. 23, 24, 66, 69
- [125] D. Christofilos, J. Arvanitidis, E. Efthimiopoulos, X. Zhao, Y. Ando, T. Takenobu, Y. Iwasa, H. Kataura, S. Ves, and G. A. Kourouklis, “High pressure raman studies of carbon nanotube materials,” *Journal of Physics: Conference Series*, vol. 121, no. 16, p. 162003, 2008.
- [126] A. J. Ghandour, I. F. Crowe, J. E. Proctor, Y. W. Sun, M. P. Halsall, I. Hernandez, A. Sapelkin, and D. J. Dunstan, “Pressure coefficients of raman modes of carbon nanotubes resolved by chirality: Environmental effect on graphene sheet,” *Phys. Rev. B*, vol. 87, p. 085416, 2013. 22, 26, 53
- [127] Y. Sun, I. Hernandez, A. Ghandour, C. Rice, I. Crowe, M. Halsall, A. Sapelkin, J. Gonzalez, F. Rodriguez, and D. Dunstan, “Resonance raman spectroscopy of carbon nanotubes: pressure effects on g-mode,” *High Pressure Research*, vol. 34, no. 2, pp. 191–197, 2014. 22, 25
- [128] S. Kawasaki, Y. Matsuoka, T. Yokomae, Y. Nojima, F. Okino, H. Touhara, and H. Kataura, “Effect of a liquid pressure-transmitting medium on the high pressure behavior of open- and closed-end single-walled carbon nanotubes and of c60-peapods,” *physica status solidi (b)*, vol. 241, no. 15, pp. 3512–3516, 2004. 22, 25
- [129] M. Hanfland, H. Beister, and K. Syassen, “Graphite under pressure: Equation of state and first-order raman modes,” *Phys. Rev. B*, vol. 39, no. 17, pp. 12598–12603, 1989. 25, 53, 65
- [130] B. Anis, F. Boerrnert, M. H. Ruemmeli, and C. A. Kuntscher, “High-Pressure Optical Microspectroscopy Study on Single-Walled Carbon Nanotubes Encapsulating C-60,”

- JOURNAL OF PHYSICAL CHEMISTRY C*, vol. 117, pp. 21995–22001, OCT 24 2013. 24, 70
- [131] D. Christofilos, J. Arvanitidis, E. Efthimiopoulos, X. Zhao, Y. Ando, T. Takenobu, Y. Iwasa, H. Kataura, S. Ves, and G. A. Kourouklis, “Tube encapsulation effects in various carbon nanotube systems,” *Physica Status Solidi B: Basic Solid State Physics*, vol. 244, no. 11, pp. 4082–4085, 2007. 24
- [132] B. Anis, F. Boerrnert, M. H. Ruemmeli, and C. A. Kuntscher, “Role of the pressure transmitting medium on the pressure effects in DWCNTs,” *PHYSICA STATUS SOLIDI B-BASIC SOLID STATE PHYSICS*, vol. 250, pp. 2616–2621, DEC 2013. 25
- [133] A. Abouelsayed, K. Thirunavukkuarasu, F. Hennrich, and C. A. Kuntscher, “Role of the pressure transmitting medium for the pressure effects in single-walled carbon nanotubes,” *The Journal of Physical Chemistry C*, vol. 114, no. 10, pp. 4424–4428, 2010. 25
- [134] A. L. Aguiar, R. B. Capaz, A. G. Souza Filho, and A. San-Miguel, “Structural and phonon properties of bundled single- and double-wall carbon nanotubes under pressure,” *J. Phys. Chem. C*, vol. 116, no. 42, pp. 22637–22645, 2012. 25
- [135] M. H. F. Sluiter and Y. Kawazoe, “Phase diagram of single-wall carbon nanotube crystals under hydrostatic pressure,” *Phys. Rev. B*, vol. 69, p. 224111, June 2004. 26
- [136] D. J. Dunstan and A. J. Ghandour, “High-pressure studies of carbon nanotubes,” *HIGH PRESSURE RESEARCH*, vol. 29, no. 4, pp. 548–553, 2009. 47th Meeting of the European-High-Pressure-Research-Group (EHPRG 47), Univ Pierre & Marie Curie, Cordeliers Campus, Paris, FRANCE, SEP 06-11, 2009. 27, 28, 48, 61
- [137] M. Mases, V. V. Milyavskiy, J. Waldbock, M. Dossot, X. Devaux, E. McRae, and A. V. Soldatov, “The effect of shock wave compression on double wall carbon nanotubes,” *Physica Status Solidi B: Basic Solid State Physics*, vol. 249, no. 12, 2012. 27
- [138] R. S. Alencar, A. L. Aguiar, A. R. Paschoal, P. T. C. Freire, Y. A. Kim, H. Muramatsu, M. Endo, H. Terrones, M. Terrones, A. San-Miguel, M. S. Dresselhaus, and A. G. Souza Filho, “Pressure-Induced Selectivity for Probing Inner Tubes in Double- and Triple-Walled Carbon Nanotubes: A Resonance Raman Study,” *JOURNAL OF PHYSICAL CHEMISTRY C*, vol. 118, pp. 8153–8158, APR 17 2014. 28
- [139] M. Bronikowski, P. A. Willis, D. T. Colbert, K. A. Smith, and R. E. Smalley, “Gas-phase production of carbon single-walled nanotubes from carbon monoxide via the

- hipco process: A parametric study,” *J. Vac. Sci. Technol. A*, vol. 19, pp. 1800–1805, 2001. 28
- [140] P. Nikolaev, M. Bronikowski, R. Bradley, F. Rohmund, D. Colbert, K. Smith, and R. Smalley, “Gas-phase catalytic growth of single-walled carbon nanotubes from carbon monoxide,” *CHEMICAL PHYSICS LETTERS*, vol. 313, pp. 91–97, NOV 5 1999. 28
- [141] A. Rinzler, J. Liu, H. Dai, P. Nikolaev, C. Huffman, F. Rodriguez-Macias, P. Boul, A. Lu, D. Heymann, D. Colbert, R. Lee, J. Fischer, A. Rao, P. Eklund, and R. Smalley, “Large-scale purification of single-wall carbon nanotubes: process, product, and characterization,” *APPLIED PHYSICS A-MATERIALS SCIENCE & PROCESSING*, vol. 67, pp. 29–37, JUL 1998. 28
- [142] C. Bower, S. Suzuki, K. Tanigaki, and O. Zhou, “Synthesis and structure of pristine and alkali-metal-intercalated single-walled carbon nanotubes,” *APPLIED PHYSICS A-MATERIALS SCIENCE & PROCESSING*, vol. 67, pp. 47–52, JUL 1998. 28
- [143] A. Thess, R. Lee, P. Nikolaev, H. Dai, P. Petit, J. Robert, C. Xu, Y. H. Lee, S. G. Kim, A. G. Rinzler, D. T. Colbert, G. E. Scuseria, D. Tomnek, J. E. Fischer, and R. E. Smalley, “Crystalline ropes of metallic carbon nanotubes,” *Science*, vol. 273, no. 5274, pp. 483–487, 1996. 28
- [144] J. Richard and P. Wallis, “Manufacturing, characterization and use of single walled carbon nanotubes,” *Material Matters*, vol. 4, p. 23, 2009. 28
- [145] R. B. Weisman and S. M. Bachilo, “Dependence of optical transition energies on structure for single-walled carbon nanotubes in aqueous suspension: an empirical katura plot,” *Nano Letters*, vol. 3, no. 9, pp. 1235–1238, 2003. 31
- [146] H. Liang and M. Upmanyu, “Axial-strain-induced torsion in single-walled carbon nanotubes,” *Physical Review Letters*, vol. 96, p. 165501, Apr. 2006. 51
- [147] D. G. Vercosa, E. B. Barros, A. G. Souza Filho, J. Mendes Filho, G. G. Samsonidze, R. Saito, and M. S. Dresselhaus, “Torsional instability of chiral carbon nanotubes,” *Phys. Rev. B*, vol. 81, p. 165430, Apr. 2010. 51
- [148] J. Wang, Y. Zhu, J. Zhou, and X. Lu, “Diameter and helicity effects on static properties of water molecules confined in carbon nanotubes,” *Physical Chemistry Chemical Physics*, vol. 6, no. 4, pp. 829–835, 2004. 52

- 
- [149] A. Alexiadis and S. Kassinos, “Molecular simulation of water in carbon nanotubes,” *Chemical Reviews*, vol. 108, no. 12, pp. 5014–5034, 2008. 52
- [150] A. Alexiadis and S. Kassinos, “The density of water in carbon nanotubes,” *Chemical Engineering Science*, vol. 63, no. 8, pp. 2047–2056, 2008. 52
- [151] O. Byl, J.-C. Liu, Y. Wang, W.-L. Yim, J. K. Johnson, and J. J. T. Yates, “Unusual hydrogen bonding in water-filled carbon nanotubes,” *Journal of the American Chemical Society*, vol. 128, no. 37, pp. 12090–12097, 2006. 52
- [152] A. Berezhkovskii and G. Hummer, “Single-file transport of water molecules through a carbon nanotube,” *Physical Review Letters*, vol. 89, no. 6, 2002. 52
- [153] A. Waghe, J. Rasaiah, and G. Hummer, “Filling and emptying kinetics of carbon nanotubes in water,” *Journal of Chemical Physics*, vol. 117, no. 23, pp. 10789–10795, 2002. 52
- [154] Y. Maniwa, H. Kataura, M. Abe, S. Suzuki, Y. Achiba, H. Kira, and K. Matsuda, “Phase transition in confined water inside carbon nanotubes,” *Journal of the Physical Society of Japan*, vol. 71, no. 12, pp. 2863–2866, 2002. 52
- [155] C. Luo, W. Fa, J. Zhou, J. Dong, and X. C. Zeng, “Ferroelectric ordering in ice nanotubes confined in carbon nanotubes,” *Nano Letters*, vol. 8, no. 9, pp. 2607–2612, 2008. 52
- [156] U. Venkateswaran, “Squeezing carbon nanotubes,” *PHYSICA STATUS SOLIDI B-BASIC SOLID STATE PHYSICS*, vol. 241, pp. 3345–3351, NOV 2004. 11th International Conference on High-Pressure Semiconductor Physics (HPSP-11), Berkeley, CA, AUG 02-05, 2004. 54

---

## NOMENCLATURE AND ABBREVIATIONS

|               |  |
|---------------|--|
| CNT           | Carbon Nanotube                              |
| SWNT          | Single Wall Carbon Nanotube                  |
| DWNT          | Double Wall Carbon Nanotube                  |
| MWNT          | Multi Wall Carbon Nanotube                   |
| $(n, m)$      | Chiral indexes n and m                       |
| $\theta_{Ch}$ | Chiral angle                                 |
| $d_t$         | Nanotube diameter                            |
| $\omega_M$    | frequency of the mode M                      |
| $\alpha_M$    | Pressure derivative of the mode M            |
| $\Omega_M$    | Normalized pressure derivative of the mode M |

---

## ACKNOWLEDGMENTS

The research work presented by this manuscript was developed at Institut Lumière Matière, Université Claude Bernard Lyon 1, in collaboration with the Experimental Condensed Matter physics laboratory at University of Antwerp, and with support of the Centre National de la Recherche Scientifique (CNRS) and Agence Nationale de la Recherche (ANR).

I would like to thank:

Alfonso San Miguel, for directing my thesis work.

Denis Machon, for co-directing my thesis work.

Sophie Cambré and Wim Wenseleers, for their collaboration to this research work.

Franck Legrand, Sylvie Le Floch and Régis Debord, for the engineering support.

Felix Balima, Victoria Pishedda and Jean-Christophe Blancon, for the discussions.

Tiago Cerqueira, Miguel Marques and Silvana Botti, for the discussions on theory.

Rémy Fulcrand, for the support on development of devices.

Agnes Piednoir, for the support on Atomic Force Microscopy.

Valerie Martinez and Jacques Le Brusq, for their support at the CECOMO facility.

Thomas Agatocleous and Liu Hongjun, for their work as trainees under my supervision.

Ruben Mascart, Fabio Rampoldi and Carlos Garrido, for the support on informatics.

Christele Macheboeuf, Delphine Kervella, for the administrative stuff.

Christophe Laurent, Alexander Soldatov, Antonio Gomes, Rafael Alencar,

Nedjma Bendiab, Laetitia Marty and Dipankar Kalita, for their collaboration.

Patrice Mélinon, Stéphane Paillès, Valentina Giordano, Georges Bouzerar,

Lucas Piot, Dimitri Hapiuk, Rafael Lobato, Guillaume Souteau, Sabine Korbel,

José Flores, Simón Oyarzun, Rafael Sarmiento, Clément Albin,

Julien Lombard, Emeric Bergmann and Guillaume L'heureux, for the friendship.